To the Graduate Council:

I am submitting herewith a dissertation written by Subhadarshi Nayak entitled "Laser Induced Surface Modification of Aluminum Alloys". I have examined the final paper copy of this dissertation for form and content and recommend that it be accepted in partial fulfillment of the requirements for the degree of Doctor of Philosophy, with a major in Materials Science and Engineering.

Narendra B. Dahotre, Major Professor

We have read this dissertation
and recommend its acceptance:

Accepted for the Council:

Vice Chancellor
and Dean of Graduate Studies

Thesis
20046
.N39

Laser Induced Surface Modification of Aluminum Alloys

A Dissertation
Presented for the
Doctor of Philosophy
Degree
The University of Tennessee, Knoxville

Subhadarshi Nayak
May 2004

To my *alma mater* Indian Institute of Technology, Kharagpur.



Acknowledgments

If I have seen further than others, it is by standing upon the shoulders of giants. -*Newton.*

I am not sure if I have seen any further than others, but I know that without help, support, and encouragement from several persons, I would never have been able to finish this work. First of all, I would like to thank my adviser Dr. Narendra B. Dahotre, for helping me during the whole work with this dissertation. Thank you for providing me direction when I needed most

I am very grateful to Drs David C. Joy, Carl McHargue and Easo P. George for serving in my committee, and providing valuable inputs. I also give a special thanks to Dr. Ian M. Anderson, Dr. Harry M. Meyer, III, Ms. Laura Reister, Dr. Edward A. Kenik and Dr. Hsin Wang for fruitful collaboration and as co-authors and Dr. George M. Pharr for helping me understand nanoindentation. I acknowledge Ford Motor Company for partial funding of the research project. I appreciate Dr. Oludele Popoola of Ford Research Laboratory (presently with Zimmer Inc.) for his support and encouragement. Also GRA support from UTSI in the last semester is greatly appreciated.

Thanks to Dr. Indranil Manna, Dr. B.S. Murty and Dr. K.K. Ray for instilling curiosity in me during undergraduate studies that led me to explore the fascinating world of materials little further. Thanks also to all my colleagues, especially Abhijeet, Anil, Anshul, Greg, Raghuvir, my friends and wing-mates from IIT-Kharagpur, roommate Kiran for all their support and help.

At last, to my wife Jyoti, thanks for supporting me with your love and understanding, and also in mathematical concepts, programming and in LaTeX. I could not have finished this work without your support and help.

Abstract

Purpose of this work is to improve surface related properties of aluminum alloys by employing a laser based technique. Two approaches were taken to achieve this goal. First approach involves a rapid solidification induced by laser without any deliberate change in chemical composition. In second approach, laser was used to deposit Fe_3O_4 on A319, producing an Fe_3O_4/Al reaction composite coating.

In-situ high-speed infrared thermographs captured during laser surface melting of A319 enabled estimation of maximum temperature, temperature gradient and cooling rate. In light of limited spatial and time resolutions of the infrared camera, one-dimensional heat transfer model was adopted for estimating the cooling rate The cooling rate thus estimated provided a range of cell size that closely matched with the experimentally observed cell size The high cooling rate (> 10^5 °C/s) resulted in extensive refinement of microstructure in the laser melted layer. Instrumented indentation technique was used to measure hardness (H) and elastic modulus (E) of the laser-melted layer. Berkovich tip was used to indent the material for 100-nm, 200-nm, 500-nm, and 1000-nm depths. The H and the E were found to be 1.22 GPa and 78.2 GPa, respectively, for 1000-nm indentation depths. The variances associated with H and E were minimal, whereas, the same for substrate possessed significant scattering. Also, H and E increased with decreasing depth of indentation. Closer examination suggested that when the heterogeneity in the material was in the scale of indentation depth, significant scattering took place and the hard phase Si influenced the average hardness. However, the effect of indentation depth on elastic modulus was not statistically significant. The improvement in mechanical properties manifested in better wear resistance.

Aluminum and Fe_3O_4 reacts readily in what is known as Thermite reaction. Infrared thermography was employed for diagnosing the thermal conditions during laser processing. Scanning Auger microscopy, transmission electron microscopy and x-ray diffraction techniques indicated a reaction between oxide particles and aluminum - forming FeAl intermetallic compounds, Al_2O_3, and various intermediate reaction products. Analysis of the coating region, fractured *in vacuuo*, indicated substantial toughness of the material due to extremely refined microstructure with finely distributed oxide and intermetallic particles and strong interfacial bonding between particles and the matrix. Mechanical properties of the coating were evaluated by nanoindentation techniques employing both Berkovich and cube-corner indenters. Hardness and elastic modulus values were found to be uniform at 1.24 and 76 GPa, respectively. No radial cracking was observed for either the Berkovich or cube-corner indenters. These results indicate that the laser-induced rapidly solidified composite material is tough and fracture resistant.

Contents

1 Introduction 1

2 Background and Hypothesis 3

2.1 Surface and Surface Engineering 3

2.2 Aluminum Alloys 5

2.2.1 Cast Aluminum Alloys 6

2.2.2 Modification of Microstructure 20

2.2.3 Surface Engineering of Aluminum Alloys 23

2.3 Laser as a Engineering Tool 30

2.3.1 Laser as a Surface Engineering Tool 32

2.3.2 Surface Properties 36

3 Experimental Concepts 40

3.1 Materials and Processing 40

3.2 Process Diagnosis 42

3.3 Microscopy and Microanalysis 49

3.3.1 Energy Dispersive X-Ray (EDS) Microanalysis 51

3.3.2 Scanning Auger Microanalysis 52

3.3.3 Transmission Electron Microscopy 53

3.4 Mechanical Properties 54

3.4.1 Instrumented Indentation Technique 55

3.4.2 Abrasion and Wear 60

3.5 ThermoCalc 61

4 Results and Analysis 63

4.1 Laser Melting and Rapid Solidification 63

4.1.1 Thermal Conditions During Processing 63

4.1.2 Evolution of Microstructure in Laser Melting 72

4.1.3 Improvement in Properties 79

4.2 Reaction Coating 92

4.2.1 Observation of Exothermic Reaction 92

4.2.2 Evolution of Microstructure in Reaction Coating 105

4.2.3 Mechanical Properties 125

5 Conclusion 140

Bibliography 142

Appendix 151

Vita 156

List of Tables

2.1 Properties of aluminum. 6

2.2 Alloying elements in aluminum casting. 11

2.3 Chemical composition of A319. 18

2.4 Mechanical properties of A319. 19

4.1 Maximum temperatures during laser melting. 67

4.2 Surface cooling rate under non-steady state. 70

4.3 Surface cooling rate under steady state. 71

4.4 Properties derived from IIT for 1000 nm indentation depth. 81

4.5 Properties derived from IIT w.r.t. indentation depth. 84

4.6 Scratch hardness (GPa). 89

4.7 Maximum temperature during laser treatment. 95

4.8 Maximum temperature gradients at the periphery of laser melt-pool in the directions parallel and perpendicular to laser traverse. 101

4.9 Temperature corresponding to maximum gradients, T_{mg}. 101

4.10 Non-steady state cooling rates. 101

4.11 Steady state cooling rate in the directions opposite to laser traverse. 102

4.12 Reactions between Fe and Al [x Fe + (1-x) Al ➔ $Fe_xAl_{(1-x)}$]. 109

4.13 Summary of Auger spectroscopy data. 118

4.14 Nanoindentation (Berkovich) data for Fe_3O_4 coating. 126

4.15 Analysis of unloading data in IIT. 131

4.16 Scratch hardness (GPa). 138

List of Figures

2.1 Al-Si phase diagram. 9

2.2 Schematic representing dendritic growth during solidification. 14

2.3 Flow diagram of the current work. 39

3.1 Schematic of the infrared thermography during laser processing. 43

3.2 Pixels of an infrared thermograph during laser processing. 45

3.3 Calibration of temperature vs. infrared intensity. 48

3.4 Indentation impressions on cross-section of the laser modified samples. 58

4.1 Temperature profile along the laser traverse path. 65

4.2 Optical micrographs of as-received A319. 72

4.3 SEM of the interface between laser melted layer and the substrate. 74

4.4 SEM of the laser melted zone at different magnifications. 75

4.5 Combination elemental map of the laser melted zone. 78

4.6 Schematic of regions designed for indentation analysis. 82

4.7 IIT data: hardness vs. depth of indentation. 83

4.8 IIT data: elastic modulus vs. depth of indentation. 83

4.9 Reduced elastic modulus vs. depth of indentation. 86

4.10 Weight loss under dry sliding test of laser remelted sample. 90

4.11 Frame captured in IRT during laser processing. 93

4.12 Temperature profile in the laser traverse direction across the melt-pool. 96

4.13 Temperature profile perpendicular to the laser traverse direction across the melt-pool. 98

4.14 Optical micrographs of the substrate and laser processed samples. 104

4.15 Infrared thermographs of the samples under laser processing. 105

4.16 Optical micrograph of the Fe_3O_4 coating and the substrate. 106

4.17 SEM of the Fe_3O_4 coating. 108

4.18 Auger micrographs of the reaction coating. 110

4.19 Fracture surface of the coating and substrate. 115

4.20 Fracture of an oxide particle embedded in the matrix. 117

4.21 Schematic of possible phases, and their shape and configuration. 118

4.22 TEM indicating oxide particles within Al cell. 120

4.23 TEM indicating interfacial reaction between Fe_3O_4 particles and Al matrix. 122

4.24 SEM of ultrafine particles formed in laser coating. 124

4.25 SEM of fragmented Fe_3O_4 particles. 124

4.26 SEM of an indentation impression (Berkovich tip). 126

4.27 Properties of the Fe_3O_4 coating as a function of indentation depth. 127

4.28 Cube-corner indenter impressions. 136

4.29 Load-displacement curves for cube corner indentation. 136

4.30 Weight loss under dry sliding test, 10N load. 139

Chapter 1

Introduction

Surfaces may be the most important parts of a component. It is that part of the component most vulnerable to deterioration and failure. Perhaps an easy but uneconomical way of dealing with the problem would be the use of superior materials for the entire component. However, it is often not practical. The properties required of a surface are often contradictory to the bulk design property. For example, a mating component under cyclic load would require a tough bulk with only moderate hardness and the surface with high hardness. It is engineering prudence to combine appropriate surface properties with that of the bulk. Therefore, it is often desired to tailor the surface related properties of critical components without adversely affecting bulk properties. Several techniques have been applied to modify the surface layer without significantly affecting the bulk in order to enhance engineering performance of a component. The appropriate techniques and process parameters to modify surfaces depends upon the particular application. Various surface engineering techniques available today can be divided primarily into two categories: (1) via alteration of microstructure and defect concentration and (2) via change in chemical composition. The first category includes induction hardening, shock treatment, shot peening, ion implantation etc., whereas the second category includes but not limited to chemical vapor deposition (CVD), physical vapor deposition (PVD), plasma coating, carburizing, nitriding, carbonitriding, etc. In this work, the use of a laser

is explored as a surface engineering tool for both the categories in an important class of materials, namely, aluminum alloys.

Aluminum alloys offer many technological and economic advantages over ferrous alloys and other materials. Light weight, very good thermal and electrical conductivity, atmospheric corrosion resistance, high specific strength, high ductility, malleability, castability, manufacturability, and aesthetic appearance with no or little maintenance requirement are a few to name. However, poor surface-related properties of aluminum have severely limited its further or direct use. Hence, in this work, a laser-based technique is explored to enhance the surface-related properties of aluminum and its alloys.

This dissertation is organized into 5 chapters. Chapter 1 introduces the general topic of surface engineering and overviews the dissertation. Chapter 2 develops a background and hypothesis for the research effort. The experimental concepts used to verify the hypothesis are described in Chapter 3. Extra emphasis was given on the experimental procedures, which are not very well developed or established. Chapter 4 describes the results and analysis of various experiments. Conclusion and technical challenges are compiled in Chapter 5.

Chapter 2

Background and Hypothesis

2.1 Surfaces and Surface Engineering

The surface of a component is subjected to the influence of the environment, contact stress and other physical and chemical stimuli. Structural components fail by wear, corrosion, erosion, fatigue, contact stress concentration, etc. Even electrical and electronic components fail more often not by electronic property deterioration but by structural or mechanical failures. Often, it is the combined effect of external stimuli that is much more damaging and very complex to address

through component design. Most of these failures are affected and initiated by the surface conditions. The selection of a material on the basis of both surface and bulk properties severely limits engineering and economic considerations. Often, obviously contradictory sets of properties are required for the bulk and surface of a component. For example, heavy-duty components, such as an idler wheel of an excavator require high hardness at surface and at the same time high toughness in the bulk. Overall hardness can not be raised as it will induce brittleness. On the other hand, moderate hardness to maximize toughness would cause undue surface wear, deformation and damage. The desired engineering design is to maximize surface hardness without compromising bulk toughness in an economic method.

Fortunately, there are several available techniques by which one can modify the `surface-only' properties without affecting the bulk properties. These techniques have been developed to efficiently and economically combine a relatively cheap substrate material with the appropriate surface layer. Techniques of modifying the surface is based on either of the two principles, viz.- (1) alteration of the surface microstructure, stress distribution and defects concentration and (2) change of chemical composition. The type (1) consists of thermal, mechanical or thermo-mechanical treatment of surface. As a result of such treatment, the microstructure of surface and near-surface volume undergoes dramatic alteration without significant or deliberate changes in chemical composition. The primary mechanism of this technique is based on solid state; diffusion-less or stress-induced phase transformation, surface melting, increasing defect density, and inducing residual compressive stresses. This category includes shot peening, surface-localized heat treatment, remelting, flame hardening, induction hardening, shock wave treatment, ion implantation etc. Only microstructural changes may not be possible or may be inadequate to achieve desired set of properties. In that case, the surface composition needs to be selectively altered so as to make it amenable to microstructural modification thus and/or achieve desired set of surface related properties. The type (2) includes: carburizing, nitriding, carbonitriding, physical vapor deposition (PVD), chemical vapor deposition (CVD), plasma spraying, laser surface alloying etc [2].

The technique of surface modification depends upon the substrate materials, and the particular application requirements, particularly the design stress level and flaw tolerance. At moderate loads, protection can be provided by means of CVD and PVD processes, wherein the layer thickness amounts to several microns [3]. However, at high

contact loads, a thicker and well-bonded hardened layer is required, which can be provided by means of plasma spraying and laser processing. These techniques are capable of modifying the surface layer over several hundreds microns [2, 4]. Often, a composite coating is more desirable since it can combine apparently contradicting properties of the substrate and the selectively added coating materials (often refractory ceramics, intermetallic compounds or constituents to form these in situ).

These tools of improving surface characteristics have greatly increased opportunity to utilize advantages of many materials, deemed unworthy otherwise. Yet, in many other cases, it has improved design parameter, manufacturability, component performance, life and reliability and economy. One class of metallic materials, namely aluminum alloys are seen as potential materials for many applications, when appropriate surface engineering has been applied.

2.2 Aluminum Alloys

Aluminum and its alloys have gained much attention in recent years for its most striking characteristic, i.e., `light weight'. The specific strengths of many aluminum alloys are even better than that of high strength steels. The socio-politico-economic factors have driven us to achieve better energy efficiency in our day-to-day operations. Often, the focus is to reduce the payload to achieve this goal, particularly in transportation industry [5]. Aluminum-based alloys (density = 2.68g/cm^3) have replaced other high-density materials including ferrous alloys (density = 7.8 g/cm^3). The transportation industry remains the single largest domestic (USA) consumer of aluminum at 29% [5].

Table 2.1: Properties of aluminum. From Ref. [6]

Property	Value	Unit
Crystal Structure	FCC	..
Density	2.68	g/cm^3
Thermal Conductivity	247	W/m.K
Specific Heat Capacity	900	J/kg.K
Coefficient of Thermal Expansion	23.6	$^oC^{-1}x10^{-6}$ m/m
Hardness	0.6	GPA (annealed)
Melting Point	660	^oC
Electrical Resistivity	2.655×10^{-8}	Ω-m

Aluminum also possesses several other important characteristics making it advantageous over other materials (Table 2.1). The high electrical and thermal conductivity, ductility, malleability, formability, machinability, castability and corrosion resistance of aluminum has made it a material of popular choice [7]. Due to its face centered cubic (fcc) crystal structure aluminum possesses very good ductility, malleability and mechanical formability. Most aluminum alloys are easy to machine or machinability can be further improved, if so desired, by making slight adjustment in chemistry. Hence, aluminum alloys are very popular in wrought form. Excellent casting properties, easy availability of scrap and low melting point makes it an attractive choice also for casting as a substitute to cast iron components as well ($\rho = 7.8 g/cm^3$).

2.2.1 Cast Aluminum Alloys

The melting point of Al is 660°C. Moreover, Al forms eutectic system with many common alloying elements, further lowering its melting point. Hence, it is easy and

efficient to melt aluminum for casting purposes. Combined with this, Al possesses good castability particularly for intricate and thin section casting. It is relatively easy to control gas contamination of aluminum casting. The only major gas contaminant is hydrogen, which can be easily controlled by regular chlorine or freon fluxing before casting or by vacuum treatment of the liquid metal [6]. Moreover, it produces a very good as-cast surface finish with lustrous surfaces and little or no blemishes [6].

The automotive industry is the largest market for aluminum castings and cast products make up more than half of the aluminum used in cars [5]. Cast aluminum transmission housing and pistons have been virtually universal in cars and trucks throughout the world for years. Many other engine parts are cast aluminum and the applications grow as automakers seek new ways to save weight and gain fuel efficiency and performance. Cast aluminum is also widely used in other forms of transportation, including aircraft and marine engines and structures [5, 8].

One such automotive casting, namely, engine block is a critical component that used to be a major component of payload (grey cast iron). This is an intricate casting with widely varying section thickness. The engine block works under mechanical and thermal cyclic stresses during operation. Also, it is in relative motion with other engine parts such as piston. High fatigue strength and excellent wear resistance are of utmost importance for this kind of applications. It has been realized that aluminum casting is suitable to make pressure tight, defect-free and intricate casting. Several aluminum alloys have entirely replaced cast iron reducing weight and increasing fuel efficiency.

The most widely used aluminum casting alloys are a class of Al-Si based composition [6, 8] for the reasons explained below.

Al-Si System

The most significant effect of silicon as an alloying element in aluminum alloys is the improvement in melting/casting characteristics. Addition of silicon to aluminum dramatically improves fluidity, hot tear resistance and feeding characteristics [6,9]. Silicon addition also results in reduction in specific gravity and coefficient of thermal expansion. Al-Si cast alloys are widely used due to their excellent combination of properties such as excellent castability, reduced hot shortness, corrosion resistance, wear resistance and strength to weight ratio.

The most prominently used compositions in all casting processes are those of the aluminum-silicon family. The Al-Si binary phase diagram consists of basically a simple eutectic reaction. Al-Si binary alloy is a eutectic system with the eutectic composition at 12.6 wt.% Si [10] (Figure 2.1).

The solid solubility of Al in Si at room temperature is practically negligible. Similarly, the solid solubility of Si in Al is extremely limited. Depending upon cast method and composition, Si assumes either plate-like, irregular or rod-like (fibrous) morphology. Hence, the principal microstructural features of these alloys are primary -Al dendrites with inter-dendritic eutectic, fibrous or plate-like eutectic or angular primary silicon crystals in an eutectic matrix [6,11].

Various alloying elements are in use to improve processing and properties of Al-Si castings. The solubility of most common alloying elements (Cu, Mg, Mn, Fe, and Zn) in aluminum increases substantially with increasing temperature. This significant reduction from high equilibrium solid solution at high temperature to very low (almost negligible) solubility limit at room temperature results in precipitation of secondary

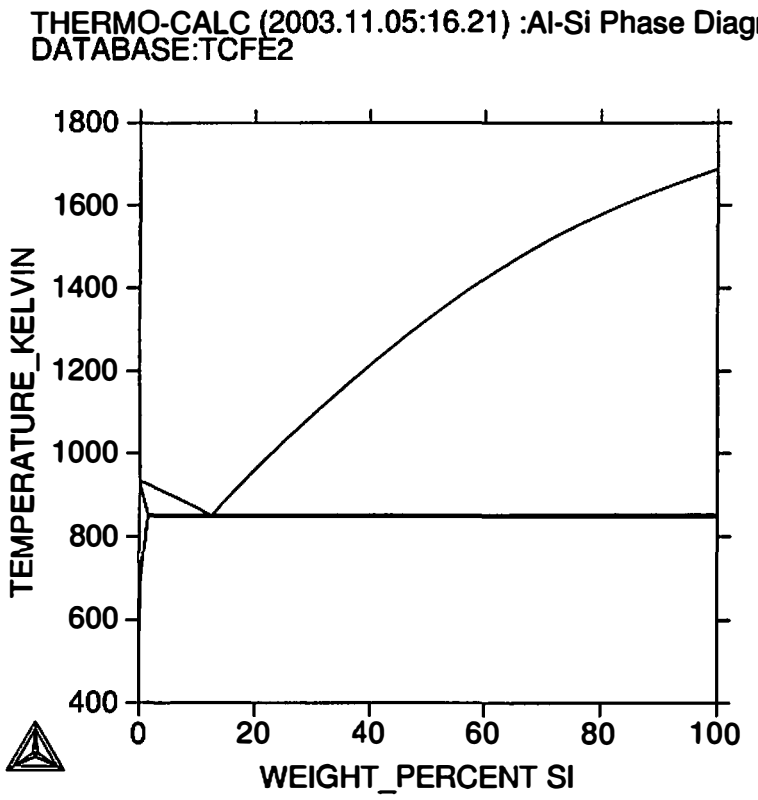


Figure 2.1: Al-Si phase diagram

phases, and primarily intermetallic compounds. The wide variety of intermetallic phases in aluminum alloys occurs because aluminum is highly electronegative and trivalent [12]. Different alloying elements are used for different purposes. Usually they are used in combination to optimize cost, manufacturability and application. The alloying elements and their most significant contributions are listed in the Table 2.2. Several Al-Si based alloys and metal-matrix composites, such as A318, A319, A356, A357, A360 and A390, are in use [9].

Microstructure of Al-Si system

When a hypoeutectic composition (< 12:6 wt% Si) solidifies, the primary aluminum forms and grows in dendrites. In contrast, as a hypereutectic composition liquid solidifies, primary Si phase precipitates first. When the eutectic point is reached, the eutectic Al-Si phases nucleate and grow until the end of solidification. At room temperature, hypoeutectic alloys consists of a soft and ductile primary aluminum phase and eutectic Al + Si phase mixture. Hypereutectic alloys usually contain coarse, angular primary silicon particles [8, 9, 13]. Any other alloying elements or impurity elements present, precipitate as third phase more often than not as intermetallic compounds (aluminides).

The most important features that describes the microstructure of Al-Si systems are:

- Grain size and shape
- Dendrite and dendrite-arm spacing
- Size and distribution of second phase particles and inclusion.

Table 2.2: Alloying elements in aluminum casting. From Ref. [5, 6, 9].

Element	Range	Purpose
antimony	>0.05%	refine eutectic microstructure
bismuth	few ppm	Improves machinability
boron	0.2-1.0%	grain refinement
cadmium	>0.1%	Improves machinability
calcium	<0.005%	eutectic modifier
chromium	-	deters grain growth
copper	4-10%	Improves strength, hardness
iron	-	hot tear resistance
lead	>0.1%	machinability
magnesium	0.4-0.6%	strength and hardness
magnesium	4-10%	heat treatable
manganese	>0.5%	casting soundness[1]
mercury	-	prevents passivation[2]
nickel		high temperature properties[3]
phosphorous	few ppm	refines primary Si and coarsen eutectic structure
silver	0.5-1.0%	precipitation hardening
sodium	-	modifies Al-Si eutectic structure
strontium	0.008-0.04%	modifies Al-Si eutectic structure
tin	up to 25%	antifriction
titanium	-	grain refinement
zinc	-	heat treatable[4]

[1]Manganese is useful for wrought alloys and primarily an impurity in castings from the scrap.

[2]In sacrificial anode. Now restricted due to environmental consideration.

[3]Usually used along with copper.

[4] Accompanied by Cu and/or Mg.

Grain size and shape

A fine, equiaxed grain structure is desired in most materials. A microstructure with fine and equiaxed grains offers the best combination of strength and ductility. The flow stress (σ_f) of a polycrystal material with average grain size, d, is given by Hall-Petch relation as follows.

$$\sigma_f = \sigma_o + kd^{-1/2} \qquad (2.1)$$

(σ_o is the flow stress of single crystal and k is a material constant). The type and size of grain formed are determined by alloy composition, solidification rate, and the addition of grain refiner (master alloys). The most popular grain refiner are usually a Ti and/or B in aluminum, which provide heterogeneous nucleation sites. Low pouring temperature and higher solidification rates in combination with grain refiners is resorted to obtain optimum combination of properties in cast components. Now-a-days, grain refiners are very commonly used for Al castings. In fact, fine grain size is taken for granted and is no more reported in quality assessment and other microstructural parameters overshadow the quality index.

Dendrite and dendrite-arm spacing

Solidification of almost all Al-Si commercial cast alloys takes place via the formation of dendrites in the liquid solution. The cells contained within the dendrite structure corresponding to dimensions separating the arms of primary dendrites are controlled for a given composition primarily by solidification rate. Presence of second phase particles and oxide or gas inclusion affects this spacing. The farther apart the dendrite arms are, the

coarser the distribution of the micro-constituents and the more pronounced their adverse effects on properties. Thus, small interdendritic spacing is the key for better quality. Dendrite growth is presented in Figure 2.2.

Second phase particles and inclusion

Aluminum is electronegative (1.6 in Pauling's scale). Moreover, it is trivalent. The fcc crystal structure permits some degree of solubility of metals in aluminum at higher temperature. But, the solubility of most metals substantially falls as the temperature decreases. Hence, a wide variety of intermetallic phases are present in aluminum alloys. These intermetallic phases can be exploited to improve mechanical properties of aluminum alloy via particle strengthening.

Often, Materials engineers seek one single microstructural feature to define general refinement of a casting that unambiguously correlates to the mechanical properties. Solidification in Al-Si systems usually proceeds via formation of dendrites. The microstructural features that most significantly influence mechanical properties of the Al-Si cast alloys are:

- Dendritic arm spacing,
- Size, shape and distribution of Si particles,
- Fracture resistance of Si,
- Interfacial strength between Si and Al.

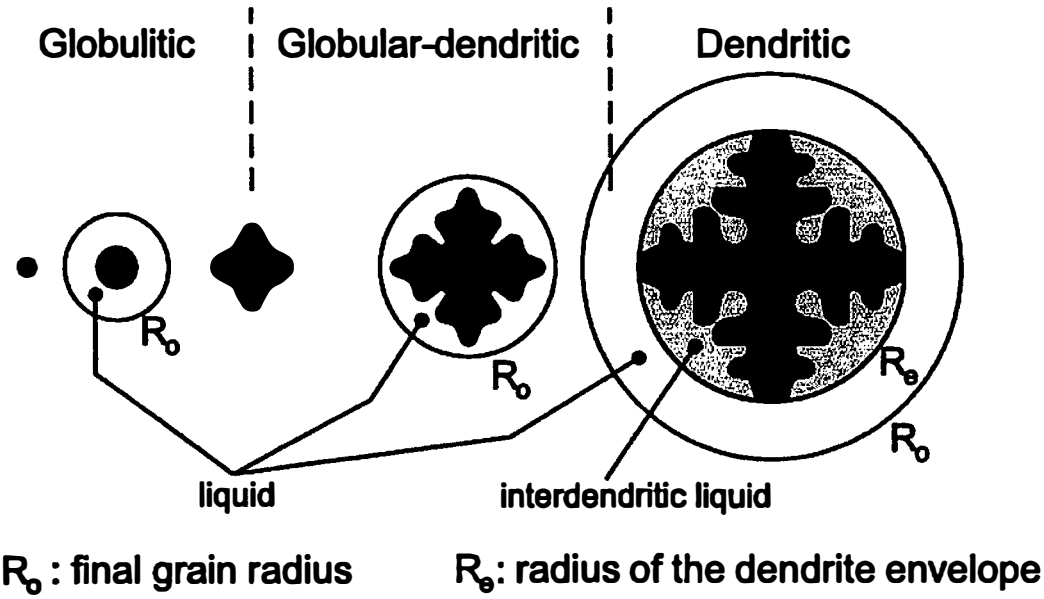


Figure 2.2: Schematic representing dendritic growth during solidification.

The microstructure features such as grain size and dendrite-arm spacing are strong function of solidification rate. Dramatic variations are observed based on the cooling rate during solidification as in sand cast, permanent mold cast or die cast.

Grain Refinement: A casting with fine, equiaxed grain structure offers the best combination of strength and ductility. As predicted by Hall-Petch relation (Equation 2.1), smaller the grain size (diameter) higher is the flow stress of the material. The grain size is primarily a function of alloy composition, solidification rate and addition of grain refiner (master alloy). A higher cooling rate increases the under-cooling during solidification. Similarly, the grain refiner increases the heterogeneous nucleating site. Essentially both of these methods act to ease nucleation, therefore, formation of more number of grains. Grain size has been used as a single most important feature. However, use of grain refiner

has reduced the importance of grain size as a good indicator of microstructure and correlation with respect to properties. Primary dendrites are the first series of branches that form from the nucleus of a grain in the direction of preferential growth. The spacing or interval of these dendrite arms, when viewed in a plane, is equivalent to the grain size of the material. The casting parameters such as grain refinement, cooling rate, alloy constituents, thermal conductivity, thermal and solutal melt flow etc. affecting the grain size also affects dendrite size in the same manner. There are at least three microstructural features that may be used to describe the extent of dendritic refinement in a casting. These are

1. secondary dendrite arm spacing (SDAS)
2. dendritic cell interval (CI) and
3. dendrite cell size (CS)

Secondary Dendrite-Arm Spacing (SDAS): Secondary dendrite arms arise from perturbations during the growth of primary dendrites, and their spacing is a function of cooling rate alone. Since arm spacing is a strong function of cooling rate, this gives a snapshot of the local solidification time as a function of billet radius or casting section thickness. The faster the cooling rate, the smaller is the secondary dendrite arm spacing (SDAS). The SDAS is empirically related to solidification time (t_s) as per Equation 2.2 [14].

$$\mathbf{SDAS = k \times t_s^m} \qquad \textbf{(2.2)}$$

where **k** and **m** are materials constants; function of latent heat of fusion and diffusivity.

If the spacing of primary dendrites - or cell nuclei - is large enough, these secondary arms are detectable and measurable. If primary dendrite spacing is too small, secondary dendrites may not form, or may be too small to measure conveniently. The cells contained within the dendrite structure roughly correspond to the dimensions separating the arms of primary dendrites and are controlled for a given composition primarily by solidification rate. However, secondary dendrite-arm-spacing is difficult to measure in most aluminum commercial castings. Usually grain size is so small that the dendrites have not developed in a good secondary growth pattern. Moreover, secondary arms can coarsen isothermally by different mechanisms such as tip remelting, transport from the necked region at the dendrite root or reduction in radius by redistribution to its nearest neighbor.

Secondary arms can also dissolve or fracture by inter-dendritic melt flow. The newly fractured arms act as newer nucleation sites for solidification - known as grain multiplication. This makes it difficult to compare microstructure of two casting in terms of dendrite arm spacing.

Dendrite Cell Interval is the distance between centerlines of adjacent dendrite cells whereas Dendrite Cell Size is the width of individual cells (arms). The dendrite cell interval is basically combination of a cell size and the width of the inter-dendritic phase present.

For alloys with a small amount of inter-dendritic material (generally neglected) the cell size and interval are equal. However, for alloys with large amounts of inter-dendritic materials, that is, in case of composition closer to eutectic point or a higher solidification rate (i.e., smaller cell size), the width of inter-dendritic phase volume can

not be neglected and measurement of cell interval is preferred. Hence, the cell interval is considered more appropriate for quantitatively describing such a microstructure. Line intercept methods can be used to measure the cell interval or cell size. The relationship between solidification rate and cell size in case of Al-Si alloys may be empirically described by the Equation 2.3 [15]:

$$y = 0.002 \times R^{-0.337} \quad (2.3)$$

where y is the cell size in inches, and **R** is the cooling rate during solidification in (^{o}F/s). The Equation 2.3 can be rewritten in metric units as

$$\text{Cell size in } \mu m = 416.7 \times (\text{Cooling rate in } {}^{o}C/s)^{-0.337} \quad (2.4)$$

The strong dependence of the microstructural features of cooling rate can be exploited to our advantage. By increasing the cooling rate, a finer microstructure thus a set of properties can be engineered in these alloys. The limitation of alloys cast under near-equilibrium condition can be overcome. For example, the high-cycle fatigue failure in Al-Si alloys takes place by nucleation and propagation of micro-cracks around silicon phase or in aluminum matrix. Hard and brittle Si can crack or can detach from soft-Al matrix. During cyclic load, micro-cracks can initiate in such locations and propagate. For large cell size and secondary dendritic arm spacing, the cell boundaries are well defined by a high density of Si particles. The Si particles in the cell boundaries are further apart but majority of them are on cell boundaries. The crack propagates through high density of Si particles. On the contrary, for a finer microstructure, the crack propagates along the grain boundaries. In light of this, it has been demonstrated that refinement of the eutectic silicon particles improves fatigue crack growth resistance [6]. The size and distribution of second phase particles are very complex to control. However, careful empirical control of

chemistry can ensure uniform size and distribution. Use of modifier and refiners are useful in altering the eutectic structure and hypereutectic Si morphology thereby improving mechanical properties of the casting.

Alloy A319

One of the most important and most widely used alloying element in Al+Si system is copper. Copper substantially improves strength and hardness in the as-cast condition. Additionally, it also makes the alloy heat treatable (age-hardenable). Alloys containing 4-6 wt% Cu respond most strongly to thermal treatments. One such Al-Si-Cu based alloy, A319, is popular for automotive applications (Table 2.3). Its typical microstructure consists of primary Al and divorce-eutectic phase mixture of Al + Si and, Al_xCu_y. Presence of Cu makes it amenable to heat treatment. The solubility limit of Cu in Al at eutectic temperature is 5.65 wt% and that at room temperature is $\approx$ 0 wt%. If an alloy is quenched from high temperature, a supersaturated aluminum matrix results. This can be exploited for improving mechanical properties via a heat treatment called precipitation hardening. When a Cu-supersaturated alloy is thermally treated (known as aging), coherent or semi-coherent GB zones or non-coherent Al_xCu_y intermetallic compounds (commonly $AlCu_2$) precipitates, providing precipitation strengthening.

Table 2.3: Chemical composition of A319.

Elements	Si	Cu	Mg	Mn	Fe	Zn	Ti	Ni	Others	Al
Range (%)	5.5-6.5	3.0-4.0	<0.1	<0.5	<1.0	<1.0	<0.25	<0.35	<0.5	balance

Table 2.4: Mechanical properties of A319. From Ref. [1].

Condition	**Sand Mold**		**Permanent Mold**	
Property	As Cast	T6	As Cast	T6
tensile Strength (MPa)	185	250	235	280
Tensile Yield Strength (MPa)	125	165	130	185
Elongation (%)	2.0	2.0	2.5	3.0
Hardness (HB)	70	80	85	95
Shear Strength (MPa)	150	200	165	185
Fatigue Strength (MPa)	70	75	70	..
Compression Yield Strength (MPa)	130	170	130	..

Copper is also known to favorably modify brittle Al-Fe-Si (Fe as a tolerable impurity) phase [6]. Copper improves the corrosion resistance as well [1, 6, 8]. The mechanical properties of the alloy A319 can widely vary with respect to its processing and condition (sand cast or permanent mold, as-cast or heat treated) [1]. Table 2.4 represents common mechanical properties of A319 with respect to the processing and heat treatment conditions.

Cast Al-Si alloys are associated with casting defects such as porosity and inclusion. Besides obvious reduction in load-bearing cross-section, these defects are particularly harmful for stress concentration. Such defects in surface and near-surface region dramatically reduce high cycle fatigue strength. It is desirable to repair such defects particularly on surface. Alloying elements are known to change defect formation characteristics, particularly by altering solidification range. Many alloying elements can be exploited favorably to bring in improvement in microstructure and properties. Al-Si system is particularly amenable to great alteration in microstructure by addition of some elements in very minute quantity [6, 9, 1]. This kind of microstructure alteration specially

named as "Microstructure Modification" for its great effectiveness in improving casting properties.

2.2.2 Modification of Microstructure

Addition of few reactive elements, referred to as inoculants, just before pouring is known to greatly modify the size, shape and distribution of microstructural features of Al-Si alloys. Some elements modify the normally occurring eutectic phase mixture. Yet, some other elements modify specifically the hypereutectic Si phase. The addition of these elements to a hypoeutectic Al-Si alloys results in a finer lamellar or fibrous eutectic network and that to a hypereutectic composition results in finer and less acicular primary Si particles. The most commonly used modifying elements are Sr, Ti, Ca, Na, Sb, P and B depending on the alloy composition and casting process.

Hypoeutectic aluminum-silicon alloys involve the improvement of properties by inducing structural modification of the normally occurring eutectic phase mixture. Ca, Na, Sr and Sb are common elements for this purpose, addition of which, results in a much finer distribution of lamellar or fibrous eutectic network. Basically, the surface characteristics of nucleating Si changes due to addition of such chemical modifier. Consequently, the growth of silicon crystal within the eutectic occurs as a finer distribution of lamellae relative to the growth of the eutectic [6]. Typically, modified structure displays higher tensile strength, but more significantly, exhibits improved ductility. Modification is also known to improve casting characteristics by improved flow and feeding as well as by superior resistance to cracking at elevated temperature.

The primary silicon in hypereutectic Al-Si alloys precipitates in discrete, angular, large and coarse morphology that is harmful in the casting and in machining of these alloys. Addition of P has a remarkable effect on the size, shape and distribution of these particles [6, 9]. Phosphorous (in the form of metallic P, P-Cu and/or PCl_5), when added to molten hypereutectic alloys, greatly modify size, shape and distribution of primary silicon particles. Sr, K, Ca, Na etc. modify size, shape and distribution of eutectic Si. However, P nullifies the effect of Sr or Na. Hence, it is difficult to modify eutectic structure and the primary Si at the same time. This limits the gain due to modification in hypereutectic systems.

Microstructure Modification by Rapid Solidification

Rapid solidification causes extensive microstructural refinement in Al-Si alloys [16]. Besides, refining the microstructural features such as α-Al dendrite, it also modifies the morphology of Si substantially. (rapid solidification refines both dendrites and eutectic phases). When the growth rate increases the eutectic Si changes in morphology from plates to fiber [17]. Also, a fully eutectic structure can be achieved over a range of compositions, which does not necessarily correspond to eutectic composition [18].

By controlling solidification parameters such as cast temperature, cooling rate, modifier addition, etc., one can attain a tailored microstructure of these alloys. Consequently, widely different sets of properties can be attained depending on structure of reinforcing Si-rich particles much like in particulate composite materials. However, different parts of a complex casting undergo solidification at different rate, making it

difficult to control as the microstructure refinement also vary based on section thickness. This results in a very undesirable non-uniform property manifested by non-uniform microstructure of the casting. For varied cross-section and intricate shape, it is not possible to resort to rapid solidification to modify entire bulk microstructure. Special casting techniques (e.g., squeeze casting, semi-solid casting, thixocasting and Cosworth casting) are employed to address these issues in critical and expensive castings [14, 7, 19]. The properties can be improved by one of the several techniques in bulk of a component. However, it may not be practical or economic. Yet, in many other cases a more significant improvement is desired selectively on surface.

Surface Related Properties of Al Casting

Al alloys in general and A319 in particular have poor surface-related properties. This has severely limited their direct uses in many applications despite of their several economic and engineering advantages. As discussed in Section 2.2.2, it is often not possible to obtain a modified microstructure in the bulk as well as on the surface of the entire component. Most of the wear resistance can be attributed to the presence of hard silicon particles distributed in the matrix of an Al-Si alloy. The amount of these particles becomes significant above equilibrium eutectic composition (>12.6 wt%).

The most significant mechanism for wear of Al-Si alloy is the delamination of surface material. The breaking of Si particles or Si-matrix interface can initiate microcracks. These microcracks can form network, and propagate along sub-surface region until they reach the surface, then the whole piece detaches. Since the Si particles

can not provide reinforcement in the center of a cell, the soft aluminum matrix can undergo local plastic deformation and can eventually crack.

Size, morphology and distribution of Si particles are the most important factors in wear of Al-Si alloys. Generally, Si increases the average hardness of the alloy, which roughly translates into higher wear resistance. Distribution and size of primary silicon particles, rather than the overall silicon content of the alloy has been identified as the key parameter. Finer particle sizes were usually found to improve wear resistance [20, 21, 22]

2.2.3 Surface Engineering of Aluminum Alloys

Aluminum alloys have gained increasing popularity because of their excellent bulk characteristics. However, the surface properties of aluminum alloys, in particular the hardness and wear resistance, are inadequate to fulfill all demands of many other applications. There exists many techniques to improve surface related properties including corrosion resistance, wear and scuffing resistance, fatigue resistance etc. They include but are not limited to electroplating, immersion plating, electroless plating, painting, porcelain enamelling, shot peening etc. [23], chemical vapor deposition (CVD), physical vapor deposition (PVD), plasma spraying and laser surface engineering (LSE) etc. [3, 24]. The appropriate technique depends on the required layer thickness and perhaps more importantly on particular application. At high contact loads, a thicker hardened layer is required, which can be provided by plasma spraying or laser surface engineering via coating a thick ceramic-based layer. Hardfacing or ceramic coating of aluminum alloys to improve their surface properties has been a challenge for a long time

in materials engineering [25]. Only a few aluminum alloys are amenable to type (1) surface modification (page 4), and only to a limited extent. Thermal spray coatings are not very adherent on aluminum owing to a tenacious layer of oxide that is inherent to aluminum. The low melting point of aluminum makes it harder for this and many other kind of surface treatments. Ceramic coatings are not very encouraging for aluminum [26]. Thus, both to continue using aluminum alloy (for its lighter weight) and to improve wear resistance, a number of techniques have been explored. These techniques include usage of metal matrix composite [27, 28, 29], plasma spraying [30, 31], thermal spraying [30, 31], hard anodizing [30, 31, 32], based on formation of alloy, composite and monolithic coating on the surface. All the above-mentioned techniques of surface modification have some intrinsic limitations. The high thermal stresses and the severe wear regimes in applications can lead to delamination of the coatings with catastrophic failure [32]. Furthermore, it is difficult to get a coating of consistent quality in the case of thermal spraying, and on the other hand, plasma coating requires extensive surface preparation.

Hardfacing of aluminum alloys to improve their hardness and wear resistance has been a challenge for a long time to the field of materials science and also the industry. In particular, surface coating with hard metals and ceramic layer can be a very promising approach. For instance, the hardness and wear resistance can be improved significantly by anodizing. However, there are still major drawbacks in these conventional methods. In conventional methods coating for wear/corrosion protection remain separated from the substrate by a sharp interface, which may greatly affect the mechanical performance.

Rapid Solidification for Surface Engineering

Even though microstructure modification improves properties of the entire component, it is often not practical. Modification of primary and eutectic silicon is difficult to attain in the same casting by chemical modification due to fact that P and Na (or Ca, Sr) nullify each other's effect. Also chemical modification does not refine aluminum dendrites. On the contrary, rapid solidification does refine primary silicon, eutectic structure as well as aluminum dendrites. However, it is not possible to improve the mechanical properties of any real life engineering components via rapid solidification in its entirety, and to a great extent.

A thermal or thermo-mechanical treatment can be carried out selectively on the surface to engineer surface related properties of a component, as in induction hardening of steel, wherein, the surface layer is heated and allowed to cool rapidly (or quench). The solid-state martensitic transformation of austenite improves hardness of the surface layer by the solid-state diffusion-less transformation. Unfortunately, solid-state phase transformation of aluminum alloys is not known to improve properties dramatically and often is extremely difficult to control with adequate precision. However, the microstructure of the near surface volume in Al-Si system can selectively be refined by melting and re-solidifying; thus tailoring the surface-related mechanical properties. A high energy density laser when scanned over a surface (if coupled), it can melt only a confined volume of laser-material interaction. At the same time, the rest of the component is at lower temperature and thus acts as an infinite heat sink (chill). The high thermal gradient and very good thermal conductivity of aluminum, induces rapid solidification of the molten metal once the laser has moved away from that spot. The

surface layer thus rapidly solidified would consist of a refined microstructure and improved surface related properties. Laser-processing parameters can be controlled to optimize the melting and re-solidification; consequently, properties of a surface layer thus produced. A high-power traversing laser can cause metal to melt and re-solidify in tracks and thus covers the entire selected surface area with the re-solidified layer. The solidified layer possesses uniform and enhanced mechanical properties manifested by such a modified microstructure. Such a technique would significantly improve mechanical properties of surface. Improvement in mechanical properties via microstructure refinements roughly translates into better surface-related, in particular, friction and tribological properties of the materials.

For many extreme applications/conditions, further strengthening is required. Incorporation of hard ceramics is the obvious choice for this purpose [4]. However, it is difficult to incorporate ceramic in aluminum [25]. Liquid aluminum has very poor wettability with most ceramics [25, 33]. However, high reaction-tendency of aluminum can be exploited to improve wettability (reaction induced wetting), produce metastable, and novel composite and synthesize a coating via reaction. Many such reactions are highly exothermic in nature and are classified as combustion synthesis.

Combustion Synthesis of Coating

In 1885, V.M. Goldschmidt suggested that aluminum metal powder would reduce most metal oxides at high temperatures because aluminum oxide formation involves higher heat evolution than most other metal oxides. In other words, aluminum has a higher affinity for oxygen (and most oxidizing species [34, 35]) than most metals. Furthermore,

the Ellingham diagram, which depicts thermodynamic data for chemical reaction among reacting metals and non-metallic oxidizing elements, predicts that the iron oxides (FeO, Fe_2O_3, Fe_3O_4) are readily reduced by aluminum to form (Al_2O_3) [36, 37].

Thermite welding is perhaps the earliest application of such chemical principle. Low melting point of aluminum is convenient to obtain liquid aluminum for this welding operation. In this process, liquid aluminum and Fe_3O_4 (sometime other oxides are in use) are allowed to react, forming super-heated liquid iron. The liquid iron thus produced is used as the filler metal for the welding operation of very heavy sections such as rail tracks. The reaction that occurs in thermite welding can be written as Equation 2.5.

$$3Fe_3O_4 + 8Al = 4Al_2O_3 + 9Fe \quad (\Delta G = -3095\ kJ/mol\ of\ Al\ at\ 1173K) \quad (2.5)$$

In thermite reaction, when the mixture of reactants (one or several metals and metallic alloys and a metal compound, such as oxide, carbide, boride, etc.,) is ignited at one place, the reaction continues on its own accord. When the heat generated is sufficient for the reaction to continue, it is known as combustion synthesis or Self-propagating High-temperature Synthesis (SHS). The reaction between aluminum and iron oxides in thermite welding is not just self-propagating, often it is so violent that it needs to be cooled by adding ferroalloys [38].

If the liquid iron, produced due to reaction between liquid aluminum (excess) and iron oxides, is allowed to mix further, they can react to form various iron aluminides. The formation of aluminides is yet another class of exothermic reaction, itself considered for combustion synthesis. The further reaction to form iron aluminides would cause to liberate more heat, and such extreme exothermic reactions would develop into a very high thermal gradient.

There are several advantages of combustion synthesis over conventional synthesis methods, namely:

- The simple exothermic nature of the SHS reaction avoids the need for expensive processing facilities and equipment and reduces energy requirements.
- The generation of a high reaction temperature can volatilize low-boiling point impurities, and, thereby produce higher-purity products.
- High thermal gradients and rapid cooling rates can give rise to non-equilibrium or metastable phases resulting in novel properties.

Materials like borides, carbides, nitrides, silicides, intermetallics, and binary compounds have been synthesized via combustion synthesis [37]. These exothermic reactions can be initiated at one place by such means as resistance heating, induction heating and flame. High power-density lasers have also been successfully used to initiate SHS. Recently, SHS has attracted attention for its suitability and ease to synthesize composite materials. Ceramic-ceramic, metallic-metallic and metallic-ceramic composites have been successfully synthesized by such method.

All these characteristics of combustion synthesis or SHS are very desirable for synthesis of coatings. Combustion synthesis can be selectively achieved on surface for surface modification particularly in synthesis of composite coating. As described previously (page 4), a composite coating is often desirable as it can combine properties of the substrate and that of a coating material (such as a ceramic or intermetallic compound). A composite is often advantageous over its constituents, as it can possess a superior set of properties; even a combination of seemingly conflicting properties. A ceramic reinforced metal matrix composite is superior to both ceramic and metal, as it

can possess higher ductility than ceramic and higher hardness and strength than metal; and possibly higher toughness than both. Such a material is most desirable in many critical applications. However, one of the primary limiting factors in developing such a material is the relative poor wettability of ceramic for metal and, therefore, a weak bonding between the matrix and the reinforcement [14]. Since, the load transfer from matrix to reinforcement is abrupt, the interface is a potential site for crack initiation and propagation.

Several efforts are being made to enhance wettability and bonding between the ceramic and metal. One such method is to choose the material system in which the ceramic and metallic constituents have potential for chemical reaction, which promotes reaction-induced wetting of the particle by the matrix. Often reaction between metal and ceramic can alter the wettability characteristics because of the resulting reaction product layers [33]. The free energy associated with such a reaction, provides energy required for work of spreading on particle. Aluminum has high affinity for oxygen. As depicted in an Ellingham diagram [36], aluminum is capable of reducing a large number of oxides [36]. Oxides of iron are proven candidates in self-sustaining aluminothermic reaction as in thermite welding [38]. Another problem in synthesis of such composite materials is that the reinforcing particles tend to segregate owing to hydrophobic nature, lack of wettability, higher surface tension and (often) wide density differences [25]. A non-uniform microstructure with segregated particles manifests in adverse mechanical properties [39]. Often, such undesired segregation is minimized by mechanical or electromagnetic stirring. Similar difficulties arise in laser coating of aluminum alloys with composite (ceramic + Al) because of the poor wetting between liquid aluminum and

solid ceramic [26]. It was realized that the laser can be used as a great tool to produce both for rapid solidification as well as to initiate the combustion process to synthesize coating. Laser energy when focused in a small area confined to the interaction volume which is subjected to rapid cooling as heat is rapidly transported to rest of the component via conduction. In case of a ceramic coating, the ceramic particle and molten metal can mix due to convective flow. Moreover, high temperature gradient coupled with violent exothermic (aluminothermic) reactions between Al and certain ceramic phase particles (for example in the present case, Fe_3O_4) would ensure wetting, mixing and homogenization. Also very high negative free energy associated with such aluminothermic reaction increases wettability by reducing surface tension. Hence, laser surface engineering was considered to be suitable for synthesis of such a reaction composite coating.

2.3 Laser as a Engineering Tool

Laser is acronym for "Light Amplification by Stimulated Emission of Radiation". The principle of a laser is to excite atoms to a high-energy state level and to get an inversion in population with respect to an intermediate level. When radiation interacts with the excited atom with a frequency that corresponds to the energy difference between the higher energy state of the atoms and the intermediate state with inverted population, it produces an emission of radiation with the same phase as the incidental radiation. It is possible to amplify this radiation by using a resonance cavity, in order to get a beam of coherent light. Besides its coherence, the emitted light is highly monochromatic which

enables efficient focusing. A laser can be used to heat or melt material locally. The coherent nature of the laser beam allows it to be focused to a small spot, leading to high energy density [40]. This property of a laser makes it possible to obtain very small spot sizes. Thus, a very high intensity (up to 1010 W/m2) can be attained. The medium used for laser determines the wavelength and quality of laser. The primary lasers available in market for high power applications are continuous wave CO_2 laser (wavelength 10.6μm), Nd:YAG laser (active entity Nd^{+3} with wavelength 1.06 μm) and excimer (lasing medium dimer a compound between is one inert gas atom and an halide atom, wavelength in ArF: 193 nm, KrF: 248 nm, XeCl: 308 nm and XeF: 351 nm). Nd:YAG laser have gained popularity primarily for the flexibility provided by fiber optical beam delivery making it suitable for many applications.

Laser-Matter Interaction and Laser Heating

The input of energy from pulsed/continuous wave lasers into the near-surface regions of solid involves electronic excitation and de-excitation within an extremely short period of time. The interest in these energy deposition techniques arises because lasers can be used to achieve extreme heating and cooling rates in the near-surface region (10^4-10^{10} K/s), while the total deposited energy (0.3-5 J/cm2) is insufficient to affect, in a significant way, the temperature of the bulk material. This allows the near-surface region to be processed under extreme conditions with little effect on bulk properties. The initial stage in all laser-metal processing applications involves the coupling of laser radiation to electron within the metal. This first occurs by the absorption of photons from the incident

laser beam promoting electron within the metal to higher energy states. Electrons that have been excited in this manner can divest themselves of their excess energy in a variety of ways. For example, if the photon is energetic enough, excited electrons can be removed entirely from the metal. this is the photo-electric effect, and in most materials, requires photon energies greater than several electron volts. However, the laser photons have usually much less energy (CO_2 laser 0.12 eV and Nd:YAG laser 1.2 eV). Hence, the electron that have absorbed energy from laser photon may not be energetic enough to leave the material, but they do have to lose energy to get back to ground state. This occurs when excited electrons are scattered by lattice defects. Such defects can be dislocation, grain boundary, lattice distortion (due to photon, thermal or other kind of stress). Consequently, the photon energy is converted to thermal energy.

Photon interactions with matter occur usually through the excitation of valence and conduction band electrons throughout the wavelength band from infrared to ultraviolet region. Since, free carrier absorption by conduction band electrons is the primary route of energy absorption on metals, beam energy is almost instantaneously transferred to the lattice by electron-photon interaction.

2.3.1 Laser as a Surface Engineering Tool

The first attempt at laser surface alloying was reported in 1964 [41]. However, the application of lasers in coating technology has developed rapidly only after 1980. Primarily, the development in laser technology has been responsible for this leap. Availability of various kind of lasers such as CO_2, Nd:YAG and excimer in adequate

power level and optical fiber delivery system has extended usability of laser in surface engineering and many other manufacturing processes. It has been recognized that by its very nature laser surface engineering has unique advantages over its conventional counterparts.

Characteristics of Laser Surface Engineering

1. Light is inertia-less, making it conducive to rapid processing.
2. Focused laser light provides high energy density.
3. Laser surface engineering can be carried out with/without atmosphere control.
4. Materials difficult to melt (such as ceramics, refractory metals) can be surface treated.
5. Precise and selected surface area can be surface treated.
6. Little or no contamination is involved.
7. Heat-affected-zone (HAZ) is narrow or absent.
8. Non-flat surface (e.g., inner diameter, non-regular surface) can be surface treated.
9. Coating is metallurgically bonded.
10. Laser can be time shared using fiber-optics to process multiple components simultaneously.
11. Laser treatment is amenable to automation.

Rapid Solidification by Laser

High power lasers provide coherent, monochromatic light that can be focused onto a very small spot of 0.1 - 1.0 mm. The intensity, thus, of the order of 10^{10} W/m^2 can be obtained. CO_2 and Nd:YAG laser are successfully applied for materials processing such as

welding, cutting, and to a lesser extent for heat treatment, melting and laser surface alloying. The most important feature of laser treatment is the localized melting of the surface material. This makes treatment of small surface areas possible without altering or affecting bulk properties and obviates the need for expensive alloying of the entire component. High power density (10^5 to 10^7 W/cm^2) in laser surface engineering produces a temperature gradient of the order of 106 K/cm [25]. Such a high temperature gradient, heat sink effect (of the rest of the components) and conduction mode of heat transfer result in a very high cooling rate or rapid self quench, sometime exceeding 10^9 K/s. This results in further grain refinement, may even produce novel metastable or amorphous phases. Solidification within the laser melt pool occurs rapidly once the laser beams has moved away. The rapid solidification, thus achieved, produces novel microstructure that is far-from equilibrium.

Laser Induced Combustion Synthesis

There are several difficulties in the applications of high power lasers on aluminum alloys as well. First, the high melting point of ceramics, which is close to boiling temperature of aluminum, requires a high energy density of the laser beam to melt ceramic coating. It will generate a strong convective flow in the aluminum melt pool. Eventually, it may lead to substantial surface roughness and may even destroy the ceramic coating. Secondly, the large difference of thermal expansion coefficient between aluminum (~ 22 μm/m K) and ceramics (mostly below 8 μm/m K) will introduce high stresses at the metal/ceramics interface during rapid cooling which may cause the interface bonding to fail. Finally, the

wetting of aluminum on most ceramics is usually poor and the rapid melting and solidification of laser process require a good wetting between liquid metal and solid ceramic within a very short period. Laser coatings on aluminum alloys with metals such as nickel, cobalt and manganese were not successful as the solubility of these metals in aluminum is rather low [5]. In case of such metal coatings, a typical microstructure developed with separated aluminum-rich and metal-rich parts [25].

In order to overcome these difficulties, a novel process for Al based systems was developed. The basic idea is to promote a chemical reaction at the interface between the metallic substrate and the ceramic particles. In this reaction coating, mixing powders of reactive ceramic (e.g. Fe_3O_4) with aluminum are used to laser coat aluminum alloy. Iron oxide was considered the appropriate choice of the coating material because like cast iron it is iron-based material, and unlike other ceramic materials (carbides, borides and some oxides) it does not provide extremely hard surface that can be detrimental to the mating surface. As mentioned in Section 2.2.3 laser can be used to ignite an SHS reaction. A reaction between Al and iron oxides in the surface layer induced by a laser can propagate into the material (in the direction of heat transfer) thus providing a thick coating thickness. Moreover, a higher temperature resulting from such exothermic reaction will further increase temperature gradient and cooling rate. A microstructure, thus resulted, would be much more refined compared to just laser melting. Further reinforcement by combustion reaction product is also expected to improve mechanical properties.

However, if such reactions are \quenched-in" by rapid solidification, it would result in a composite material with reaction-induced strongly bonded interface between the ceramic and the metal matrix. Furthermore, during synthesis of such composite

(ceramic/metal matrix) coating using laser surface engineering (LSE), the laser interaction is confined to a near-surface small volume compared to the substrate bulk. This provides a high cooling rate due to high temperature gradient and conduction mode of heat transfer through aluminum (substrate), effectively "quenching-in" the reaction thereby producing some novel, non-equilibrium phases and microstructure.

A coating or surface layer produced either solely by laser induced rapid solidification or non-equilibrium combustion synthesis is expected to enhance wear resistance of aluminum alloys and many other metallic system such as magnesium [42].

2.3.2 Surface Properties

As described above the surface related properties of a component are of primary importance. Mechanical properties such as surface hardness, wear resistance, erosion and abrasion resistance etc. determines suitability of a component. Surface related chemical properties such as corrosion resistance, pit resistance and stress corrosion cracking are also life-limiting factors for many components. Even crack propagation and fatigue initiates at surface and greatly influenced by surface conditions. Hence, the surface related properties of a component are of cardinal importance. Mechanical properties of a refined surface layer are expected to improve. Improvement in wear resistance is sought for application of these alloys. The laser induced surface modification of A319 alloy is expected to improve wear resistance of different flavors, such as erosion, abrasion, lubricated and dry abrasion resistance.

The sliding wear between two solids results in volume removal. Volume loss is a conventional comparative measure of wear. Weight or volume loss during wear is due to fracture subsequent to deformation until critical plastic strain incipient to fracture in very small regions. [43]. Usually these small volumes in and around the contact points may exist in the form of asperities that come in contact with the mating surface, which undergo elastic deformation, plastic flow, and fracture sequentially. It can be expected that materials having high plasticity and/or strain hardening characteristics would exhibit reduced wear rate, because it takes more plastic flow and/or plastic work to reach at the critical level of deformation to fracture. In other words, the ease with which the deformed metal may be torn off depends upon the toughness. Hence, wear behavior of monolithic coatings and especially composite coatings is a strong function of mechanical properties of the local microstructural features [9]. Such mechanical properties are hardness H [44], yield strength σ_y (σ_y is usually approximated as H/3 for a elastic-perfectly plastic material [45]), elastic stiffness S (resistance to deformation, quantified as the area under linear portion of stress-strain curve), fracture toughness and interfacial properties between phases and relative sizes of neighboring phases [46, 47, 48]. In case of a composite with ductile matrix, a hard secondary phase is often believed to reduce wear, as the presence of the hard reinforcement increases the effective hardness of the matrix, thereby reducing the penetration of the abrasive medium or the asperity of harder mating surface.

In this work, A319 alloy is chosen for two types of surface modifications. A laser beam is used to selectively melt and rapidly solidify the surface layer. There is no chemical composition change, but the microstructure is modified substantially. The

microstructure of such a system is a strong function of cooling rate. By controlling the solidification conditions, one can engineer the properties of Al-Si based alloy such as A319. It was essential to evaluate the temperature and cooling rate during LSE. The dynamic thermal conditions during LSE were measured using spatially and time-resolved infrared thermography. A simple mathematical model was used to analyze the data and calculate the thermal conditions. The instrumented indentation technique was employed to evaluate the mechanical properties of such a coating. The mechanical properties, and abrasion and wear test indicated improvement in the laser modified surface layer. In the second part of the work, it is attempted to synthesize a reaction composite coating of Fe_3O_4 on A319. The infrared thermography was employed to determine the thermal condition. The thermal diagnosis technique provided evidence of exothermic reactions in terms excess heat generated. The microstructural examination indicated formation of reaction products. The surface modified layer is evaluated using microstructural techniques. Mechanical properties are determined using instrumented indentation techniques. Abrasion and wear properties were evaluated using scratch and wear test. The flow diagram presented here summarizes the objective, approach and justification of the work (Figure 2.3).

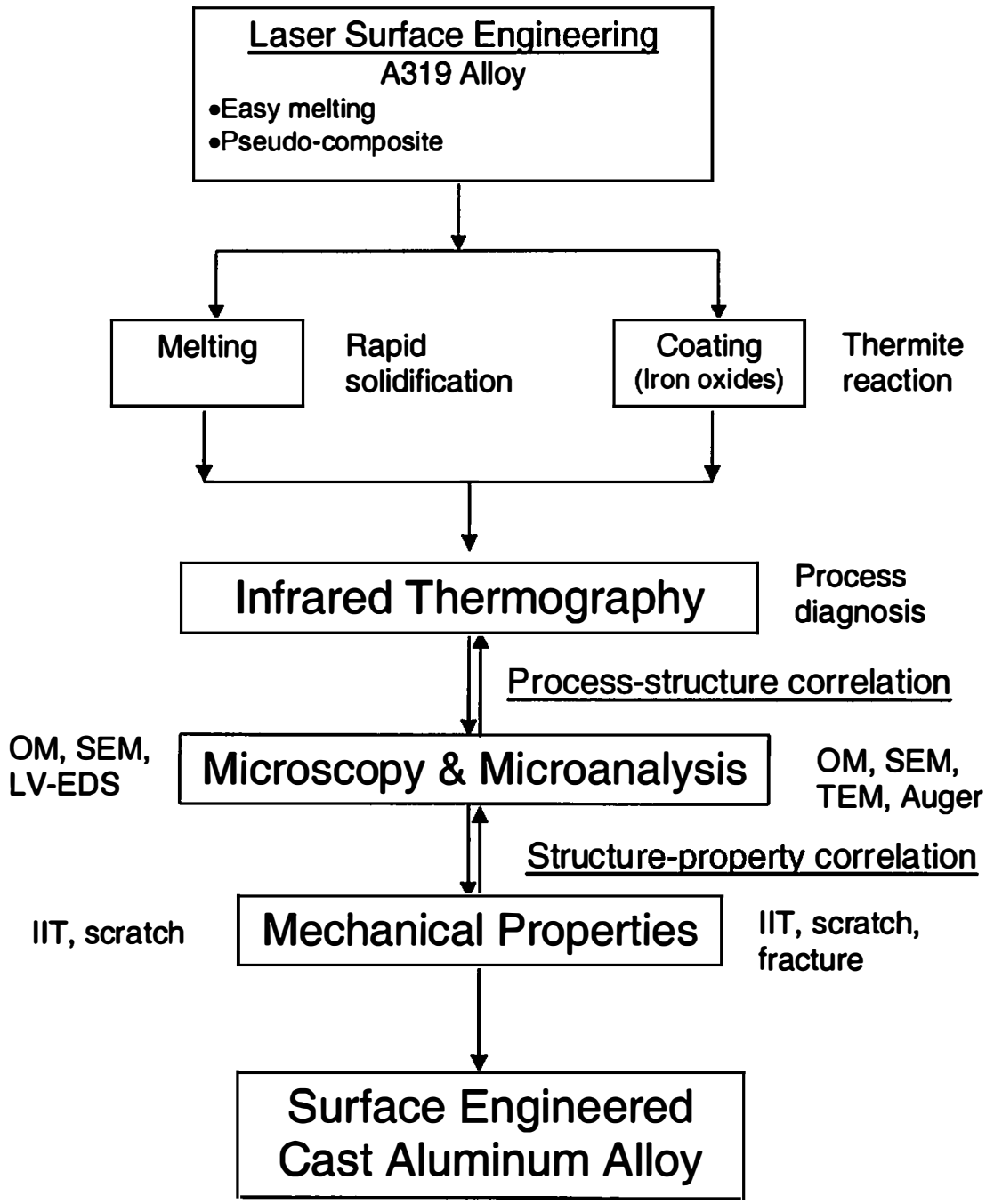


Figure 2.3: Flow diagram of the current work.

Chapter 3

Experimental Concepts

3.1 Materials and Processing

The A319 alloy (5.5 - 6.5 Si, 3.0 - 4.0 Cu, <0.5 Mn, < 1.0 Fe, < 0.1 Mg, <1.0 Zn, < 0.25 Ti, < 0.35 Ni, < 0.5 others (total) and balance Al, all in wt%) was used in the present study. Coupons of size 60mm x 60mm x 4mm were machined from A319 cast billets. These coupons were sand blasted to improve surface roughness for laser coupling. Then they were cleaned with soap and water followed by acetone and methanol, and oven dried for 30 minutes. Aluminum alloys possess high reflectance for most wavelengths in the visible light range including Nd:YAG wavelength (1.06μm). Problems in laser processing of aluminum alloys due to high reflectance have been reported [2]. For laser melting experiments, graphite paint (average paint thickness <10μm) was applied on these coupons to achieve initial coupling with laser, which remains high once aluminum is melted. For reaction coating experiments, commercially available Fe_3O_4 powders (99.5% purity, Reade Advanced Materials, Riverside, RI, average powder size <15 μm) were used in this study. The powder precursor, made of iron oxide (Fe_3O_4) suspended in a 10 wt% water based organic binder (proprietary formulation made from commercially available resins used in the paint industry) was spray deposited on A319 samples (60mm x 60mm x 5mm). The average precursor deposit thickness was 150±15mm. Sprayed samples were dried at 100°C for 1 hour prior to laser processing.

It was essential to verify that the higher temperature detected during laser treatment is due to heat of reaction and not enhanced absorption due to iron oxide precursor coatings. Two sets of parallel experiments were also conducted to study the thermal condition during surface coating, under similar laser processing parameters as those used during Fe_3O_4 coating. In the first set of experiments, graphite coated A319 alloy was laser treated under identical conditions. In the second set of experiments, the coupons were deposited with FeO. FeO has similar thermal properties and reactivity as Fe3O4, however a modest free energy of reaction. FeO is reduced by Al as per following equation [35].

$$\mathbf{3FeO + 2Al = Al_2O_3 + 3Fe}\ (\Delta G = -775.7\ \text{kJ/mol of Al at 1173 K}) \quad \mathbf{(3.1)}$$

A 2 kW Rofin Sinar continuous wave Nd: YAG laser equipped with fiber optic beam delivery system was employed for laser treatment of the samples. The lenses within the output-coupling module of the fiber optic delivery system were configured to provide a beam of about 600 μm diameter spatial distribution onto the sample surface to provide a rapid processing speed and limits the overlap between the laser passes to 20%. After few preliminary experiments with working distance, optics, lenses, beam profile, power and speed, the laser beam power was maintained constant at 2.0 kW and the beam traversed at a speed of 300-400 cm/min. The laser beam was traced in straight, overlapping stripes for entire coverage of the surface of the coupon.

3.2 Process Diagnosis

The mainstay of laser treatment is centered around fast thermal events. The fast cooling, rapid laser traverse speed, conduction mode of heat transfer and consequently rapid cooling rate can be used to our advantage. The rapid solidification is able to produce selective solid-state phase transformation, melting and even vaporization of surface [4]. It is, therefore, important to understand the thermal conditions during laser processing and its influence in consequent microstructure. However, measurement of temperatures during laser treatment is extremely difficult due to the rapid heating, non-steady state and high temperature gradients that are present. Lack of any reliable direct high-speed response non-intrusive techniques have prevented this step. Conventional techniques of temperature measurement such as thermocouple-based ones are limited due to their response time. A method using the electromagnetic radiation of a hot body to calculate temperature has a potential to solve this problem. In the present study, a state-of-the-art, high speed, and high sensitivity Raytheon Radiance HS IR imaging system was used to record the temperature during laser treatment. The IR camera had a 256 x 256 pixels focal-plane-array InSb detector, which was sensitive to 3.5μm wavelength thermal radiation. The infrared camera system is capable of capturing thermographic frames at 1-144 Hz. In the present work, it is set up to capture infrared image at 30 Hz based on initial trials for optimum incoming IR signal. The camera could be operated in a snapshot mode, and could be externally triggered. The temperature resolution of the camera was 0.015 °C. As seen in Figure 3.1, the camera was focused on a location covering a few

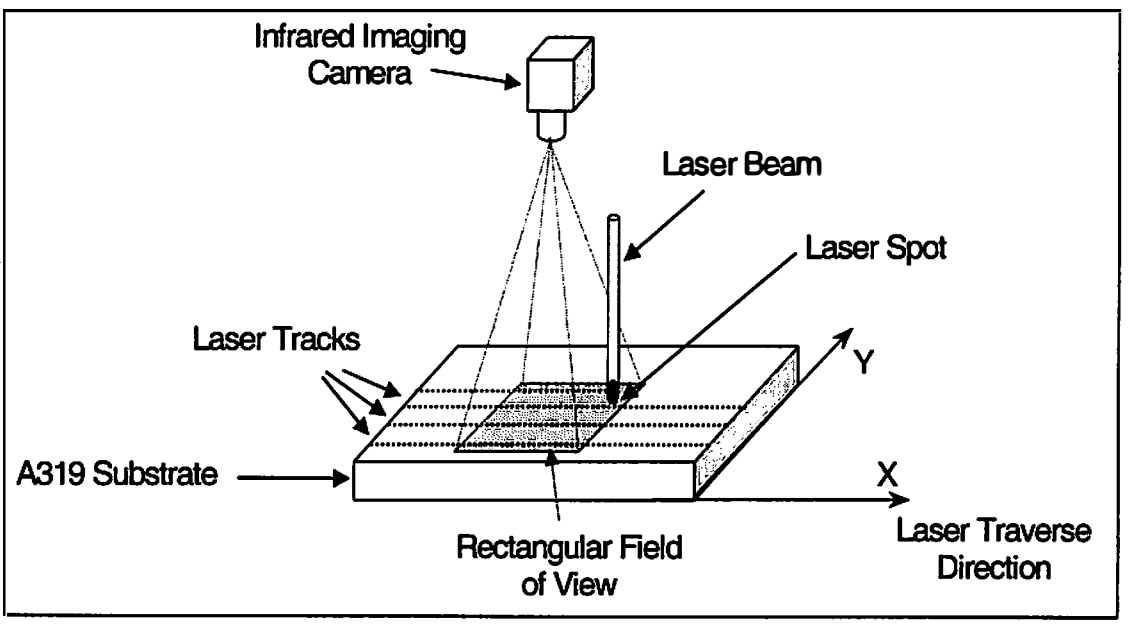


Figure 3.1: Schematic of the infrared thermography during laser processing.

tracks. The camera remained stationary while the laser beam traversed on the sample surface within the field of view of the camera.

In addition, the IR imaging system can be coupled with the laser treatment system through a synchronizer to trigger the IR camera to record data at a certain time delay such that any phase lag of data recording was avoided. The IR thermography camera recorded the intensity of infrared light in digital form. The pixel size was 20 microns x 20 microns. The infrared thermograph is an array of intensity values of pixels covering entire surface as a function of time as seen in Figure 3.2. The recording (of 3 laser tracks) was done 30 frames per second for laser traverse speed of 325 cm/min. Energy is emitted by a hot body, such as the laser processed samples, in the form of electromagnetic radiation. Most of the energy emitted in the temperature range of the laser processing would normally be in infrared range. The intensity of any particular wavelength is a function of temperature and emissivity (ε) only. In the current study, attempts were made to measure temperature from intensity value at a particular wavelength. Hence, experimental calibration was necessary. For calibrating the infrared intensity (I) thus measured for actual temperature (T), actual samples were heated from room temperature to 600^{o}C in a closely controlled black hole furnace. The sample was kept in the center of the black hole. As the temperature of the furnace was raised, the IR intensity was recorded corresponding to the furnace temperature. The samples were heated at the highest possible heating rate (40oC/min) so that far-from-equilibrium condition is maintained. The temperature of the sample was trailing behind furnace temperature during heating. Hence, the intensity was recorded with IR camera along with temperature with a rapid response thermocouple

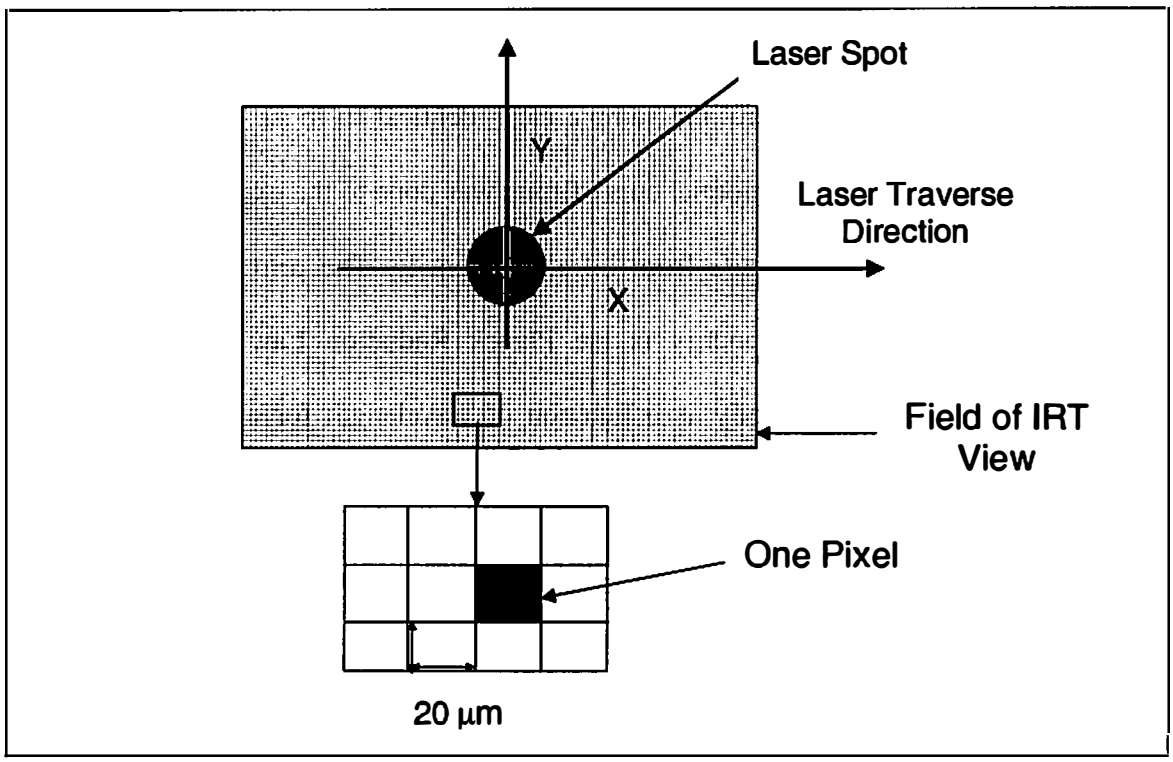


Figure 3.2: Pixels of an infrared thermograph during laser processing.

(coupled with the control thermocouple to reduce error) attached to the sample. It was not possible to calibrate beyond furnace temperature 600°C because it was difficult to maintain a good thermocouple-sample contact beyond that temperature as the sample starts softening (melting point is 485°C). Care was taken to keep camera setting (filters, lenses, distance between camera and sample etc.) identical to those used for recording during laser treatments. A polynomial curve fitting was done to the experimental data and was used to estimate temperature from infrared intensity. The primary law governing radiation of electromagnetic energy is the Planck Radiation Law. The intensity of radiation emitted by a blackbody as a function of wavelength for a fixed temperature under equilibrium condition is given by Equation 3.2.

$$I(\lambda,,T) = \frac{2hc^2}{\lambda^5} \frac{1}{e^{\frac{hc}{\lambda k}} - 1} \qquad (3.2)$$

where, λ is the wavelength of electromagnetic radiation, **T** is the temperature in Kelvin, **h** is the Planks' constant, k is the Boltzman's constant and **c** is the velocity of light. The emission of energy by a hot non-black body, such as the laser processed samples, is given by Stefan-Boltzmann law (Equation 3.3).

$$\frac{dQ}{dt} = \varepsilon \sigma T^4 \text{ x (Area)} \qquad (3.3)$$

where ε is the emissivity and σ is the Stefan's constant. This relation gives the total energy radiated per unit time over the entire electromagnetic wavelength range. In the current study, intensity value in a particular wavelength is used to measure temperature of the spot. Hence, experimental calibration was necessary.

The temperature of laser remelt sample and iron oxide on A319 can provide information if there is additional heat due to exothermic reactions [Equations 2.5 and 3.1]. For calibrating the infrared intensity (I) thus measured with actual temperature (T), a painted sample was heated from room temperature up to 600°C in a closely controlled black hole furnace and the intensity was recorded with IR camera along with temperature with thermocouple attached to the sample. Care was taken to keep camera setting (filters/lenses etc.) identical to those used during laser treatments. Experimentally, it was not possible to go beyond the explored temperature range (100 - 600°C). These two red equations as well as the calibration curve in Figure 3.3 indicate that the sample was very close to black-body as far as emission of infrared radiation is concerned (i.e., ε in Equation 3.3). Furthermore, the correlation factor (R^2) of very near to 1 indicates that the curve fitting is excellent. In view of good curve fitting, fourth order temperature dependency similar to Equation 3.3, and the sample behavior similar to a black body ($\varepsilon \sim 1$), it was considered appropriate to extrapolate the I-T relation for the sample beyond the experimental range to determine temperature from the intensity. To find out T of the sample, the value of corresponding I was substituted in Equation 3.5 and the equation was solved. The only real positive root of relation was accepted as the T. A polynomial curve fitting was done to the experimental data and was used to estimate temperature from infrared intensity. The order and shape of the curve for sample is similar to that obtained for black body (furnace). The emissivity coefficient undergoes only minor changes over the temperature range as shown in Figure 3.3.

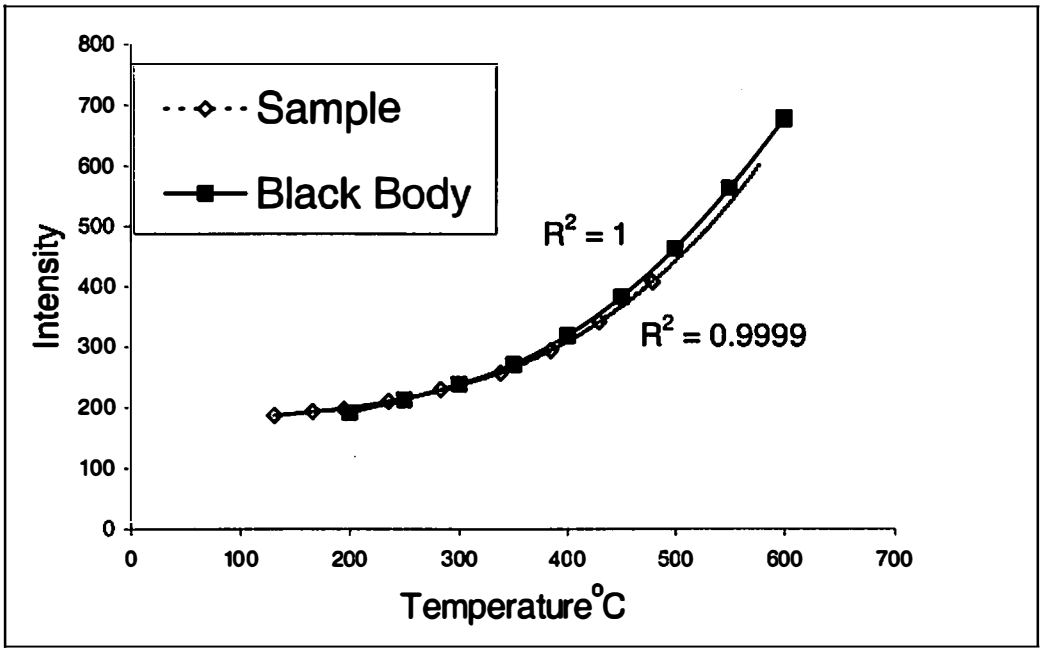


Figure 3.3: Calibration of temperature vs. infrared intensity.

Intensity, I, is related to temperature, T through a fourth order polynomial curves fitted with the experimental data for the black-body (furnace) (Equation 3.4) and the samples (Equation 3.5) respectively.

$$I = -1x10^{-8} T^4 + 2x\ 10^{-5} T^3 - 0.0105\ T^2 + 2.6006\ T - 51.723 \quad (3.4)$$

$$I = 2x10^{-9}T^4 + 5x10^{-7}T^3 + 5x10^{-05}T^2 + 0.081T + 174.57 \quad (3.5)$$

Considering, power - 4 dependency of total energy emission (I) on temperature, it is not surprising that the single wavelength intensity (I_λ) is related to temperature by a 4th order polynomial. The correlation factor (R^2) of very near to 1 indicates that the curve fitting is excellent. To find out T for a corresponding I, the value of the value of I was substituted in Equation 3.4 and Equation 3.5 and the equation were solved to estimate T.

3.3 Microscopy and Microanalysis

For microscopic examination, the laser-processed samples were cross-sectioned, mounted and mechanically polished to mirror finish and, wherever desired, etched with Keller's reagent. For scanning electron microscope (SEM) imaging heavy etching was employed to provide better topographical contrast in secondary electron (SE) mode. Colloidal silica 0:3μm was used for final polishing for instrumented indentation characterization. Colloidal silica is known to be slightly acidic and thereby removes the stressed top layer. General characterization of laser-processed samples included cross-sectional examination of the coating and interface using an optical BX60M Olympus (Olympus, Melville, NY) microscope.

The resolution of a microscope is limited by the wavelength of the source of illumination. Hence, to reveal microstructural feature finer than that one has to go to higher resolution microscope such as a scanning electron microscope. Laser processed samples thus prepared were examined using FEI XL30FEG model SEM and Hitachi 4500 SEM. Both secondary and back-scattered modes were employed depending on sample, particular feature being examined and convenience. The raw image digitally captured or produced by a electron microscopic examination contains several artifacts and noise rooted in electronics, lens, alignment, vibration and other factors. Primarily noise can be divided into random noise and systematic noise. An important feature, if to be revealed above background, should have a reasonable signal-to-noise ratio (SNR). It has been reported that for distinction from the background, the SNR value should be at least 10. Random noise can easily be suppressed by means of digitally "averaging" several images of same microstructure. This is implemented by software while capturing high quality images. Other principles such as wavelet improvement by FFT and logarithmic intensity were used in certain cases. These and other image enhancing capability have been used in current work.

Besides, magnified view of the microstructure, it is often necessary to determine the phases present. The crystallography features such as type and interplanar distance of uniquely identify all phases. Structural characterization for phase identification on a Philips Norelco X-ray diffractometer with CuK_{α} radiation operated at 40kV and 20mA.

3.3.1 Energy Dispersive X-Ray (EDS) Microanalysis

High-energy electron and matter interactions often produce x-ray. Depending on the excitation voltage (kinetic energy of electrons) and the elements present in the matter, beam electrons knock of bound electrons from the ground (unexcited) state. As the electrons falls back from high-energy state to ground state, the extra energy associated is emitted in the form of electro-magnetic radiation, possibly in the x-ray regime. Since the difference between ground state and excited state is well defined for chemical elements, the intensity and wavelength of x-ray radiation (above background) can be utilized to find the spatially resolved chemical composition of the sample. EDS microanalysis has proven to be a very useful tools and now is a popular attachment with most electron microscopes (SEM, TEM, STEM). The detector in this unit is a 1024-channel Li-doped Si crystal which records the x-ray photon counts (intensity) as a function of energy over a period of time. Laser processing is known to produce many non-equilibrium phases. Often, the microstructural features are distributed finely. Hence, it is essential to determine approximate chemical composition of these features. An EDS system attached to the SEM was used for this purpose.

The Energy Dispersive Spectroscopy (EDS) signal comes from the volume of matter excited by an electron beam. The higher the voltage, the larger is the volume from which signal is registered by the detector and thus lower is the spatial resolution. The problem with higher voltage is the lateral resolution of such analysis spot is compromised. It is, therefore, required to reduce excitation volume to improve resolution. However, the low voltage represents lower energy of electrons that generates x-ray. The

x-ray thus produced is often from low-energy (outer shell) of atoms due to the low energy difference between outer shells. It is less sensitive and often overlapping peaks of different elements are hard to distinguish. Hence, voltage and resolution need to be optimized. By choosing an appropriate low voltage (LV), it is possible to analyze microstructural features with high resolution. Since laser modification generates extremely refined microstructure, LV-EDS was employed to analyze the samples.

3.3.2 Scanning Auger Microanalysis

Scanning Auger Microanalysis (SAM) utilizes the Auger electrons emitted from near surface atomic layer to analyze the chemical content of sample. Owing to the low energy range of Auger electrons, few nanometers thick top layers on surface can be analyzed. Also, as the yield of Auger electrons increases with a decrease in atomic number, SAM is useful for analyzing low atomic number elements like H, C, and O etc. SAM was employed because it is capable of detecting light elements like O. This analytical technique is also most suitable to study the fracture surface created *in vacuuo*. The analysis of a pristine surface thus created provides information about dissolved oxygen. A surface that is exposed to atmosphere, even briefly, absorbs and/or adsorbs oxygen and gets contaminated. Therefore, this procedure of creating fracture *in vacuuo* to quantify oxygen dissolved in the bulk of Fe_3O_4-Al composite region is most suitable. SAM was carried out using a PHI 680 SAM (Physical Electronics, Eden Prairie, MN) at the High Temperature Materials Laboratory of Oak Ridge National Laboratory. Auger analyses were conducted to investigate various physical, microstructural and chemical aspects.

The Auger spectra were obtained with an accelerating potential of 10kV and the beam current of 10nA operated in a vacuum better than 10^{-10} torr. Two types of samples were analyzed, several as-polished cross-sectional samples and several samples that were fractured in-vacuuo. The sample was polished before insertion into the analysis chamber and then ion sputter cleaned in-situ prior to analysis. Since polished and air exposed surfaces adsorb oxygen, water vapor and other gases, ion sputtering was conducted using Ar ions at 3.5kV which produced a sputtering rate of 167 Å/min to remove the entire layer of adsorption prior to quantitative analysis of the sample surface. As the adsorption-film disappears, the composition tends to reach asymptotically a constant value. Analysis was completed before re-contamination of the surface. It was, therefore, possible to detect O dissolved in the coating material. Fracture samples of 22 mm × 3 mm × 3 mm were prepared in the cross-section that included both coating and substrate material regions. A notch perpendicular to both the length of the sample and the interface between the coating and substrate was made. Auger spectra of pristine surface were obtained from the surface fractured *in vacuuo*. The elemental spectra were analyzed for possible phases. To ensure reproducibility several chemical spectra were taken both from as polished and ion-sputtered cross-sectional samples as well as from the *in vacuuo* fractured samples.

3.3.3 Transmission Electron Microscopy

As the name suggest in "transmission electron microscope" (TEM) a beam of electron transmits through the samples. The internal structure is revealed at very high magnification as the beam transmitted through the sample causes fluorescence on a

screen. With the help of electro-magnetic lenses, very high resolution can be achieved. Since the electron-matter interaction is rather strong, the sample must be transparent to obtain any meaningful signal out of the images. A focused ion beam was used to make sample electron-transparent and thus suitable for examination in a TEM. A FEI (formerly Phillips) 200kV Tecnai 30 TEM was used to examine the microstructure. EDS and Selected Area Diffraction (SAD) pattern were used to find out chemical composition and crystal structure respectively of microstructural features.

3.4 Mechanical Properties

Tribological performance of the composite coating is greatly dependent upon mechanical properties of the coating. Such mechanical properties are hardness H [44], yield strength σ_y (σ_y ~ 0.3-0.4 times H [45]), elastic stiffness S, fracture toughness and interfacial properties between phases and relative sizes of neighboring phases [46, 47, 48]. Hence, it is expected that a tough, particle reinforced composite coating would provide better wear resistance compared to as-received A319 alloy, especially where dimensional tolerance is uncompromisable. The evolution of a refined microstructure is expected to improve these mechanical properties. The modified surface layer was evaluated to verify improvement in mechanical properties. Four-point-bend-test were initially attempted. It was difficult to measure the properties due to composite nature (coating and substrate are metallurgically bonded), high ductility of the modified layer and relatively lower flow stress of the substrate. Instead a localized property measurement technique such as "Instrumented Indentation Technique" (IIT) was employed.

3.4.1 Instrumented Indentation Technique

In IIT, hardness (H) and elastic modulus (E) are determined from the contact stiffness (S) experienced by the depth-sensing indenter. As a result, the E and the H measured at different depths reflect their variation as a function of a confined affected volume (~10 times the corresponding indentation depth). Moreover, the load-displacement curve contains information regarding initiation of cracks, if any. It is essential to determine the effect of microstructure refinement on mechanical property. In light of this, IIT has been used for determining hardness and elastic modulus of the laser-refined surface layer. The additional advantage of IIT over its more traditional counterparts is that the mechanical property from point to point can be probed. On the contrary, most other techniques provide only the "averaged out" property and miss information about contributions of the discrete constituents. Mechanical property measurement was carried out on the NANOINDENTER II ™ at the High Temperature Materials Laboratory (HTML) of the Oak Ridge National Laboratory (ORNL). The instrument was factory calibrated. A Berkovich tip was calibrated for area function using pure aluminum and fused silica standards and was found to exhibit minimal variation for indentation depths, h, ranging from 25 nm to 1200 nm. In nanoindentation, a prescribed load is applied to a pyramidal or spherical indenter in contact with the specimen surface. As a load is applied to the indenter, the depth of penetration into the specimen is measured. A nanoindentation test instrument provides experimental results in the form of a load-displacement curve for the loading and the unloading parts of the indentation process. An analysis of the unloading

data provides a value for the depth of the circle of contact at full load. The area of contact at full load is determined from the known angle or radius of the indenter. The hardness is found by dividing the load by the area of contact. The slope of the unloading curve provides a measure of elastic modulus.

Using the known physical properties of standard aluminum and fused silica, an area function, A, (curve fitting in terms of depth, load, and corrections) was determined. The reduced elastic modulus using this area function was constant throughout the indentation depth range (25-1200 nm). To account for tip rounding, the Hertzian relation was used for very low indentation depths. (The tip radius was less than 50nm.) This area function was later used for calculation of the nanoindentation data. Nanoindentation can be carried out in different modes; (1) displacement mode: the total displacement (indentation depth) is traveled in equal intervals, (2) strain rate mode: the strain rate during displacement is kept constant; (3) load mode: the load is increased at equal increment until the pre-specified load is attained. Different modes can be applied depending upon the information being sought from experiments and on the material. After an initial observation of the material being strain rate independent (under various strain rate mode) displacement mode was employed for evaluating mechanical properties of the material.

Samples were metallographically polished to a mirror finish. Nanoindentation data were recorded with indentations made at a distance interval of 25 microns from the surface in the laser modified rapidly solidified region using a Berkovich indenter as seen in the Figure 3.4. Such experimentation was carried out with several indentation-depths up to 1000 nm. Also, a series of load-controlled indentations was carried out for 150 mN

(corresponding depth ~ 2200 nm) for analyzing if there is any strain dependency, crack initiation and/or discontinuity in load-displacement curve. Measurements were done for various indentation-depths to determine depth dependency and to estimate the extent of heterogeneity. Several tracks of indentation (number of indentations ~ 100) were traced within the coating regions from edge of the coating towards the substrate for each depth (Figure 3.4), to provide a good statistical sampling. Each indentation consisted of six steps. During step 1, the indenter approached the sample surface. The sample was loaded to different depths (100 nm, 200 nm, 1000 nm and 2200 nm) during step 2 and held at this stage. The holding period was referred to as step 3. The fourth step was an unloading step to 80% of load. The indenter was still in contact with the sample surface when a hold period (step 5) of 60 seconds was introduced to sense thermal drift, which was used to correct the load-displacement curve during elastic modulus, E and hardness, H computations. Step 6 was the final unloading segments. The E and H computations were carried out based on an analytical technique developed by Oliver and Pharr [49, 50]. In the displacement mode indentation process, the instrument senses and records the depths (h) and corresponding contact stiffness (S). The above-mentioned technique uses the load (P), depth (h), area function (A) and the contact stiff ness experienced by indentation machine (S) data to determine E and H. The correlation between physical properties and measured parameters are presented in Equations 3.6 and 3.7 from Ref. [49]:

$$H = \frac{P}{A} \tag{3.6}$$

$$E_{reduced} = \frac{\sqrt{\pi}}{2} \times \frac{S}{\sqrt{A}} \tag{3.7}$$

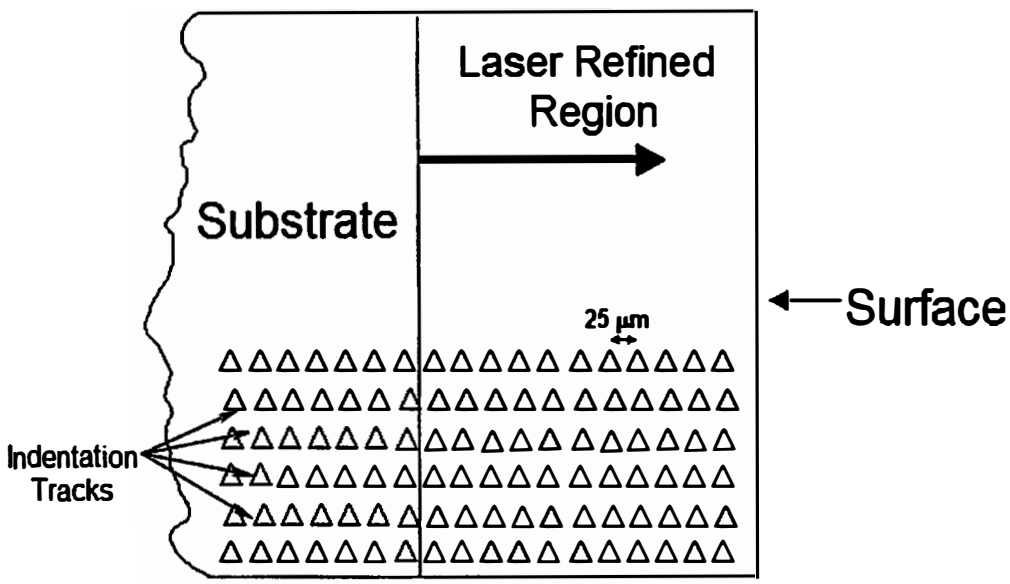


Figure 3.4: Indentation impressions on cross-section of the laser-modified samples.

It is, therefore, possible to find "averaged out" mechanical properties as a function of depth. In a composite material consisting of widely different constituents (in terms of hardness), the contact stiffness S [as in equation 3.7] recorded would depend on whether the indenter hits the harder phase, the softer phase, or the interface region. However, as depth of indentation increases, the S would be a result of the weighted average of the composite material. If a large number of reduced elastic modulus $E_{reduced}$ [derived from contact stiffness and area function as per Equations 3.6 and 3.7] versus depth of indentation ($E_{reduced}$ versus h) data points are plotted, at the lower h end it is expected to segregate into two groups corresponding to two distinct components of the surface material. To find out if such a phenomenon was present in the current materials system, the depth-reduced elastic modulus (h vs. $E_{reduced}$ data points (>5000) were plotted.

After initial observations indicated that nanoindentation using the Berkovich indenter was unable to produce any cracks in the laser-modified region, a cube corner indenter was used. Indentation was carried out for 5 different loads (400 mN, 200 mN, 100 mN, 50 mN and 20 mN) in load-control mode, intended to determine the threshold load for cracking and resistance to fracture. (both Berkovich and cube-corner indenters are 3-sided pyramidal tip with the angle between axis of symmetry and a face is 65.5° and 35.0° respectively). Since a cube corner indenter is of much sharper geometry, the threshold load for cracking is much less [51]. Hence, it was considered better suited to determine the resistance to fracture of the materials with toughness that was outside the regime of Berkovich or Vickers diamond. Both Berkovich and cube-corner indentation impressions were analyzed by optical and scanning electron microscopy to determine whether cracking and/or separation of microstructural constituents had taken place.

Both Berkovich and cube corner indentation impressions as well as load-displacement traces were analyzed by optical and scanning electron microscopy to determine cracking and/or separation of microstructural constituents and other features such as pile-up, sink-in, etc.

3.4.2 Abrasion and Wear

Another method of mechanically testing a specimen surface, particularly a coating, is scratch testing. In fact, scratch tests provide insight to mechanisms of deformation, material removal and evaluate the adhesion of a surface coating to a substrate, making it more akin to tribological properties than a vertical, quasi-static hardness test [52]. Also, measured scratch hardness potentially can be used to rank materials for two-body abrasion resistance. Hence, scratch tests were carried out to evaluate such a composite material.

A low-speed bench-top scratching machine [Revetest, CSM, Neuchatel, Switzerland] equipped with an spherically rounded conical diamond tip (Brale) stylus to produce a scratch with a single pass was employed in the present study. The tip radius was 200 μm. A number of scratches were carried out on buffed and polished flat samples under different normal loads. The scratch of 5 mm length was done at constant speed 100 microns/sec. The width of each scratch was measured at least at 3 different spots (avoiding the ends of each scratch) and scratch hardness (HS, in GPa) was calculated from the projected area of the sliding stylus as follows (see also [52]).

$$H_s = c\left(\frac{P}{w^2}\right) \qquad (3.8)$$

where, P is the applied load (grams-force), w is the scratch width (micrometers), and c is a geometric constant equal to 24.98 in the present case [52]. A scratch test is not strictly a wear test. It is a measure of a surface's resistance to abrasion by a hard point. Therefore, uses of the term wear, which implies a progressive removal of material, not truly applicable. Since these surface modifications are primarily aimed to enhance wear resistance, it was essential to evaluate tribological properties with respect to the substrate.

Tribological properties of laser-modified samples were measured using a block-on-disk tribometer. The coupons of dimension 20mm x 15mm x 4mm were tested for dry sliding wear against a hardened steel disk (R_c 60) rotating at a constant linear speed of 4.4 m/s. Weight loss measurements were made in pre-decided intervals. The dry sliding wear test was conducted for a total of 30 minutes duration with different applied normal force of 10 N. It is mentioned here that, to begin with, there was only a line contact between the disk and the sample (15 mm long).

3.5 ThermoCalc

ThermoCalc™ is a phase prediction software. Using thermodynamic data and phase interaction parameters of individual elements, it can predict equilibrium phases present in a multi-component thermodynamic system under the given condition. The option of deliberately including and excluding phases, based on experimental observations, it is very convenient to pin-point phases possible both under equilibrium as well as non-equilibrium conditions. The calculations are based on thermodynamic databases produced by an expert evaluation of experimental data. Each equilibrium calculation involves

setting up and solving mathematical problem that, in ThermoCalc, involves solving a set of non-linear equations. Generating a phase diagram usually involves many such calculations. The Window-based user friendly (GUI) TCW was used for phase prediction in the laser treated samples. Knowing the laser treated samples are non-equilibrium phases, it gave a comparative picture with equilibrium phases. ThermoCalc can be used to calculate

- Phase Diagram (binary, ternary, isothermal) up to 2 independent variables.
- Thermodynamic properties of pure substance, compound and solution phases such as enthalpy, heat capacity and activity.
- Driving force for formation of phases.
- Metastable transformations such as non-equilibrium solidification simulation with the Scheil-Gulliver methods.

Since laser processing is a non-equilibrium one, to study the effect of such a processing, it was essential to know the thermodynamically feasible phases. Knowledge of possible equilibrium phases does help to evaluate the microstructure better. Moreover, the Scheil-Gulliver method can be employed to predict approximately the phases expected in rapid solidification of A319 alloys. Scheil-Gulliver method is based on solidification calculation in given number of temperature steps based on assumption that there is no diffusion in solid and infinite diffusion in liquid. It is often useful to predict phases formed under rapid solidification. In the present work, this method was employed to calculate solidification temperature under non-equilibrium condition,

Chapter 4

Results and Analysis

In this chapter, the results of various experiments are discussed. As mentioned earlier, two approaches were taken to modify the surface of A319. In the first approach laser is used to rapidly solidify the surface layer without any deliberate chemistry alteration. In the second approach, it is attempted to exploit a strong affinity between iron oxide and aluminum to form a reaction coating. A high power laser is used to trigger reaction between iron oxide precursor and aluminum and thereby form a reaction coating.

4.1 Laser Melting and Rapid Solidification

In this technique of surface modification, the surface layer of A319 is rapidly heated by a high power laser. As the laser traverse, the melt-pool thus formed solidifies rapidly due to conduction mode of heat transfer and heat sink effect. Hence, the thermal conditions are considered primary process variables. The following sections deal with process diagnosis, microstructure evolution and property improvement thus ensued. Attempts are also made to establish process-structure-property correlations.

4.1.1 Thermal Conditions During Processing

Conditions during solidification determine the microstructure, which in turn translates into material properties. Therefore, it is important to understand the solidification

parameters, namely temperature, thermal gradient and cooling rates. One can get an insight into these thermal conditions by exploiting the thermal radiation emitted from any object at a temperature above absolute zero. The emission of energy in form of electromagnetic radiation by a hot non-black body, such as the laser processed samples, is given by Stefan-Boltzmann law (Equation 3.3). This relation gives the total energy radiated per unit time over the entire electromagnetic wavelength range. In the current study, attempts are being made to measure temperature from intensity value at a pre-selected wavelength range. Hence, experimental calibration was necessary. As explained in Section 3.2, calibration beyond furnace temperature 600°C (sample temperature ~ 480°C) was not done. A polynomial curve fitting to the experimental data was used to estimate temperature from infrared intensity. The intensity vs. temperature data was plotted in Figure 3.3. Intensity, I, is related to temperature, T through fourth order polynomial curves fitted with the experimental data for the blackbody (furnace) (Equation 3.4) and the samples (Equation 3.5) respectively.

A typical temperature distribution along the laser traverse direction recorded in a single typical frame is presented in Figure 4.1. The instantaneous temperature of the laser melt pool is significantly higher than that in the nearby region. The steep slope just behind and ahead of laser melt pool (left side of the crest in the graph is cooling and that on right side corresponds to heating) indicates the high thermal gradient. Also, just ahead of the melt pool (right side of the crest) a local maximum is observed. This can be attributed to superheating just before melting. Higher heating rate (intrinsic to laser

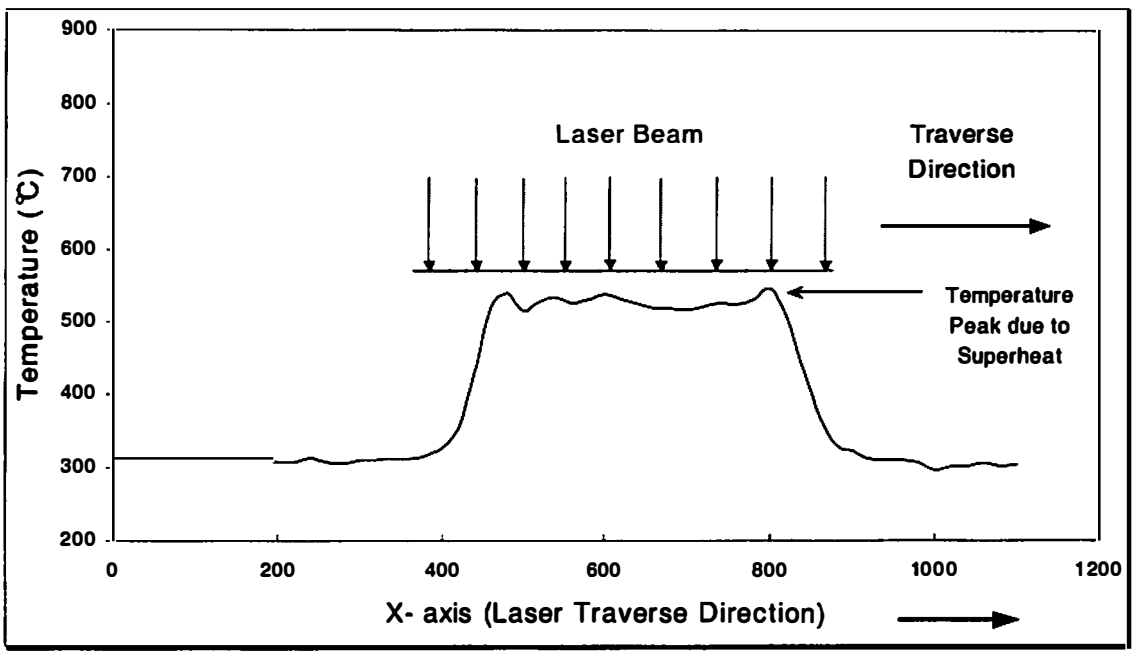


Figure 4.1: Temperature profile along the laser traverse path.

surface engineering) requires higher superheating. The maximum intensity observed in each frame gives the "averaged out" intensity over time duration of $\frac{1}{30}$ s. To determine the maximum temperature during laser treatment several (10) such readings were taken in equal intervals and the average of values (T calculated from I) is presented in Table 4.1.

Infrared experimental measurements of temperatures during laser surface engineering are complicated by non-uniform surface emissivity caused by surface roughness, laser plume/plasma obstructing the IR camera field of view, melting, and surface disturbances thus ensued. However, in absence of any better method, it was assumed that the I-T relation is valid in the entire range of experiments. This is further emphasized the by observed temperature arrest in the melt-pool shown by more or less constant temperature in Figure 4.1. Laser processing is usually associated with high cooling rates resulting in non-equilibrium microstructure and phases. Estimation of cooling rates assumes even more significance when solidification microstructure is being investigated. It is, therefore, crucial to estimate instantaneous and local cooling rates. The laser traverses at a speed of u_x is 325 cm/min, equivalent to ~2750 pixels per second. At 30Hz recording speed, the laser beam traverses about 91 pixels from frame to frame. Therefore, it was not possible to directly estimate local instantaneous cooling rate from the experimental data. Instead a mathematical approach was taken. There exists a volume of work on heat transfer modeling in welding. Two- and three-dimensional equations are available for describing primarily welding phenomena [53, 54, 55, 56]. However, in case of laser surface engineering (LSE), the traverse speed of heat source is much higher than welding. Furthermore, the heat source is much more confined in case of LSE compared to

Table 4.1: Maximum temperatures during laser melting.

Location	Maximum Temperature, T_m (°C)	Standard Deviation (%)
Laser Track 1	569	1.3
Laser Track 2	578	1.9
Laser Track 3	589	2.5

welding. During LSE, heat transfer in -X direction (opposite to laser traverse direction) dominates. The temperature gradient, as evident from Figure 4.1, is very high. Therefore, the welding models may not be applicable as it is, and the problem can be simplified further. Hence, the equation for heat-transfer in 1-dimension can be used. The sample being laser treated is large compared to instantaneous laser interaction volume. Therefore, the laser-material interaction zone can be assumed as moving origin. It is further assumed that the rectangular shape of the beam and heat distribution within this rectangle does not affect the cooling rate. For finding out the surface-cooling rate, either non-steady state (time dependent) equation or steady state (time independent) equation for moving heat source (origin) can be applied. Usually, for mathematical models of welding process, a steady state is considered [53, 54, 55, 56]. However, the very rapid process associated with laser processing makes it worthwhile to examine both the methods. The interaction volume in LSE is much smaller and superficial compared to fusion and laser welding. The non-steady heat transfer equation for a moving heat source, is given by the following equation [55] relating the `substantial derivative' of temperature as a function of time and position [T = T(x,t)] with the partial derivatives.

$$\frac{D}{Dt}[T(x,t)] = \frac{\partial T}{\partial t} + u_x \frac{\partial T}{\partial x} = \alpha \frac{\partial^2 T}{\partial x^2} + \frac{\dot{q}}{c_p \rho} \qquad (4.1)$$

where u_x is the velocity of moving heat source (laser), c_p is the specific heat, ρ is the density, α is the $\frac{k}{c_p \rho}$, k is the thermal conductivity, $\dot{q}$ is the constant heat generation term (due to the latent heat of fusion at the solidification front, exothermic reactions, etc.). The steady state relation is a special case of the unsteady state heat transfer relation (Equation 4.1). When the temperature distribution attains steady-state, $\frac{\partial T}{\partial t} = 0$,, otherwise it is a non-zero term. The left hand side of Equation 4.1 is the cooling rate, $\frac{DT}{Dt}$ experienced. For simplification, it is assumed that at any given instant the laser beam interaction region is away from the pixel of maximum cooling rate and does not contribute extra heat. This is reasonable, as significant cooling takes place only after the laser beam has moved away. In the finite difference term, the cooling rate can be estimated from pixel array double derivative in the X-direction. Equation 4.1 can be rewritten as follows.

$$\frac{DT}{Dt} = \alpha \frac{\Delta\left(\frac{\Delta T}{\Delta x}\right)}{\Delta x} + \frac{\dot{q}}{c_p \rho} \qquad (4.2)$$

The second term (heat generation term) in the right hand side of Equation 4.2, i.e., release of latent heat of fusion due to solidification of unit volume in X-direction, was found to be negligible compared to the 1st term (<2%). Hence, cooling rates were calculated neglecting this term for several frames (~10) within each laser track. The

cooling rate is primarily determined by temperature gradient $\frac{\Delta T}{\Delta x}$. Thus, the maximum surface cooling rate was experienced in the direction opposite to laser traverse direction. Since the temperature gradient within a track is very different from frame to frame as the laser has already moved 90 pixel between each frame, the corresponding cooling rates vary significantly. Hence, cooling rate corresponding to highest temperature gradient in a frame was calculated. Several such frames were analyzed and found to possess minimal variations (<5%). Also, the corresponding temperature of maximum gradient was calculated. The average values are presented in Table 4.2. It can be noted that the temperature corresponding to maximum gradient T_{mg} is different (significantly lower) than the average maximum temperature, T_m, recorded (Table 4.1). This is obvious as the highest temperature corresponds to over-heated liquid in the melt-pool and the maximum gradient occurs on the periphery of the melt-pool where the solidification front is. In non-steady state, generally the instantaneous temperature gradient is higher compared to steady state and correspondingly it is expected to indicate a higher cooling rate. However, it is possible for a moving origin at the heat source to achieve steady state with the material. From the Tables 4.1 and 4.2, it can be seen that the average maximum temperature T_m, average temperature of maximum gradient T_{mg} maximum temperature gradient $\frac{\Delta T}{\Delta x}$ and cooling rate $\frac{DT}{Dt}$change only very gradually from track 1 to track 3. Also, the standard deviations corresponding to readings taken within each track were within 5%. This is an indication of the conditions being close to steady state. Therefore, attempts were made to calculate the cooling rates assuming a steady state heat transfer for

Table 4.2: Surface cooling rate under non-steady state. Estimated using Equation 4.2 and laser traverse speed: 325 cm/min.

Location	Maximum Gradient, $\frac{\Delta T}{\Delta x}$ (°C/m)	Temperature of Maximum Gradient, T_{mg}, (°C)	Cooling Rate, $\frac{DT}{Dx}$ (°C/s)
Laser Track 1	2.85×10^6	471	7.46×10^0
Laser Track 2	2.40×10^6	454	7.37×10^0
Laser Track 3	1.96×10^6	450	6.44×10^0

a moving heat source (origin). The surface cooling rate $\frac{DT}{Dt}$ in the direction opposite to laser traverse under steady state ($\frac{\partial T}{\partial t} = 0$) can be estimated as per steady state relation given in Equation 4.3

$$\frac{dT}{dt} = \frac{dT}{dx} \times \frac{dx}{dt} \qquad \textbf{(4.3).}$$

However, for the discrete data it can be approximated as follows.

$$\frac{\Delta T}{\Delta t} = \frac{\Delta T}{\Delta x} \times \frac{\Delta x}{\Delta t} = \frac{\Delta T}{\Delta x} u_x \qquad \textbf{(4.4)}$$

where u_x, is the laser traverse velocity. The cooling rates corresponding to maximum temperature gradient $\frac{\Delta T}{\Delta t}$ (from Table 4.2) for steady state were calculated using Equation 4.4 and laser traverse velocity u_x is 325 cm/min. These cooling rates for each track are presented in Table 4.3 and they are order of magnitude lower than the corresponding cooling rates for non-steady state (Table 4.2).

Table 4.3: Surface cooling rate under steady state. Estimated using Equation 4.3 and laser traverse speed: 325 cm/min.

Location	Cooling Rate (°C/s)
Laser Track 1	1.54×10^5
Laser Track 2	1.30×10^5
Laser Track 3	1.06×10^5

The cast alloys are most sensitive to the solidification rate. The Equation 4.2 (non-steady state) is based on a steeper temperature gradient than that corresponding to Equation 4.4 (steady state). Hence, these two relations provide the natural limits (upper and lower respectively) of the surface cooling rate. It is expected that the actual cooling rate responsible for microstructural refinement is some intermediate value. Both values (the upper and the lower limits) being very high ($>10^5$ C/s), the actual cooling rate and, therefore, the solidification rate in laser treatment is also expected to refine microstructure to great extent. The average temperature of maximum gradient, T_{mg}, (Table 4.2) is close to the melting point of the Al-Si-Cu ternary alloys. For non-equilibrium conditions, as in laser treatment, the solidification temperature is suppressed. In ThermoCalc™ calculation using Scheil-Gulliver method, it was found that the solidification temperature was about 470°C. Thus, for simplification, it was assumed that the cooling rate calculated corresponds to solidification rate. Such high cooling rates and solidification rates would refine the microstructure significantly. The laser traverse at a high speed and the instantaneous heat input is confined to a small volume. The hot spot would cause a high temperature gradient with the surrounding substrate, which will result

in a high cooling rate. It is possible that the non-equilibrium condition, thus ensued, would cause evolution of refined and uniform microstructure in the surface layer. Also, it may develop non-equilibrium phases as well as microstructure.

4.1.2 Evolution of Microstructure in Laser Melting

As seen of Figure 4.2 (a), the microstructure of the as-received A319 is cellular dendritic in nature (average dendritic cell size 50 μm). The magnified version of the microstructure of as-received A319 in Figure 4.2 (b) illustrates the presence of coarse dendrites of primary α-Al and eutectic (Al + Si) phase mixture in the inter-dendritic region. As described earlier (page 19) it posses a cellular dendrite microstructure. The hypoeutectic alloy consists of primary aluminum dendrite. The inter-dendritic region is occupied by a eutectic mixture of Al + Si and $CuAl_2$.

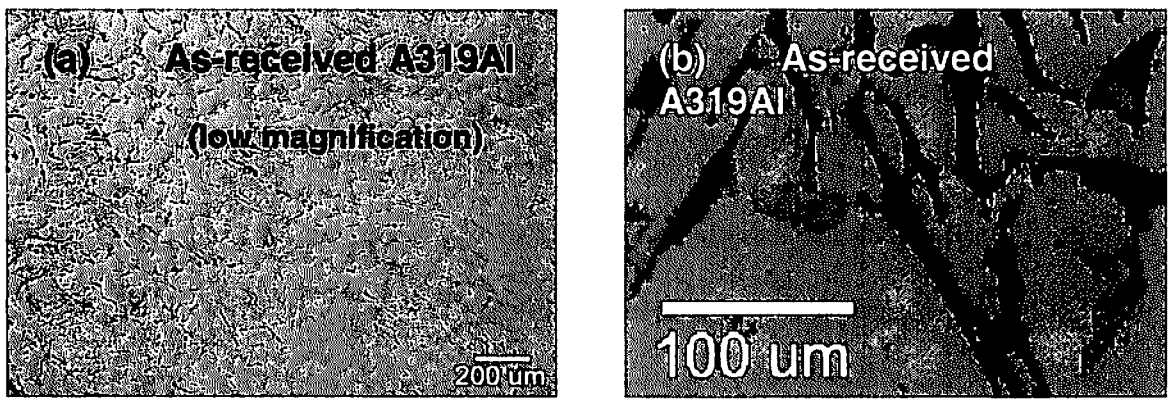


Figure 4.2: Optical micrographs of as-received A319: (a) low magnification view, and (b) high magnification view

A thin layer of the A319 substrate is melted during laser treatment. The convection currents within the melt zone caused mixing of the liquid before rapid solidification. The extent of microstructure refinement can be better presented by a high magnification micrograph of the interface (Figure 4.3). The microstructure within the laser-melted regions was more or less uniform throughout the layer. This layer is metallurgically bonded and seemed to be free from defects such as cracks and pores. The localized heating and steep temperature gradient associated with laser processing, in limiting conditions, can melt selectively the eutectic region (melting point ~ 490°C) without affecting primary aluminum dendrites (melting point 660°C). Therefore, at the interface, the laser-modified region is jig-jag. It can be seen that the prior-inter-dendritic phase mixture has been selectively melted on the interface. This results in rough interface that ensures good bonding and easy load transfer from the laser-melted layer into the substrate. As illustrated in Figure 4.3, the dendrite structure is highly refined within the laser-modified region. Also, the discrete Si particles in Figure 4.2 (b) have disappeared. Instead a refined eutectic mixture occupied the region between Al cells. Additional features of microstructure within the laser modified surface region can be observed in scanning electron micrographs taken at different magnifications (Figure 4.4). As discussed earlier (Section 2.2.1) the microstructure is cellular dendrite. The secondary arms are not well defined/developed. Other constituents like inter-dendritic networks of eutectic mixture, have also been refined and redistributed due to rapid cooling rates intrinsic to the laser-melting zone. The high cooling rate, however, did not change the morphology. By comparing Figure 4.2 (a) and 4.4, one can see that the microstructure is

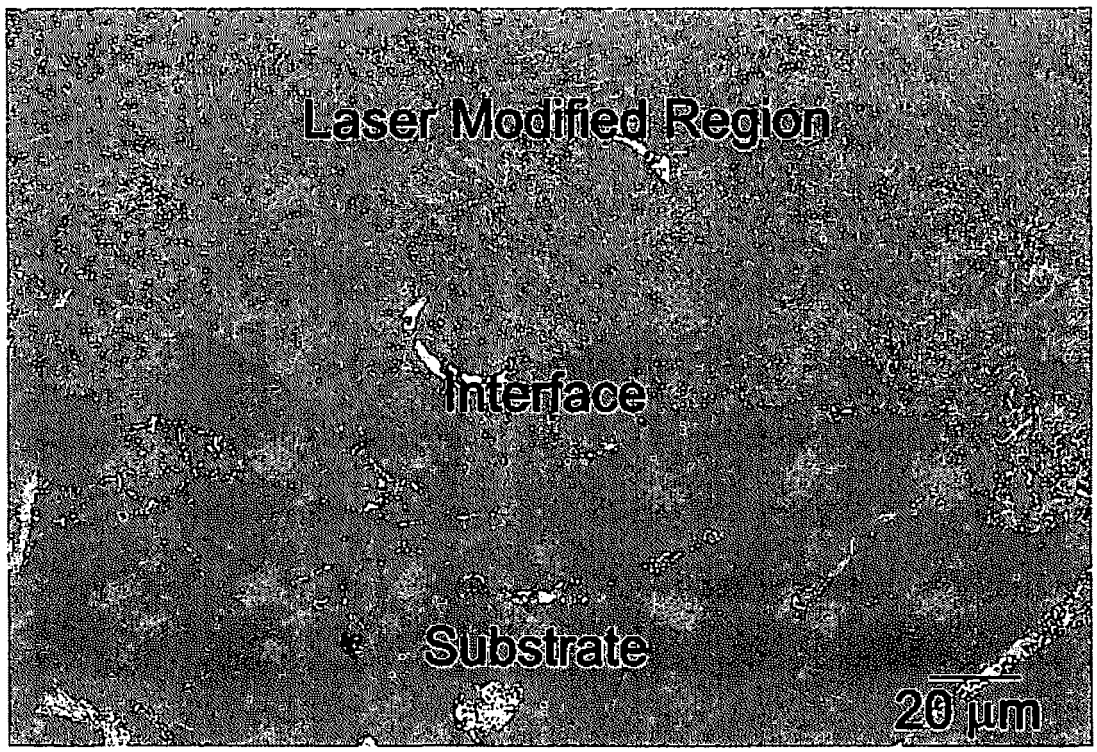


Figure 4.3: SEM of the interface between laser melted layer and the substrate.

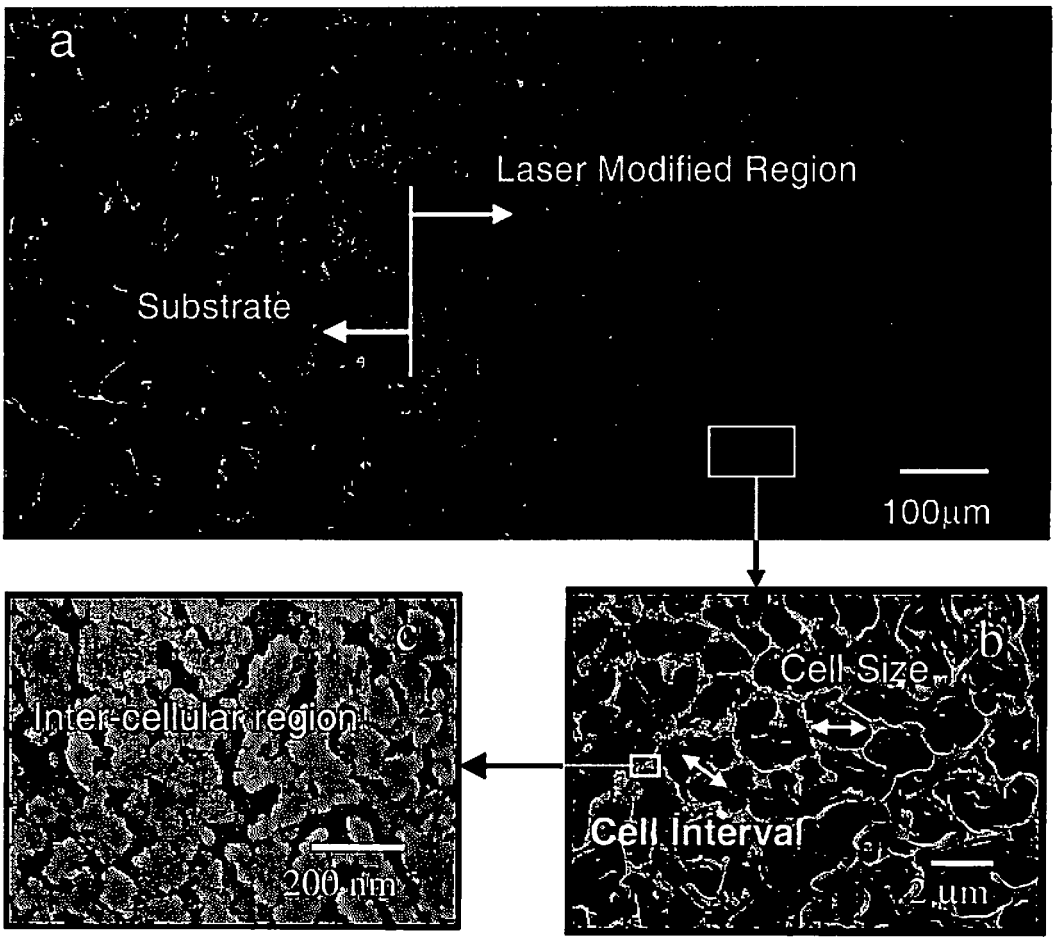


Figure 4.4: SEM of the laser melted zone at different magnifications.

three features, (1) dendritic-arm spacing, (2) dendrite cell interval and (3) dendrite cell size (Figure 4.4). The dendrite cell interval is basically the combination of a cell size and the width of the inter-dendritic phase present (often neglected). However, the cell interval is very hard to measure in the Al-Si system, and cell size is considered appropriate for any quantitative measurements. For a higher cooling rate (i.e., smaller cell size), however, the width of inter-dendritic phase is well defined and the can not be neglected. Hence, cell interval can be measured and is considered more appropriate and consistent with cooling rate. In view of this, the relationship between constant solidification rate and cell size in A356 system is empirically expressed in Equation 4.5 [15].

$$y = 416.713 \times r^{-0.337} \qquad (4.5)$$

where y is the cell size (μm) ; r is the solidification rate (°C/s).

It has also been established that the composition has only limited influence on the relation in Equation 4.5 [15]. Hence, it was considered applicable for A319 alloy. Scanning electron micrographs (Figures 4.4b and c) indicate the cellular structure, not resolved in lower magnification (Figure 4.4a). NIH Image SCION freeware was used to determine the average cell interval. The cell interval was found to be 2.09 ⊤ m (standard deviation ~ 27%). The volume of inter-dendritic phases was 16%, as determined by image analysis. Hence, the average cell size is 0.84 × cell interval, i.e., 1.86 μm. The cell size was calculated using Equation 4.5 and the solidification rate from Tables 4.2 and 4.3. The range of dendrite cell size based on non-steady cooling rates is 2.01-2.11 μm and that from steady state model cooling rate is 7.44-8.44 μm. The steady and non-steady state relations (Equations 4.4 and 4.2 respectively) provide natural limits of surface cooling

rates. Considering that the laser condition and cooling rate are not stable (constant) in the time resolution of $\frac{1}{30}$ second, the fact that dendrites impinge to one another is ignored, and the assumptions in the calculations are ideal conditions that provided an excellent agreement between observed and calculated values.

The primary microstructural features present in a hypoeutectic Al-Si alloy are: Al dendrites, aluminum-silicon eutectic and $CuAl_2$. The combination map of three primary elements, namely, Al, Si and Cu is presented in Figure 4.5. Clearly the cellular region is aluminum (red) whereas the intercellular region is occupied by either Cu (green) or Si (blue) exclusively. Energy dispersive spectroscopy carried out revealed that the green is actually Al+Cu whereas the blue phase is essentially pure silicon.

The Si rich and $CuAl_2$ phases are mostly finely distributed in the intercellular region thereby making this region much stiffer and harder compared to the aluminum cell. However, on the other hand, aluminum cells provide ductility and toughness. By increasing cooling rate alone or in conjunction with an increase in Si, it is possible to reduce cell size, increase the intercellular phase and hence further improve properties. Thus during laser processing a surface can be precisely engineered by optimizing processing parameters (power, traverse speed, etc.) and composition (addition of alloying elements) to have this intercellular phase at nanoscale (Figure 4.4c) level in a matrix of ductile aluminum for formation of a nanocomposite surface layer.

Temperature estimations during laser surface engineering were performed by employing high-speed IR thermographic imaging technique. With some degree of assumption and simplifications, highly resolved temporal and spatial IR thermographic

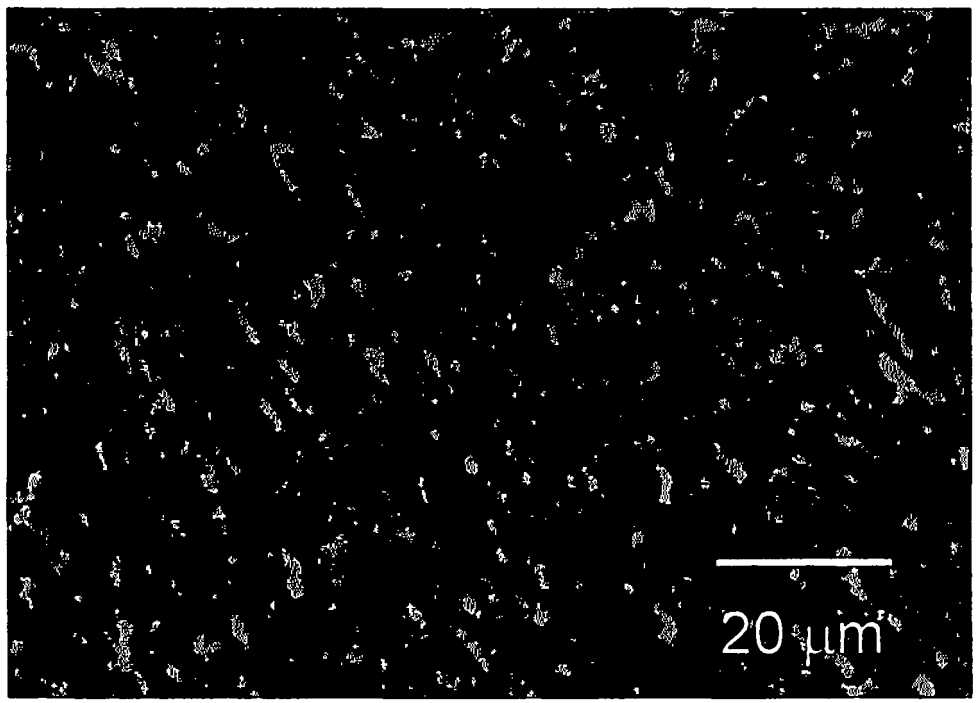


Figure 4.5: Combination elemental map of the laser melted zone. Primary elements are Al (red), Si (blue) and Cu (green), 256 x 256 pixel, pixel size was 150nm.

signals were further utilized in estimation of temperature gradient and cooling rate. Empirical calculations based on non-steady and steady state thermal conditions during laser processing also estimated a range of cell size within the modified surface region that is in close agreement with the experimentally measured average cell size. This, despite of several assumption and simplification, infrared thermography can be used to study rapid processes such as laser surface engineering.

With this kind of refinement in microstructure, a more homogeneous distribution of hard Si and $CuAl_2$ phases and soft and ductile α-Al phase is expected to translate into a stronger, harder and tougher material. In the next section evaluation of mechanical properties of this material is presented.

4.1.3 Improvement in Properties

The mechanical properties of a material generally improve due to microstructural refinement. The strength and hardness increases due to increased number of obstructions for dislocation movement. Additionally, ductility improves because the fracture is delayed as smaller grains can geometrically accommodate more deformation compared to larger grain materials. The cohesion among grains is also improved as a result of refinement. Consequently, the toughness of the material increases.

Similarly, laser melted A319 layer is expected to exhibit improved hardness, strength and ductility. However, as the layer is bonded to the substrate, it is very difficult to determine the mechanical properties of the coating in an isolated manner. As described

in Section 3.4.1, non-conventional techniques such as nanoindentation and scratch test are used to evaluate such a layer [57].

Indentation hardness and elastic modulus were determined from load-displacement curve using the Oliver-Pharr method [49]. Even though this method is meant for monolithic materials, it was assumed that this method holds good since the extent of refinement of the laser modified region was very high. During the depth mode (see Section 3.4.1) indentation process, the instrument senses and records the depths (h) and corresponding contact stiffness (S). The above-mentioned technique uses the load (P), depth (h), area function (A), and the contact stiffness experienced by indentation machine (S) data to determine E and H. The correlation between such physical properties and measured parameters are presented in Equations 3.6 and 3.7 from Ref. [49].

Because the refined microstructure was not resolvable in the optical microscope of the NANOINDENTER instrument, it was not possible to indent individual microstructural constituents. Instead, indentations were made in several tracks at 25μm intervals within the refined layer cross-section from edge towards substrate. This method is based on the intrinsic assumption that the material behaves as a single-phase homogeneous bulk material as far as indentation process is concerned. This assumption holds good for a material with fine microstructural constituents where the sizes of these constituents are small compared to the volume affected by indentation. The hardness and elastic modulus values of the substrate and laser surface-melted sample corresponding to indentation depth of 1000 nm are listed in Table 4.4. It can be seen from Table 4.4 that the variance in hardness value is much less for the modified surface microstructure (<3%) compared to that in the substrate A319 (32%). This behavior can be explained as follows.

Table 4.4: Properties derived from IIT for 1000 nm indentation depth.

Material	Hardness		Elastic Modulus	
	Average (GPa)	Std. Dev. (%)	Average (GPa)	Std. Dev. (%)
Substrate	1.10	32	80.2	7.4
Laser Melted Zone	1.22	2.9	78.2	2.6

As and when the indenter hits a hard/stiff region (Si-rich phase or a region in proximity of a Si particle), a high value of load and contact stiffness is obtained. It increases the average hardness; more so, it causes a larger variation in hardness. In other words, the laser-melted surface region does behave "effectively homogeneous" for indentation of 1000-nm depth, whereas the substrate material does not.

It has been reported that the mechanical properties of a coating changes from surface toward substrate [3]. The composition gradient, inhomogeneous mixing and inadequate coating material supply (when applicable) are responsible for these variations. It was therefore necessary to evaluate mechanical properties to establish any such property gradient is present in this case. However, no particular trend in the hardness or elastic modulus was observed within the laser-refined region while tracing from surface below, indicating the property is more or less uniform throughout this laser refined region. To establish this fact, the property determined from indentations was grouped into two regions, as shown schematically in Figure 4.6. Zone A is the layer 300μm from the surface and zone B is the layer 300μm below zone A. The hardness and elastic modulus values on zone A and zone B corresponding to different depth of indentations (h) are plotted in Figures 4.7 and 4.8 respectively and are summarized in Table 4.5.

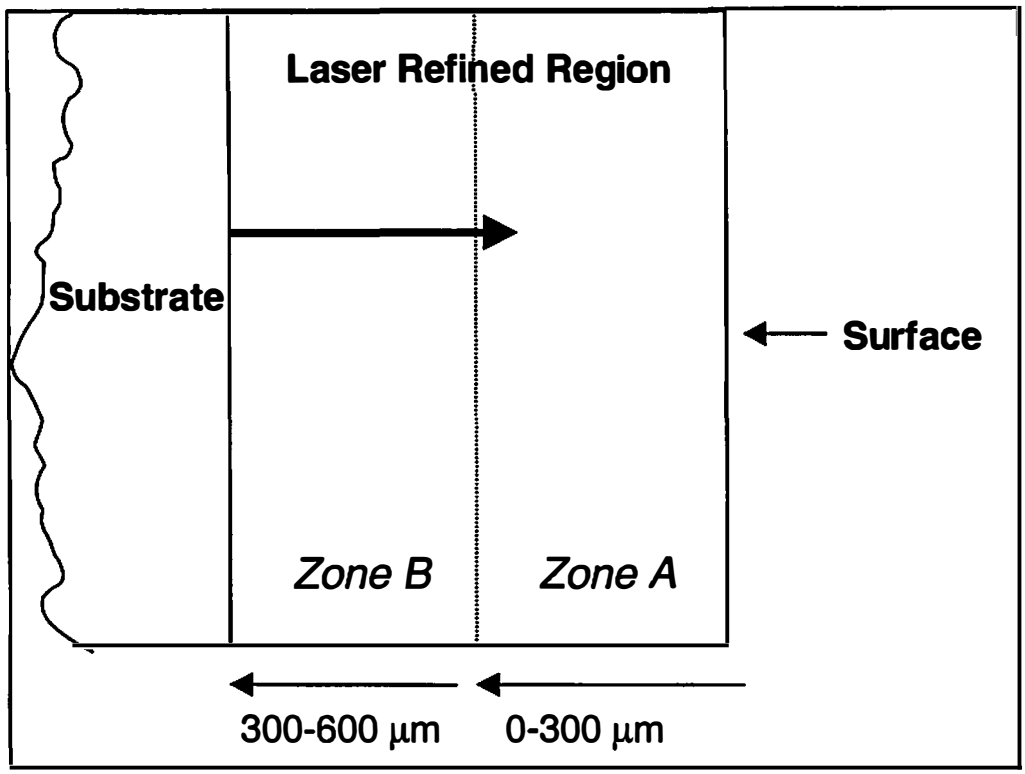


Figure 4.6: Schematic of regions designed for indentation analysis

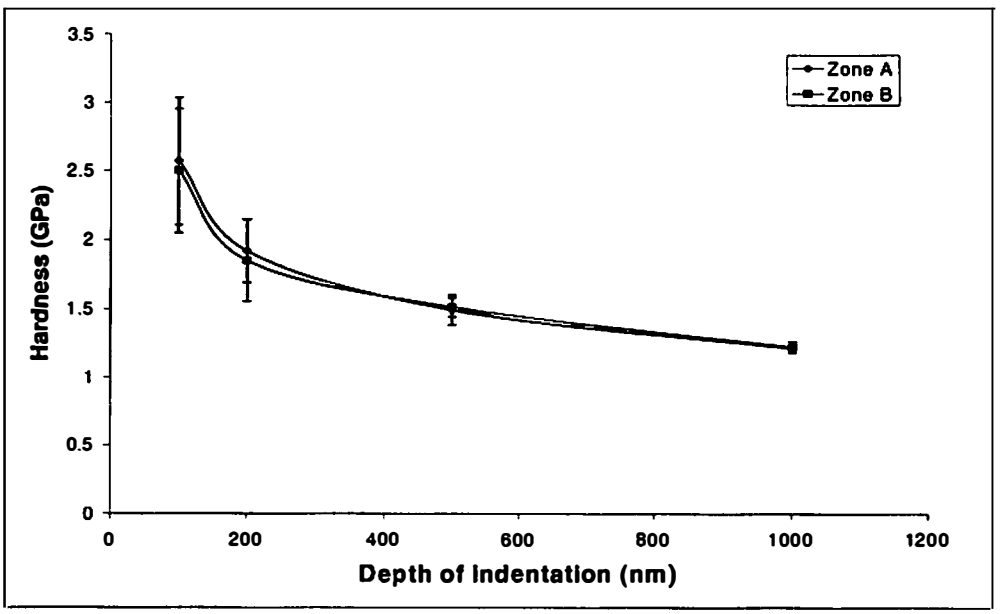


Figure 4.7: IIT data: hardness vs. depth of indentation.

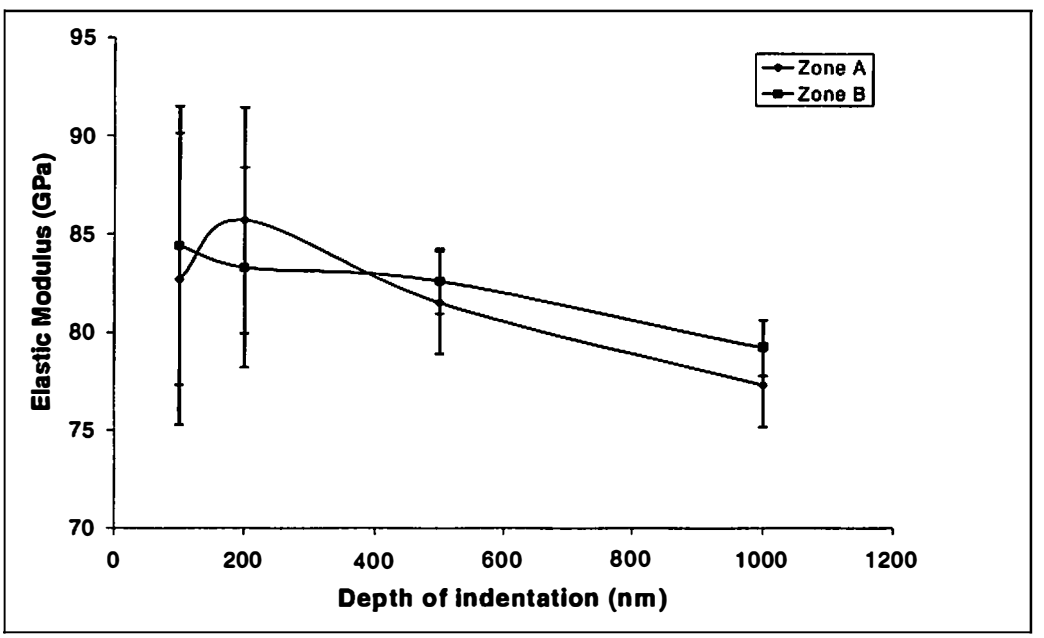


Figure 4.8: IIT data: elastic modulus vs. depth of indentation.

Table 4.5: Properties derived from IIT w.r.t. indentation depth.

Indentation Depth, h, (nm)	E (Std. Dev.) GPa (%)		E (Std. Dev.) GPa (%)	
	Zone A	Zone B	Zone A	Zone B
100	82.7 (9.0)	84.4 (8.4)	2.57 (18)	2.50 (18)
200	85.7 (6.7)	83.3 (6.1)	1.92 (12)	1.85 (16)
500	81.5 (3.2)	82.6 (2.0)	1.49 (7.4)	1.51 (4.6)
1000	77.3 (2.8)	79.2 (1.8)	1.21 (2.5)	1.22 (3.3)

It can be seen that considering the experimental variance and standard deviations, there is little difference in these values for both the zones. Hence, it can be safely concluded that the whole laser refined region is more or less uniform in microstructure as well as in properties. This kind of homogenization achieved in rapidly solidified region was attributed to convective flow of liquid material. The material experiences extreme temperature gradients within the laser melt pool. Because viscosity, surface tension, and density are strong functions of temperature, the temperature gradient drives such a convective flow within the melt-pool [58].

The assumption that the material behaves "effectively homogeneous" for 1000 nm indentation was further investigated. Data were collected at different indentation depths (h). It was found that the H and, to a lesser extent, E decrease with increase in the depth of indentation beyond experimental statistical variation. Observation of higher hardness for smaller depth of indentation is known as indentation size-effect. Several authors have investigated indentation size effects and have proposed various philosophical premises. They include indentation tip effect [49, 50, 59, 60, 61] surface localized work hardening during mechanical polishing of the sample [49, 50, 59, 62] deformation mechanism under

indentation from a dislocation theory point of view [63] and, effect of two-phase heterogeneity on property measurements [64, 65]. The matrix of the parent A319 alloy is plastic, having potential for strain hardening. Because the hardness and elastic modulus of Si (H_{Si} = 12.75 GPa and E_{Si} = 172 GPa) is substantially higher than that of Al (H_{Al} = 0.7 GPa and E_{Al} = 75 GPa), any stochastic indentation of Si particles affect the average value to a dominating extend for lower indentation depth. However, for a larger depth of indentation, the composite (coating) behaves effectively homogeneous. The indenter pushes the hard and stiff Si particles into the soft matrix thereby giving a value (for hardness and elastic modulus) dominated by matrix properties (less stiff). Furthermore, values corresponding to smaller depth of indentation exhibit higher variance, suggesting the material is effectively homogeneous for large depth of indentation, but it is not so for smaller depths (200 nm). The as-received A319 substrate behaves as not "homogeneous" to even 1000 nm indentation depth (Table 4.4).

For further investigation into the issue of variation of reduced elastic modulus [derived from contact stiffness and area function as per Equation 3.7] as function of indentation, depth recorded during loading is plotted in Figure 4.9. As discussed in previous section, each point in the plot represents a single reduced elastic modulus versus depth (Ereduced vs. h) for entire coating (zone A and zone B). The total number of data points are >5000. It can be seen that at high indentation depth (> 500 nm), the reduced elastic modulus is more or less constant, and the scattering is minimal (<10 GPa). However, as the depth of indentation decreases, the scattering in reduced elastic modulus, Ereduced, increases, and within the range of 50-200-nm depth, it substantially increases

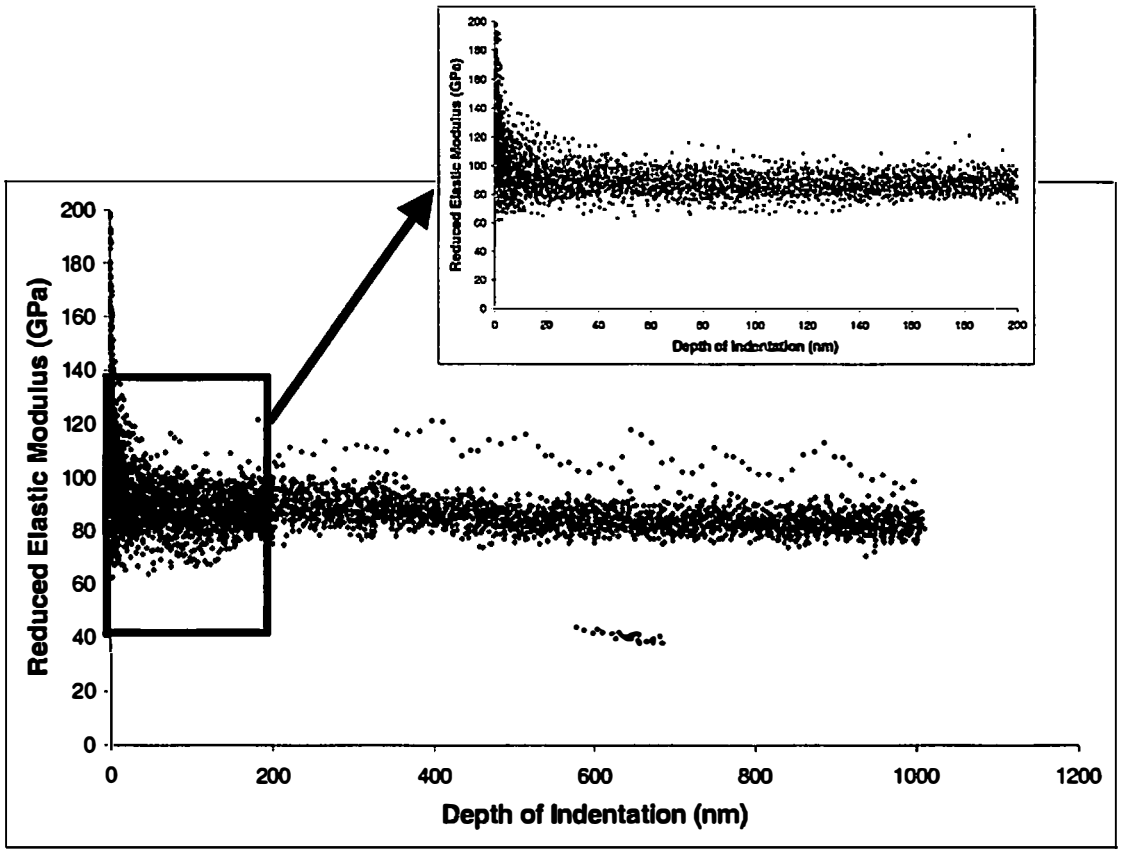


Figure 4.9: Reduced elastic modulus vs. depth of indentation.

(~ 80 GPa). Because the microstructure of laser-melted surface region is heterogeneous in the scale below 0.5 μm and the Al and Si possess extremely different reduced elastic modulus values, the scattering is understandably sourced to heterogeneity in microstructure. At very low depth of indentation (<100 nm), the reduced elastic modulus ($E_{reduced}$) values sharply scatter toward further higher values. Because Si (H_{Si} = 12.75 GPa) and Al (H_{Al} = 0.7 GPa) have distinctly separate properties, it is expected that the reduced elastic modulus-depth data points would gather about two values (one high and one low value). Instead, the reduced elastic modulus value is scattered almost continuously between 70 GPa to 170 GPa and not discrete agglomerations to one high and one low value; it can be considered that the interface between these two phases has a dominating effect on properties.

The ultra-refinement of the microstructure has increased the volume fraction of the interface to an extent that the material is effectively homogeneous up to a very small scale. Also, the stress field of indentation consists of all phases even for indentation depth of 100nm. Another possible contributing factor for indentation-size effect is work hardening of the soft matrix in surface and subsurface regions, which takes place during mechanical polishing of the sample. The matrix of the parent A319 alloy is highly plastic, having great potential for strain hardening. As the effect of work hardening is more prominent at shallower depth, a higher hardness value was observed for smaller depth of indentation. Furthermore, the elastic modulus as a function of depth of indentation depicts a similar trend [Figure 4.8]; however, on a much smaller magnitude. Elastic modulus is a structure insensitive property, hence, the indentation size-effect can be attributed to stochastic indentation of constituents rather than surface work hardening.

Indentations (Berkovich) impressions of up to 1000-nm depth were examined under scanning electron microscope but no cracking around the corners of the indentation impression was observed. Also, the load-displacement responses did not indicate any cracking with the instrumented indentation technique (IIT). This is due to high toughness associated with the composite (uniformly distributed Si particles in Al matrix) nature of the laser surface-remelted sample.

Abrasion and Wear Resistance

Even though, the nanoindentation is a suitable technique to determine the mechanical properties, it has certain limitation in terms of predicting abrasion resistance. The abrasion resistance of a material is determined by several mechanical properties not just static properties such as determined by instrumented indentation technique. Another method of mechanically testing a specimen surface is scratch testing. In fact, scratch tests provide insight to mechanisms of deformation, material removal and evaluate the adhesion of a surface coating to a substrate, making it more akin to tribological properties than a quasi-static indentation hardness test. Also, measured scratch hardness potentially can be used to rank materials for two-body abrasion resistance. Hence, scratch tests were carried out to evaluate such a composite material.

Scratch testing is a method of mechanically testing a surface. In this method, a hard loaded scratching indenter/stylus is used to generate a groove on the surface. Table 4.6 summarizes scratch hardness of pure Al, A319 alloy, and laser-melted sample. The A319 and the laser-treated samples have much higher hardness than pure Al samples due

Table 4.6: Scratch hardness (GPa)

Normal Load (g)	Scratch Hardness (GPa)		
	Pure Al	As-received A319	Laser Melted A319
1000	0.32	1.02	1.19
1500	0.34	1.14	1.23
2000	0.33	1.32	1.23
2500	0.37	1.25	1.24
3000	0.34	1.13	1.44
4000	0.29	0.79	1.43

to presence of reinforcing phases such as Si-rich phases. However, the strong variation of scratch hardness with load observed in A319 is because of the change in deformation mechanism. At much higher load, the scratch hardness drops drastically. This is possibly because of stress and deformation under the scratch surface, strong interaction with hard and discrete Si and Cu-rich phases, and chip off of materials. This was further confirmed from frictional drag force and cross-sectional microscopic examinations. However, the laser melted sample, showed higher scratch hardness for higher load (>3000g). Such variation in remelted A319 can be attributed to change in deformation mode, influence of sub-surface substrate and/or detachment of coating.

Figure 4.10 indicates the cumulative weight loss over 30 mins (equivalent to 8000m sliding distance) for the remelted sample as well as for the base. It is clear that under identical conditions, the weight loss of the laser-refined sample is substantially less than that of the as-received sample. More significantly, the surface of the laser-melted sample was much rougher compared to the as-received ground sample used in wear test.

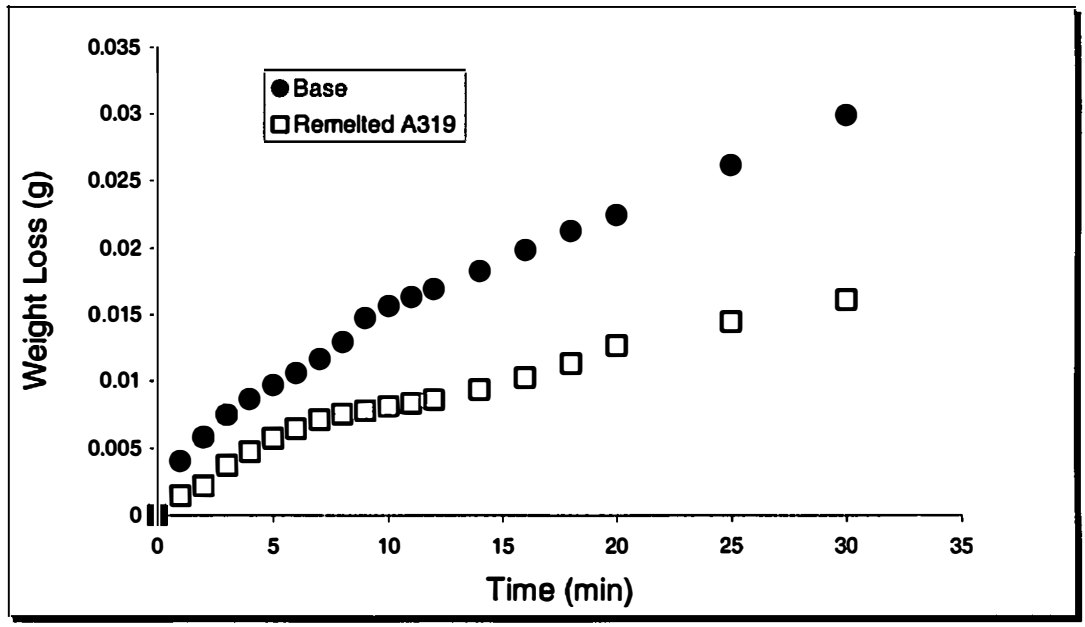


Figure 4.10: Weight loss under dry sliding test of laser-remelted sample. Normal load = 10N, linear speed = 4.4 m/s.

The laser melting of sample creates wavy pattern. The numerous asperities prevent greater contact area, resulting in uneven stress during wear test and greater weight loss. The significant slope change at about 10 minutes of wear is due to settling of these asperities within the wear surface profile.

In this section, it has been shown that a high power laser is capable of melting the surface layer due to matter-photon interaction. The rapid speed, spatially confined power input and self-quenching effect, a high cooling rate ($<10^5$ K/s) is experienced especially in the solidification temperature range. This high cooling rate produces extensively refined microstructure, which manifests in more uniform and better properties. This property improvement was attained without any deliberate chemical composition change in the surface.

In many other applications further improvements are sought. The intrinsic modified microstructure alone may be inadequate to meet mechanical property requirements such as wear resistance. The usual technique is to add a ceramic on the surface layer. As discussed earlier a reactive ceramics is advantageous. Iron oxides are very cheap readily available and proven ceramic. The reactions between oxide and aluminum are also exothermic. In the next Section, iron oxide is studied as a potential coating material. Where relevant, comparisons with laser melting process under identical conditions were made to understand the role of iron oxides.

4.2 Reaction Coating

As hypothesized in Section 2.2.3, aluminum has high affinity for iron oxides. Iron oxides are proven components for combustion synthesis as in thermite welding [38]. Therefore, in this work, synthesis of reaction composite coating is being attempted with iron oxide, i.e., Fe_3O_4 . As shown in Equations 2.5, the Fe_3O_4 has a high heat of reaction (ΔG = 3095 kJ/mol of Al). The crystal structure of Fe_3O_4 is inverse spinel and has high tolerance for defects. The Fe_3O_4 can react with aluminum exothermically. In case of limited reaction, the high tolerance of defects and +3 valence of Al can provide room for reaction-induced wettability. Another oxide, namely FeO, was considered in limited fashion to study the thermite reaction. It has a fcc (Fm3m) crystal structure and has limited reactivity with Al (ΔG = -775.7 kJ/mol of Al) and expected to exhibit lower heat of reaction.

4.2.1 Observation of Exothermic Reaction

The infrared intensity recorded at 30Hz frequency of a point can provide the thermal history. Therefore, intensities of one point on each LSE samples (remelted sample and Fe_3O_4 coating sample), indicated by + in Figure 4.11, is plotted on the right side of the Figure 4.11. The infrared intensity of the point reached a peak as laser beam passes the point. Subsequent peaks seen in the plots are due to laser passing the point or pass nearby in tracks 2 and 3. The peak provides qualitative evidence that the temperature of the laser interaction is higher in case of Fe_3O_4 coating than that of remelted sample. Further, it is possible to determine temperature from infrared intensity using spatially resolved intensity value and intensity-temperature correlation.

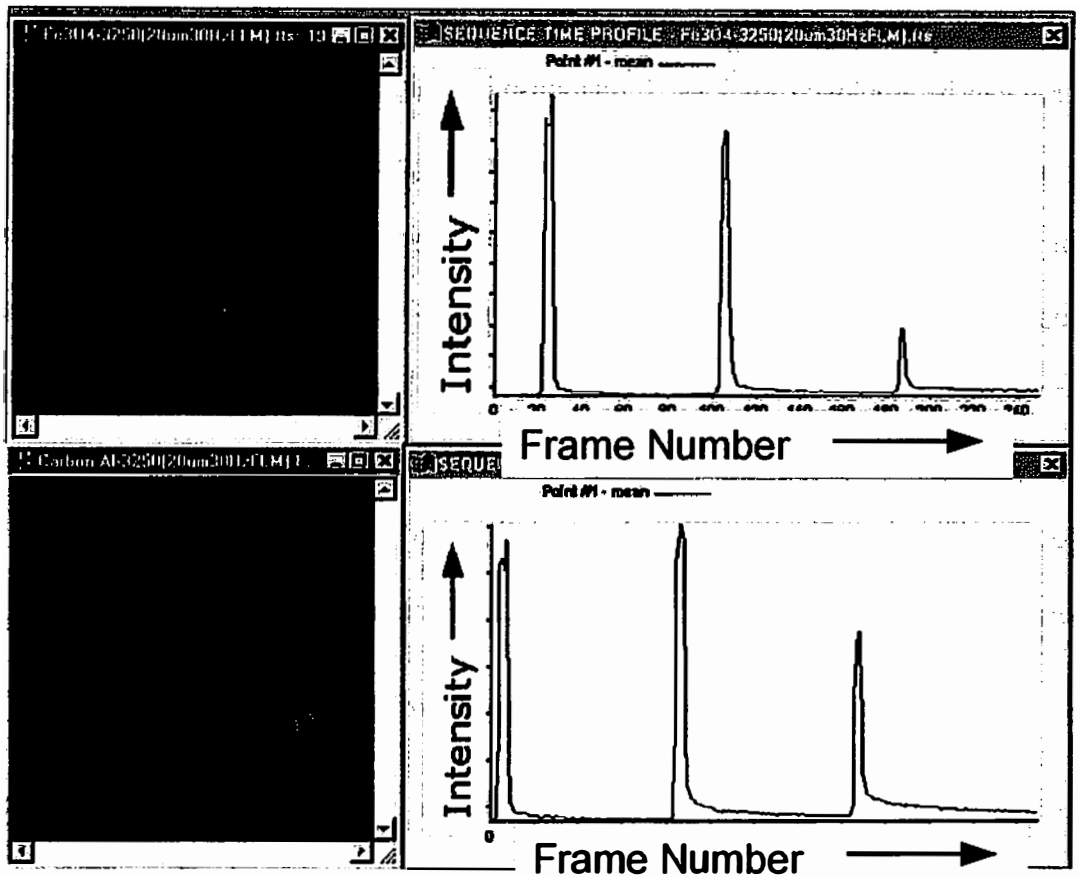


Figure 4.11: Frame captured in IRT during laser processing. The Intensity vs. Frame number profile indicates higher temperature and reaction in case of Fe_3O_4 coating compared to laser melting.

The intensity, I vs. temperature, T data, determined in furnace heating experiments, were analyzed. It was established that for all three samples, the calibration curve can be employed for I vs. T relationship at higher temperature. The emissivity (ε) values of all three samples were very close (Figure 3.3). Intensity, I, is related to temperature, T through empirical fourth order polynomials fitted with the experimental data for the blackbody (furnace) (Equation 3.4) and the samples (Equation 3.5) respectively. As discussed in Section 3.2, the I-T relation was extrapolated for the samples beyond the experimental range to determine temperature from the intensity for the explanations given in page Section 3.2. To find out T of the sample for a corresponding I, similar method was adopted as Section 3.2).

As depicted in Figure 3.2, the intensity of each pixel is recorded every $\frac{1}{30}$ second. By using the empirical calibration relation in Equation 3.5, temperature can be calculated of the entire pixel array or of any particular set of points. The maximum intensity observed in each frame gives the intensity "averaged out" over time duration of $\frac{1}{30}$s and an area of 20μm ×20μm. To determine the maximum temperature during laser treatment several (10) such readings were taken in equal intervals and the average of values (T calculated from I) is presented in Table 4.7. The standard deviation associated with all the measurements presented was below 8% despite of rapid events intrinsic to laser processing and IR thermography (e.g., plume and vapor obstruct the field of view, emissivity changes due to melting and convection, pixel-to-pixel variation, and averaging of intensity over time and space, etc.) suggesting that the experiment is well controlled

Table 4.7: Maximum temperature during laser treatment.

Location	Maximum Temperature, °C (Standard Deviation, %)					
	Fe_3O_4 Coating		FeO Coating		Laser Melting	
Speed, cm/min	325	375	325	375	325	375
Laser Track 1	638 (3.0)	650 (1.8)	597 (0.7)	614 (0.6)	596 (1.3)	596 (2.0)
Laser Track 2	633 (2.2)	626 (2.7)	603 (2.5)	605 (2.1)	578 (1.9)	569 (2.1)
Laser Track 3	643 (2.4)	636 (1.8)	615 (1.8)	612 (1.7)	589 (2.5)	578 (3.2)

and reproducible. The maximum temperature of the FeO coating was found to be lower than the Fe_3O_4 coating but higher than that of remelt sample. The temperature of laser melted sample and iron oxide on A319 can provide information, if there is additional heat due to exothermic reactions [Equations 2.5 and 3.1]. Figure 4.12 shows a typical temperature profile across the laser interaction region in the direction of laser traverse, i.e., X-axis as illustrated in Figure 3.2. The entire temperature profile of the FeO coating was found to be lower than the Fe_3O_4 coating. The precursor thickness, laser absorption and thermal characteristics of both oxides are comparable, but the amount of exotherm associated with the heat of reduction reaction in case of Fe_3O_4 is much higher than that of FeO. Hence, it can be concluded that the higher temperature and bigger area of interaction in case of Fe_3O_4 coating than FeO and remelt samples were due to this exotherm of the thermite reaction.

The temperature profile indicates a peak ahead of laser path. This can be explained as follows. As the laser moves in the X- direction, rapid heating of the

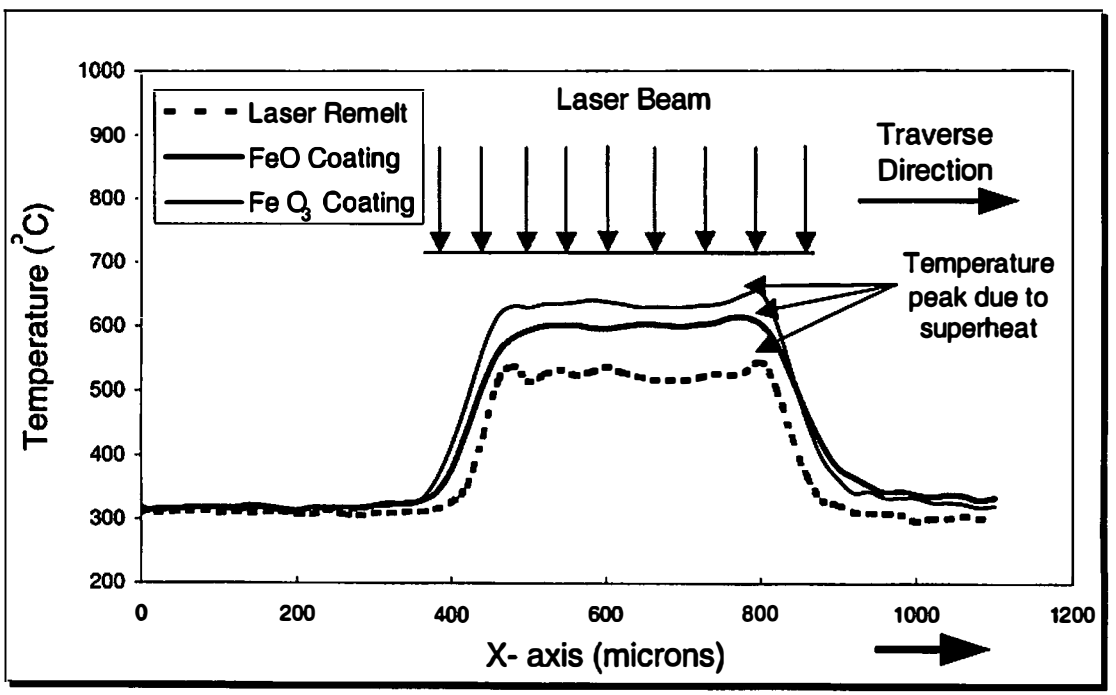


Figure 4.12: Temperature profile in the laser traverse direction across the melt-pool.

substrate takes place. Due to the rapid speed of the process, higher superheating is required before melting can occur. Once it starts melting, the temperature drops a little due to absorption of latent heat of fusion and/or convective heat transfer within the melt-pool. While cooling, however, there is no such forceful directional heat removal as opposed to heating caused by laser traverse. Therefore, the slope of T-X curve ahead of laser traverse (right side of Figure 4.12) is higher than the slope on left side (corresponding to cooling).

Similarly, Figure 4.13 shows a typical temperature profile across the laser interaction region (direction perpendicular to laser traverse, i.e., Y-axis as illustrated in Figure 3.2). Again, the temperature corresponding to the Fe_3O_4 coating was higher than the FeO coating, which in turn was higher than that of the remelting. Also, the volume of hot region under direct laser-material interaction is larger for the Fe_3O_4 coating was higher than the FeO coating, which in turn was higher than remelt sample as determined by width of the T-position crest in Figures 4.12 and 4.13. The temperature gradient or the slope of T-Y curve is significantly lower than that in the T-X curve.

It can be clearly seen from the Table 4.7 that the average of maximum temperature recorded in several (~10) frames (of the same coating and speed), T_m, is highest in case of the Fe_3O_4 coating followed by the FeO coating and the remelting sample for both the laser speeds. Even though the thermal properties of both the oxides are similar and possibly both can undergo a reduction reaction, the Fe_3O_4 coating exhibits higher temperature, possibly due to extra heat supplied by the thermite reaction and greater readiness of Fe_3O_4 to react with Al. The remelted sample exhibited the lowest maximum temperature, T_m. Moreover, FeO may have provided some degree of heat of

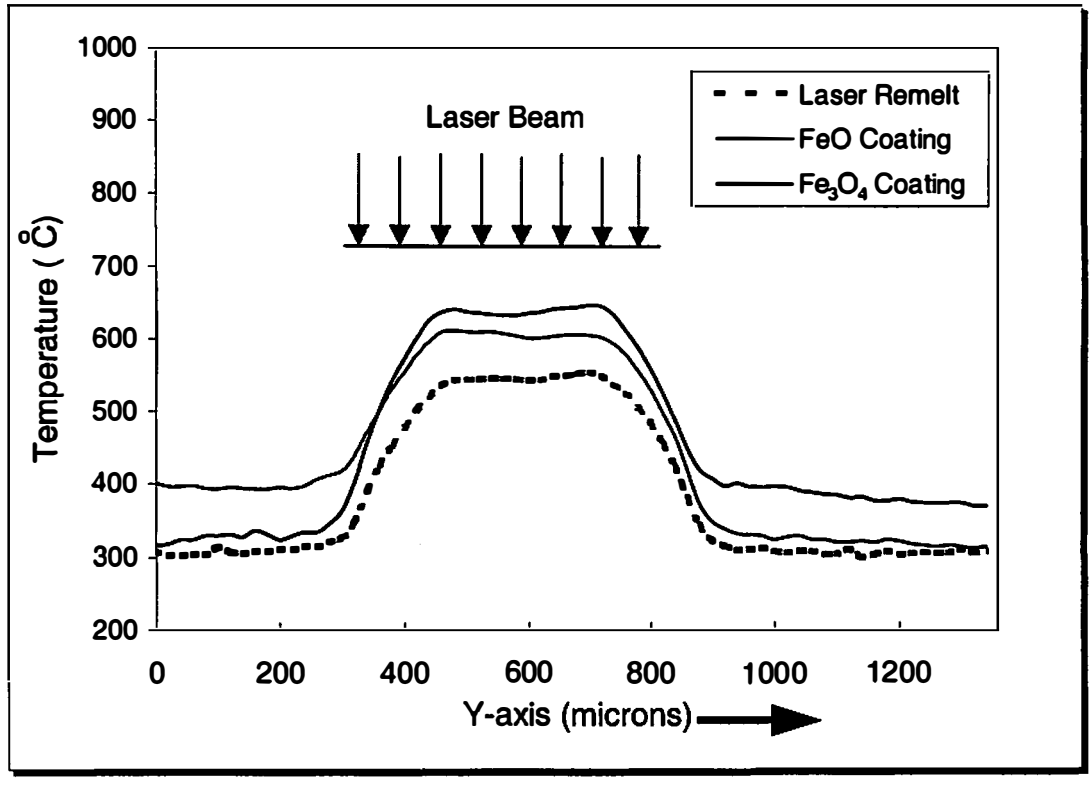


Figure 4.13: Temperature profile perpendicular to the laser traverse direction across the melt-pool.

reaction. The standard deviation <3.0% indicates excellent reproducibility and reliability of the process. It is difficult to see if the average maximum temperature, T_m follows any particular trend with speed. Apparently, the variation in speed of the laser traverse is less significant than the energy input of the laser itself. The concentrated energy input manifests in severe thermal condition, which shadows the effect of laser traverse speed.

The solidification microstructure and the properties are strongly influenced by the cooling rate. This, in turn, is primarily determined by the temperature gradient, $\frac{dT}{dx}$. Hence, it is essential to estimate the temperature gradient, especially during cooling. From the temperature vs. position data for a known laser traverse speed, it is possible to determine the temperature gradient and cooling rate. Since, the temperature profiles in X and Y directions were different [Figures 4.12 and 4.13], these exercises were carried out for both X and Y directions. The temperature-position data is incremental (pixel by pixel) and, therefore, discrete temperature gradients, $\frac{\Delta T}{\Delta x}$ and $\frac{\Delta T}{\Delta y}$ were calculated. The temperature gradient during cooling thus calculated can vary strongly as a function of position. However, the temperature profile is considered very sharp in the boundary of instantaneous laser interaction region [Figures 4.12 and 4.13]. It is, therefore, assumed that only the maximum temperature gradient is of significance in determining the final solidification rate. Moreover, as the solidification front propagate opposite to heat extraction direction and is always associated with latent heat of fusion, the temperature gradient is highest close to the solidification front. The increase in laser traverse speed induces an increase in temperature gradient in X direction.

The consequence of speed increase is ambiguous as far as temperature gradient in Y direction is concerned. Moreover, the speed seems a less important factor as far as the temperature gradient is concerned. It can be seen that the average of maximum gradients, $\frac{\Delta T}{\Delta x}$, recorded from several frames were highest for Fe_3O_4 coating (Table 4.8). However, the gradient in Y-axis, $\frac{\Delta T}{\Delta y}$, is though significantly different from sample to sample, does not follow any obvious trend. Several such frames were analyzed and found to possess minimal variations (<5%) in $\frac{\Delta T}{\Delta x}$. As explained above, the maximum temperature gradient is of primary interest. The temperature corresponding to average maximum temperature gradient, T_{mg} in a frame was calculated for better correlations. The average values are presented in Table 4.9. It can be noted that the temperature corresponding to maximum gradient T_{mg} is different (significantly lower) than the average maximum temperature, T_m, recorded (Table 4.7). This is obvious as the highest temperature corresponds to over-heated liquid within the melt-pool and the maximum gradient occurs on the periphery of the melt-pool where the solidification front is.

Based on the argument presented in Section 4.1.1 for laser surface melted A319, the surface cooling rates for iron oxides coated samples were also determined considering both non-steady and steady states. Cooling rates for non-steady and steady states are presented in Tables 4.10 and 4.11 respectively. In such a moving origin (heat source) problem attain steady state (time independent), meaning the temperature profile around the heat-matter interaction spot remains unchanged. However, it is not known whether steady state or non-steady state is attained in the current scenario.

Table 4.8: Maximum temperature gradients at the periphery of laser melt-pool in the directions parallel and perpendicular to laser traverse.

Maximum Gradient (°C/m)	Location	Fe_3O_4 Coating		FeO Coating		Laser Remelted	
	u_x (cm/min)	325	375	325	375	325	375
$\frac{\Delta T}{\Delta x}$	Track 1	3.4×10^6	3.5×10^6	3.1×10^6	3.1×10^6	3.0×10^6	3.1×10^6
	Track 2	3.0×10^6	3.1×10^6	2.9×10^6	3.0×10^6	2.6×10^6	3.0×10^6
	Track 3	2.9×10^6	3.1×10^6	2.8×10^6	3.1×10^6	2.3×10^6	2.8×10^6
$\frac{\Delta T}{\Delta y}$	Track 1	2.7×10^6	1.9×10^6	2.2×10^6	2.3×10^6	1.9×10^6	2.0×10^6
	Track 2	2.2×10^6	1.9×10^6	2.1×10^6	2.1×10^6	1.9×10^6	1.9×10^6
	Track 3	2.1×10^6	1.9×10^6	2.1×10^6	2.1×10^6	1.9×10^6	2.0×10^6

Table 4.9: Temperature corresponding to maximum gradients, T_{mg}.

Location	Fe_3O_4 Coating		FeO Coating		Laser Remelted	
u_x (cm/min)	325	375	325	375	325	375
Track 1	469	482	461	469	445	439
Track 2	528	492	479	453	457	466
Track 3	512	488	467	470	448	448

Table 4.10: Non-steady state cooling rates.

Axis	Location	Fe_3O_4 Coating		FeO Coating		Laser Remelted	
	u_x (cm/min)	325	375	325	375	325	375
X	Track 1	4.3×10^6	5.2×10^6	4.5×10^6	3.4×10^6	6.8×10^6	5.4×10^6
	Track 2	4.4×10^6	4.2×10^6	2.7×10^6	2.0×10^6	5.6×10^6	4.0×10^6
	Track 3	4.5×10^6	3.9×10^6	2.0×10^6	4.4×10^6	2.3×10^6	5.0×10^6
Y	Track 1	2.5×10^6	1.1×10^6	1.8×10^6	2.6×10^6	1.9×10^6	1.9×10^6
	Track 2	2.7×10^6	1.3×10^6	1.3×10^6	1.7×10^6	1.9×10^6	2.2×10^6
	Track 3	2.2×10^6	1.9×10^6	1.2×10^6	1.8×10^6	1.9×10^6	1.8×10^6

Table 4.11: Steady state cooling rate in the directions opposite to laser traverse.

Location	Fe_3O_4 Coating		FeO Coating		Laser Remelted	
u_x (cm/min)	325	375	325	375	325	375
Track 1	1.9×10^5	2.2×10^5	1.7×10^5	2.0×10^5	1.6×10^5	1.9×10^6
Track 2	1.7×10^5	2.0×10^5	1.6×10^5	1.9×10^5	1.3×10^5	1.8×10^6
Track 3	1.6×10^5	1.9×10^5	1.3×10^5	1.6×10^5	1.1×10^5	1.8×10^6

From the Tables 4.7, 4.8, 4.9 and 4.10, it can be seen that under non-steady state, the average maximum temperature T_m, average temperature of maximum gradient T_{mg}, maximum temperature gradient $\frac{dT}{dx}$ and cooling rate $\frac{DT}{Dt}$ change only very gradually from track 1 to track 3. Also, the corresponding standard deviations for a particular track were within 5%. This is an indication of close to steady state. By its very nature, a steady state problem is simple to solve. Therefore, attempts were made to calculate the cooling rates assuming a steady state heat transfer for a moving heat source (origin). The surface cooling rate $\frac{DT}{Dt}$ in the direction opposite to laser traverse under steady state ($\frac{\partial T}{\partial t} = 0$) can be estimated as per steady state relation given in Equation 4.3. However, for the discrete data in this case, it can be approximated as in Equation 4.4.

The steady state cooling rates corresponding to maximum temperature gradient (from Table 4.8) and laser traverse velocity u_x = 325 or 375 cm/min were calculated using Equation 4.4. The cooling rates for each track are presented in Table 4.11 and they are order of magnitude lower than the corresponding cooling rates for non-steady state

(Table 4.10). In non-steady state, generally the instantaneous temperature gradient is higher compared to steady state and correspondingly it is expected to indicate higher cooling rate. laser-processed samples possess very similar appearance.

The as received A319, remelted sample (for comparison) and iron oxide coatings were investigated in optical microscope for evidence of thermite reaction (Figure 4.14). The oxide particles are not apparent in Figure 4.14 (c) and (d), perhaps due to their readiness to react with aluminum leaving behind little remnant. Equation 4.2 (non-steady state) is based on a steeper temperature gradient than that corresponding to Equation 4.4 (steady state). Hence, these two relations provide the natural limits (upper and lower respectively) of the surface cooling rate. Since the values of both upper and lower limits are very high ($>10^5$ C/s), it is expected that the actual cooling rate responsible for microstructural refinement is some intermediate value.

Figure 4.11 provided qualitative evidence that the Fe_3O_4 coating produces a higher temperature than remelt sample and FeO coating. Further, confirmation of the order of cooling rate by rapidly solidified microstructure serves to underscore validity of the infrared thermography data and the calculations. Therefore, it can be concluded that the Fe_3O_4 coating did produce extra heat of reaction associated with thermite reaction.

The violent nature of the coating can further be corroborated by observation of plasma/plume are-up as seen in Figure 4.15. The plume and vapor tails follow the melt-pool as the laser traverse.

Moreover, high energy high speed processing further increases the reaction rate. Since the frame rate is only 30 Hz and the intensity is averaged over an area of 20 μm × 20 μm, it may not be adequately `time- and space-resolved'. In case of such an extremely

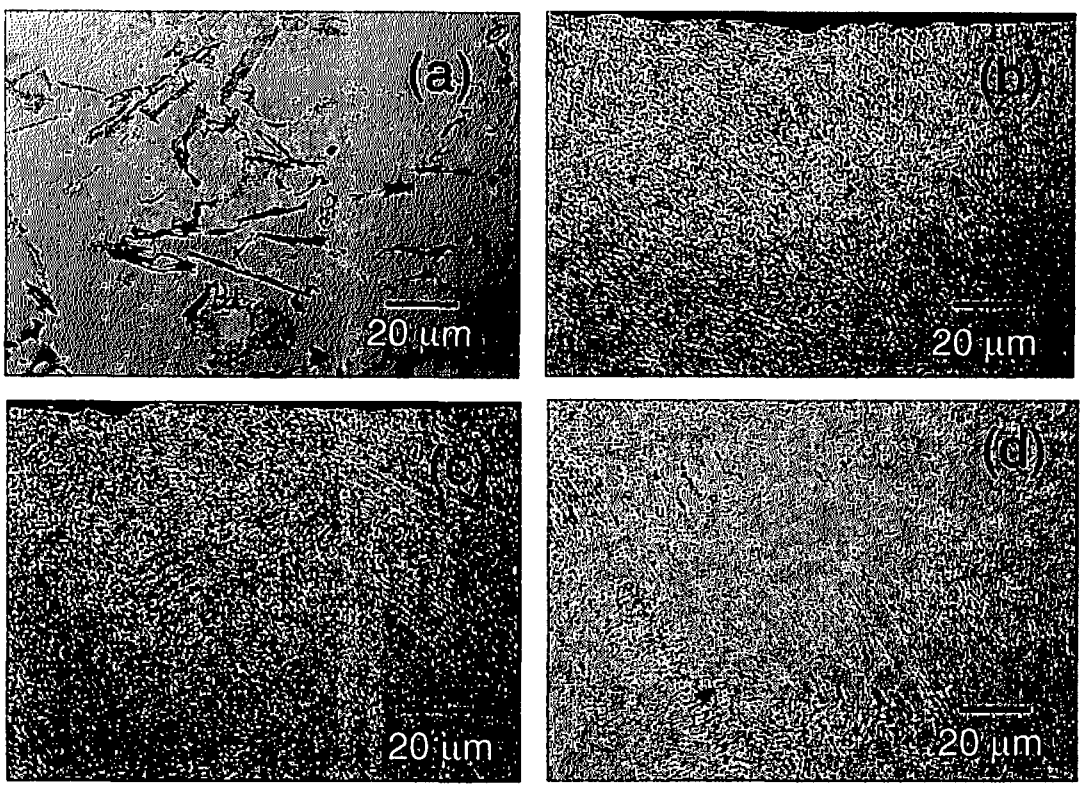


Figure 4.14: Optical micrographs of substrate and laser treated samples: (a) As-received A319 (b) the remelted A319 (c) FeO coating (d) Fe_3O_4 coating.

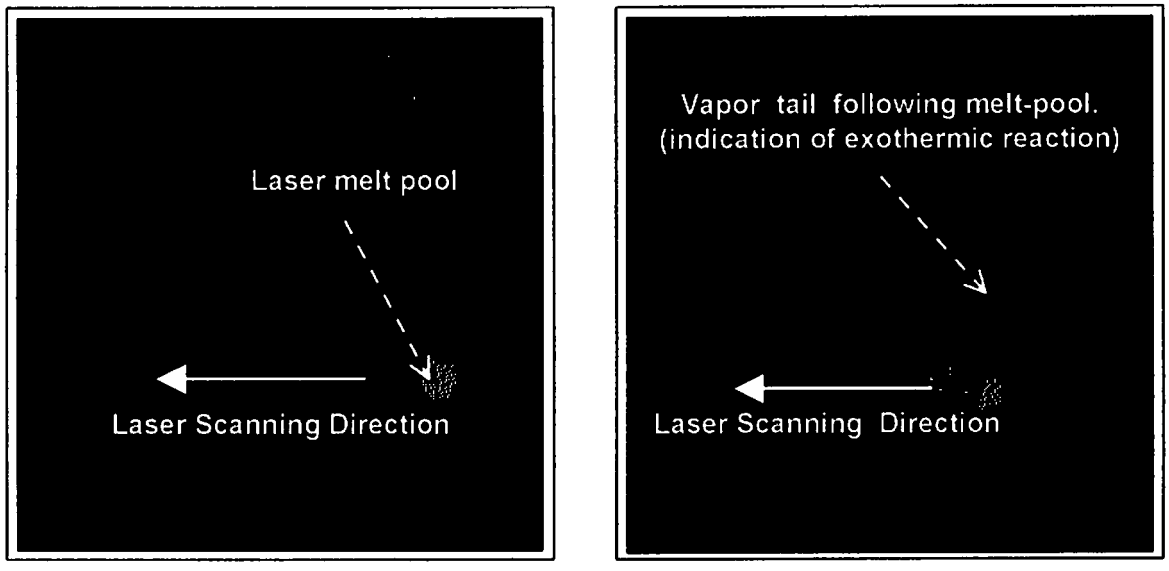


Figure 4.15: Infrared thermographs of the samples under laser processing. IRT of Fe_3O_4 coating (right) indicates reaction. IRT of laser melting is given for comparison (left).

reactive system, part of the radiation is absorbed or scattered by plume generally observed in laser processing. However, an higher temperature should be observed in the case of higher temperature.

4.2.2 Evolution of Microstructure in Reaction Coating

Typical overall microstructural views of Fe_3O_4 coating on A319 are presented in Figure 4.16. It shows the microstructure within the Fe_3O_4/Al composite coating. The coating is free from macro-defects (such as cracks and pores) and consists of fine dendrites. It is composite in nature consisting of Si particles (in the form of an Al-Si eutectic mixture),

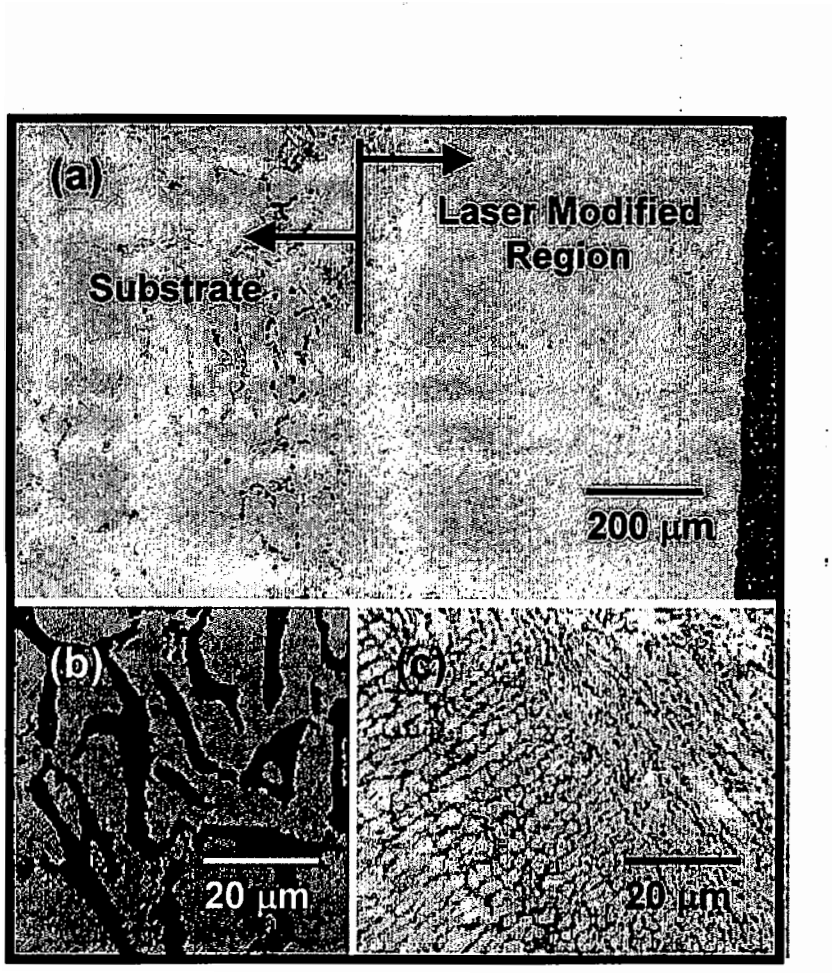


Figure 4.16: Optical micrographs of the Fe_3O_4 coating and the substrate: (a) microstructure of as received A319 substrate and laser modified region A319 and, (c) microstructure of substrate at higher magnification (c) microstructure of laser modified (Fe_3O_4/A319 composite) region at higher magnification

Fe_3O_4 and other reaction products (e.g. FeO, intermetallic compounds like Fe-Al, (Fe,Si)-Al and Al_2O_3) in a matrix of fine α-Al dendrites (2 μm average grain size). A thin layer of the A319 substrate melted and mixed with Fe_3O_4 due to the convection currents within the melt zone. Moreover, as illustrated in Figure 4.16, the dendrite structure is highly refined. For example, from initial grain size > 50 μm, the remelted zone has average grain size ~ 2μm. Also, the discrete Si particles in Figure 4.2 (b) have disappeared. Instead a refined eutectic mixture occupied the region between Al cells. Rapid cooling rates (>10^5 K/s) associated with laser melting causes extensive microstructural refinement [11, 18, 25, 66, 67, 68]. Other constituents, like inter-dendritic networks of eutectic mixture, have also been refined and redistributed due to rapid cooling rates intrinsic to the laser-melted zone. For a given chemical composition, the volume fraction of eutectic mixture in rapidly solidified off-eutectic material (higher cooling rate) is expected to be greater than that of materials solidified under equilibrium conditions because of suppression of eutectic growth temperature [18]. This manifest in a lesser volume fraction of pro-eutectic α-Al dendrite in the rapidly solidified zone as compared to slowly cooled A319.

Figures 4.16 and 4.17 indicate that the Fe_3O_4 coating also has the cellular dendritic structure as in the remelted sample (See Figure 4.4). However, a closer examination of Figure 4.17 reveals the inter-dendritic region is very irregular. Possibly, this is due to the exothermic reaction between iron oxide and aluminum. As hypothesized in Chapter 2 and confirmed by temperature measurement reaction between Fe_3O_4 particles and Al does take place during laser treatment. Aluminum has strong affinity for

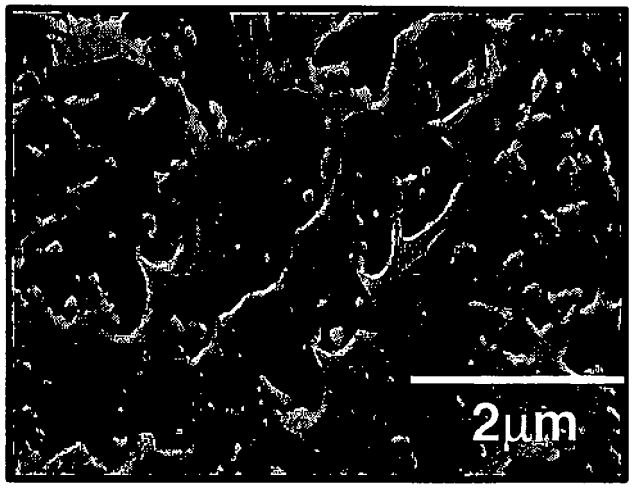


Figure 4.17: SEM of the Fe_3O_4 coating.

oxygen. An Ellingham diagram predicts that the iron oxides (Fe_3O_4) are readily reduced by Al to form Al_2O_3 [36, 69]. Since the oxygen from Fe-oxide has to diffuse through Al or Al has to diffuse into Fe-oxide particles for completion of this reaction, a 'quenched-in' materials system thus can contain an intermediate phase M-O, where M represents Fe and Al. Formation of similar intermediate phase has been reported for Al-Si-O-C system in LSE [70].

X-ray diffractions revealed presence of some un-reacted Fe_3O_4 along with phases such as Al_2O_3, aluminides and other intermetallic compounds as products of several possible reactions. Due to melting, mixing and rapid cooling of A319 during laser interaction, reactions between Fe-oxide particles and the matrix (Al) produced several

Table 4.12: Reactions between Fe and Al [x Fe + (1-x) Al → Fe_xAl_{1-x}].

Resulting Phases	x_{Fe}	ΔG (J/mole at 1173K)	a_{Al} (1173K)
θ - $FeAl_3$	0.24	-23127	0.712
θ - $FeAl_3$.	0.26	-24152	0.145
η - Fe_2Al_5	0.296	-24887	0.145
η - Fe_2Al_5	0.312	-25197	0.133
ζ - Fe_xAl_{1-x}	0.336	-25623	0.133
ζ - Fe_xAl_{1-x}	0.35	-25748	0.072
β - Fe_xAl_{1-x}	0.49	-25819	0.072
β - Fe_xAl_{1-x}	0.5	-25816	0.066
α-Fe or β - Fe_xAl_{1-x}	0.6	-24700	0.022
α-Fe or β - Fe_xAl_{1-x}	0.7	-21706	0.006
α-Fe or β - Fe_xAl_{1-x}	0.8	-16787	0.001
α-Fe or β - Fe_xAl_{1-x}	0.9	-9764	0.000

phases. Fe-oxide can be reduced by Al via possible intermediate reaction, $3Fe_3O_4 + 8Al = 9Fe + 4Al_2O_3$ to produce Fe (as in the thermite welding). Further, as the Fe mixes with molten Al and the free energy values of several possible reactions between Fe and Al are negative, Fe-aluminides can form as per reactions listed in Table 4.12 [71]. As discussed previously, Auger microanalysis is an excellent tool to study this system. Auger electron spectroscopy was used to analyze the chemical composition of the reacted material following laser processing. A high magnification secondary electron image of the coating is presented in Figure 4.18 and shows a reaction product formed between Fe_3O_4 and Al, possibly an intermediate phase, embedded in an Al matrix. In a conventional thermite welding process the reaction is allowed to proceed until the Fe-oxide is consumed, ensuring a high yield of liquid Fe [38]. In the present case, however, rapid cooling

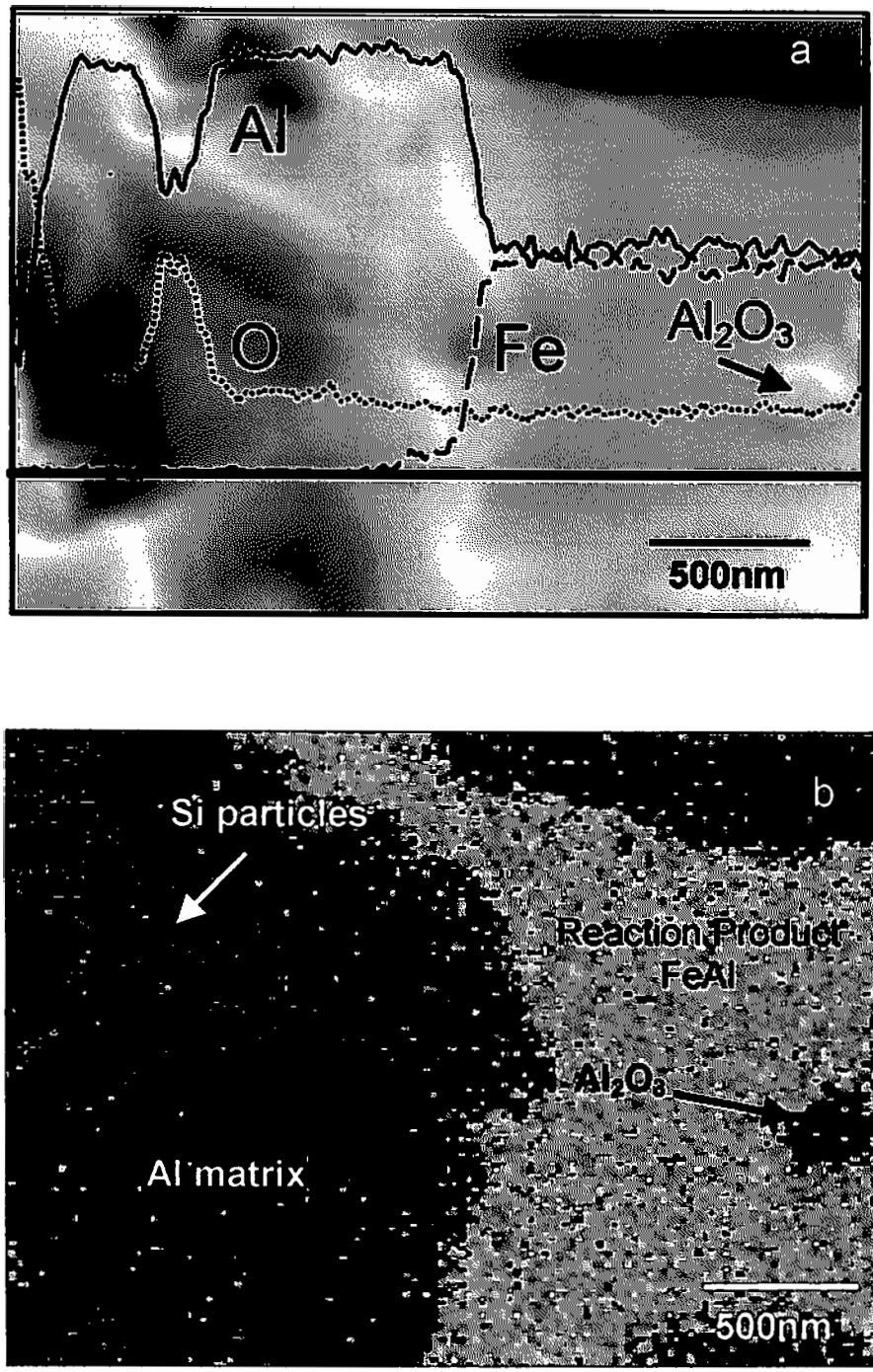


Figure 4.18: Auger micrographs of the reaction coating: (a) Line-scan (b) Combination elemental map

quenched the reaction, resulting in a composite material comprised of partially reacted Fe_3O_4 (with Al) in a Al-matrix. The solid, thick-dashed and thin-dashed curves shown in Figure 4.18 represent normalized concentrations of Al, Fe and O, respectively, along the straight line shown in the Figure. The concentrations of Fe and Al are proportional on right side part of the image suggesting that this may be an aluminide phase. The reaction product Fe-Al and the Al-rich matrix showed a gradual change in Fe and Al concentrations across the interface between them. The thin dashed line shows that oxygen was detected in a near constant amount along the entire analysis line. This indicates that the reaction between Al and Fe_3O_4 (to form Al_2O_3) was not completed. Even though the solubility of oxygen in aluminum is low (it prefers to combine with aluminum), the solubility may be extended due to non-equilibrium condition. Moreover, since Auger microanalysis detects only a few atomic layers, the oxygen can diffuse to surface or be adsorbed on surface due to high activity of pristine surface. This is further supported by observation of the right and left side of the image (corresponding to green and red portion in microanalysis combination map). The aluminide (Fe-rich) side shows a lower average oxygen level compared to the aluminum side. The activity of aluminum is substantially lowered in aluminide compared to that in aluminum (Table 4.12). For example, aluminum activity in aluminides containing 26% Fe (74% Al) is less than 0.15. A lowered aluminum potential reduces the driving force for oxygen to diffuse, hence, shows lower oxygen level. The sharp variation in Al and O concentration on the left side is when the line scan passes through Si-O-rich phases (a Si line scan was not obtained, but post-line scan analysis showed the dark regions are primarily Si). Analysis of the round

particle seen on right side of Figure 4.18 showed it to be Al_2O_3. Modification in microstructure is expected to enhance mechanical properties like toughness and hardness.

The reaction kinetics between oxides and aluminum is primarily determined by oxygen transport and combination. Therefore, it is essential to study oxygen in the coating. Under non-equilibrium condition oxygen can either go to solution or can combine with Al (cations) to form Al_2O_3 depending on diffusion in available time before quenching (cooling) takes place. Similarly, the Fe-oxides, when reduced, would form Fe. Iron can further combine with Al to form Fe-aluminides or can go into a solid solution with α-Al. The possibility of several reactions and combination thereof make it difficult to determine the predominant mechanism. It is, however, expected that intermediate step(s) would be observed in which reactions are only partially complete giving information about the reactions involved. Since, such fine uniformly distributed reaction products are grown in-situ, a novel, non-equilibrium and tough material system can be thus synthesized on the surface.

A closer look at the super-imposed line scan (normalized distribution of major elements) plotted across the line in Figure 4.18 (a) indicated constant proportionality between Fe and Al concentration. Also, Figure 4.18 (b), which is a combination of elemental map (Fe: green, O: blue and Al: red), shows that the particle in fact is a Fe-rich phase (combination of Fe (green) and Al (red) gives hue, a color different than pure green representing Fe). This, in conjunction with Auger elemental microanalysis data, ascertained that the phase is stoichiometric compound of Fe-Al as a result of the final reaction between Al and Fe. The dark region in Figure 4.18 (b) was found to be primarily Si as determined by post line-scan analysis. Since, Fe has large negative free energy of

reactions in solid state ($\Delta G_{reaction}$ at 1173K = 9700 - 25800 J/mol) (Table 4.12, [71]) it can react with Al to form intermetallic compounds (aluminide). Formation of various aluminide phases at 900°C and 1000°C in Fe-Al-O ternary system has been reported. Under high cooling rate, non-equilibrium conditions, formation of various aluminides in Fe-Al-O system has been reported particularly for low oxygen partial pressure [72]. In addition, the composition across the interface between such aluminide particle and the Al matrix changes gradually. Often the interfacial region contained various stoichiometric and non-stoichiometric compositions of aluminides. Low oxygen partial pressure (activity of oxygen) promotes formation of stoichiometric compound. In the present case, since, combination with Al results in depletion of O, formation of aluminide is possible. Moreover, such an in-situ synthesis of uniformly distributed fine aluminide particles having chemical bonding (via formation of interfacial aluminides) with the matrix are expected to produce the composite coating with superior mechanical properties compared to the substrate Al-alloy [73]. The exact composition of the intermetallic compound (within the aluminide particle and interfacial region) is dependent on the activity of the participating constituents. Typically FeAl and Fe_2Al_3 are formed in the interface region between aluminide particle and Al matrix. The ratio of Fe and Al gradually decreased from aluminide particle toward Al-matrix to form FeAl, Fe_3Al_4 and $FeAl_3$ sequentially. Since, Fe-aluminides exist over a wide range of composition [72, 74], such gradual change in composition and formation of various compounds is possible. In-situ formation of such extremely fine (<1 μm) zones of intermetallic phases within the interface region is expected to provide coherency and strong bonding between the particle and the matrix. Many intermetallic particles are observed to contain Si in the range of 10-20 at%. This

could be due to formation of ternary intermetallic compounds (among Fe, Al and Si) rather than binary ones (between Fe and Al). Ternary aluminides have been observed in many systems such as Zr-Al-Si system [75]. These regions are primarily eutectic mixture and the reactions start before any other sites because of the lowest melting point in the system. When Fe3O4 reacts with liquid Al in laser melt-pool as predicted by Ellingham diagram, Al readily reduces the iron oxide to Fe and Al_2O_3. Since the laser treatment is a rapid non-equilibrium phenomenon even though such reduction reaction begins, it is unlikely to be completed. Whereas in some cases, even if Al_2O_3 nucleates, its further growth is inhibited because of extremely rapid cooling associated with the laser processing. Such difficulties in the growth of Al_2O_3 are also observed in Al-deoxidation of steel [72]. It was also observed that often Al_2O_3 and Fe-rich phases were present in the close vicinity of each other (blue particle in Figure 4.18 is Al2O3). This observation suggests that the Al_2O_3 and aluminide particles were formed due to the same or associated reaction(s).

The reaction products and microstructure refinement improve fracture characteristics of the coating. Also, the reaction is *in vacuuo* fracture inside the scanning Auger microprobe chamber and provides a unique opportunity for studying the reaction products and mechanism. The fractograph in Figure 4.19, shows a secondary electron image surface fractured *in vacuuo* that consists of laser modified region and the substrate. Examination of fracture surfaces reveals information about the relative ductility of the material. Figure 4.19 shows one low magnification fractograph (fractured inside the SAM vacuum chamber) consisting of both the coating and the substrate. Fracture across the coating is dimpled in appearance and is a characteristic of a tough and ductile material,

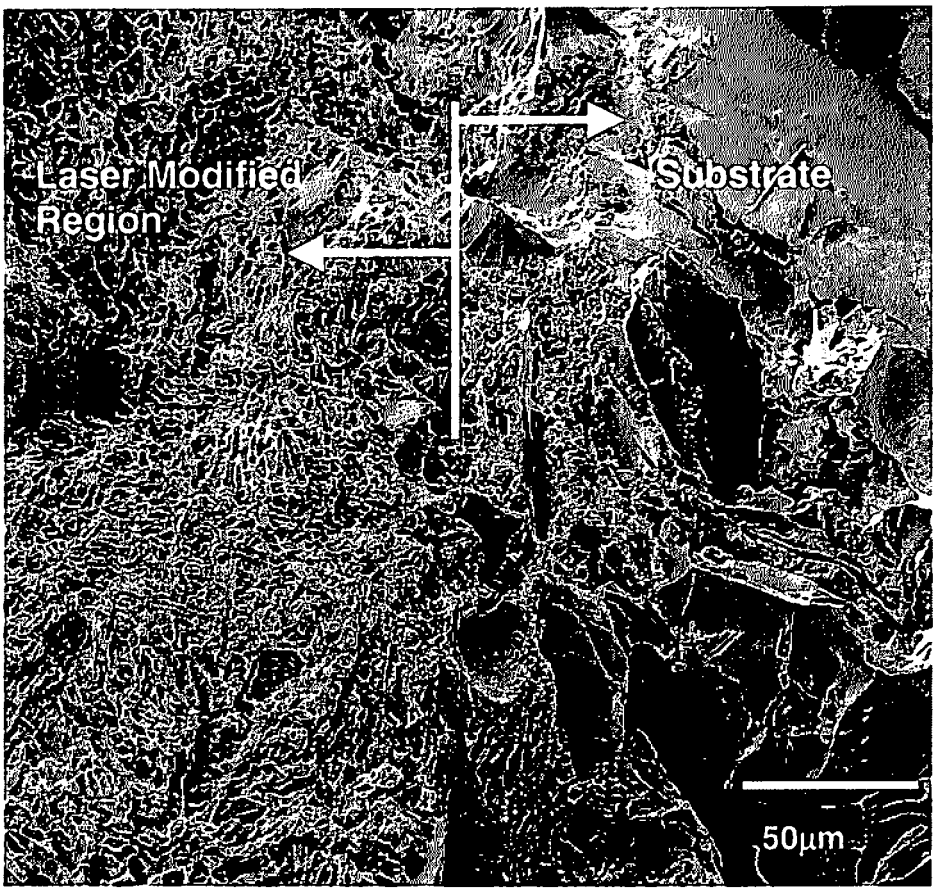


Figure 4.19: Fracture surface of the coating and substrate.

whereas that of the substrate is faceted indicating the brittle nature. Drastic change in fracture response is due to the extensive microstructure refinement (Figure 4.16) during laser processing that is also expected to improve other mechanical properties of the coating.

Figure 4.20 represents a typical Fe-oxide particle embedded in the matrix. The chemical analysis confirmed that the particle is a Fe_3O_4 stoichiometric compound. The crack has propagated across the particle and it is not dislodged from the matrix. It evident that the fracture has propagated across these oxide particles rather than interface between the particle and the matrix. This indicates a strong bonding between the matrix and the particle. It is one of the most desirable features of composite materials. This is possible if the interface between the matrix and the particle is at least as tough as the matrix and/or the particle. The interface between the oxide particle and Al matrix has varied amounts of Al, Fe, Si and O suggesting that an incomplete reaction has been quenched in. This interface was found to contain both stoichiometric (Fe-Al intermetallics) and non-stoichiometric (alloy) compositions. Analysis of some iron oxide particles revealed the presence of small amounts of Al (up to 10 at.%). This indicates that no reaction between the particle and the matrix has taken place. However, Al might have diffused into Fe3O4 to form a solid solution. In fact, $FeAl_2O_4$ (hercynite) forms as Al goes into solid solution with Fe_3O_4, wherein x fraction Al goes into solution substituting x fraction Fe atoms to form $Fe_{3-x}Al_xO_4$. As x approaches 2, the $FeAl_2O_4$ phase emerges under certain conditions (such as temperature range of 860°C-1400°C). However, under reducing condition and higher temperature aluminothermic reaction may result into different reaction products. The non-equilibrium conditions violent and dynamic laser interaction events are all

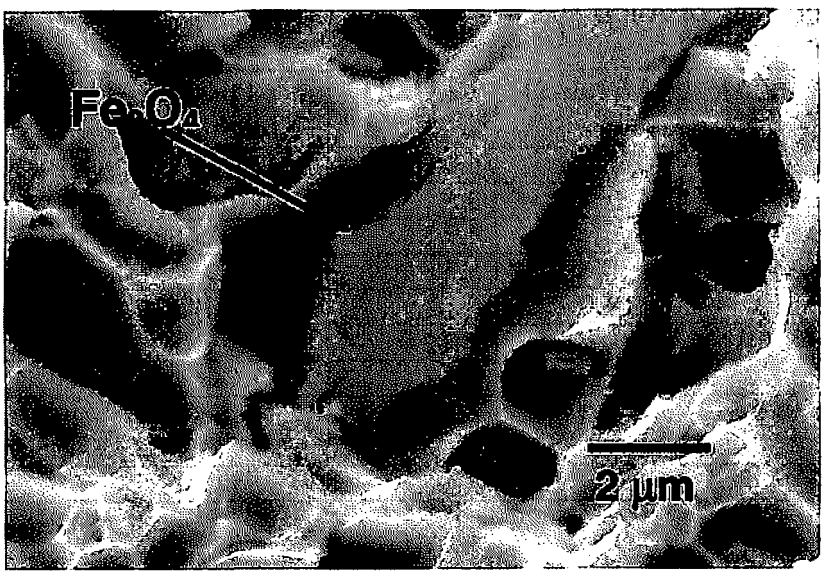


Figure 4.20: Fracture of an oxide particle embedded in the matrix.

conducive to form this phase, but it is difficult to get an understanding of the mechanism.

Table 4.13 and the schematic in Figure 4.21 summarize Auger microprobe analysis of the phase transition in laser-assisted synthesis of Fe_3O_4/Al composite coating. The unreacted and fragmented Fe-oxide particles were seen (in the fractured samples). Various reaction products including stoichiometric and non-stoichiometric phases were observed in discrete and isolated manner as particles as well as within the interface region between these particles and the Al-alloy matrix. The Auger spectroscopy data taken on these phases was further reduced to determine the stoichiometry by taking proportion of major elements present in various combinations for the most likely phases. In a Fe-oxide particle such as presented in Figure 4.21, the Fe to O atomic ratio varied between 1.1-1.3

Table 4.13: Summary of Auger spectroscopy data. (Metals represents Fe, Al and Si).

Location	Fe:Al	Metals:O	2Al:3O	Possible Stoichiometry	Remark
Particle 1	0.9-1.1	High	6.0-High	FeAl	Possibly stoichiometry is gradually changing
Particle 2	0.75	High	3.6	FeAl (0.75Fe-Al)	
Interface 1	0.66	High	4.9	FeAl (0.66Fe-Al)	
Interface 2	0.34-0.29	High	5.7	$FeAl_3$	
Particle 3	0.41	0.9-1.0	0.58	(Fe,Si,Al)O	Intermediate
Particle 4	0.8-1.0	3-4	1.0-2.0	~	Intermediate
Particle 5	<0.2	>0.8	1-1.1	Al_2O_3	
Particle 6	>3	1.1-1.3	<0.1	Fe_3O_4, FeO	Unreacted, high defect density
Matrix	0-0.1	<0.05	3-6	~	Alloy

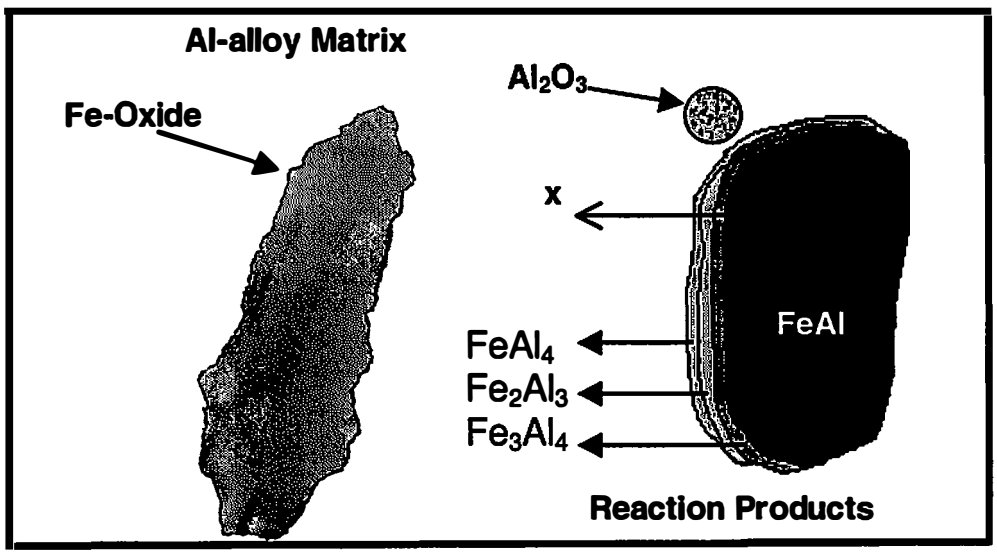


Figure 4.21: Schematic of possible phases; and their shape and configuration. Since the reaction product is formed as Fe + x Al ➔ $FeAl_x$, (x is the ratio of Al to Fe), the value of x increases from the particles towards the matrix.

(Table 4.13). Both FeO and Fe_3O_4 have high tolerance for defects and exist in a range of stoichiometry. While Fe_3O_4 has in some cases remained unreacted, FeO can result from partial reduction of Fe_3O_4. In some particles, Al was present as high as 10-at% (Table 4.13) suggesting Al has diffused into Fe-oxide particle but quenched-in before reaction could take place. Within another particle like feature presented in Figure 4.21 (right side) the ratio between Fe to Al is 0.9-1.1 and it decreases gradually across the interface region between the particle and Al-alloy matrix. Analysis at several points within the interface region suggests that the composition ranges from stoichiometric to non-stoichiometric compounds. It was observed that trace amount of O (in most cases < 3 at% or metal to oxygen ratio > 30; referred in Table 4.13 as 'high') is present in the Al matrix, perhaps in dissolved or adsorbed form. Since, formation of aluminides suggests that the activity of O is very small (less than equivalent partial pressure of O_2 of 1.2×10^{-32} bar). O is most likely present in combined form. Also, the oxygen level in a typical Fe-aluminide particle is even lesser compared to that in the adjacent matrix line scan corresponding to O in Figure 4.18. This could be because the solubility of O in aluminide is less compared to Al, since the activity of Al is less in compound form (as in aluminides) than in elemental form (See Table 4.12).

Transmission electron microscopy observations and analysis were made within the laser-refined layer and "composite coating". A bright field TEM image of the composite coating is presented in Figure 4.22. The iron oxide particle sits in side the cell preferentially near silicon. This is again because it was the last region to solidify (after the primary Al-dendrites have formed). The inter-cellular (silicon rich) phase has fluctuation of contrast. Closer diffraction pattern indicated that it could be due to the

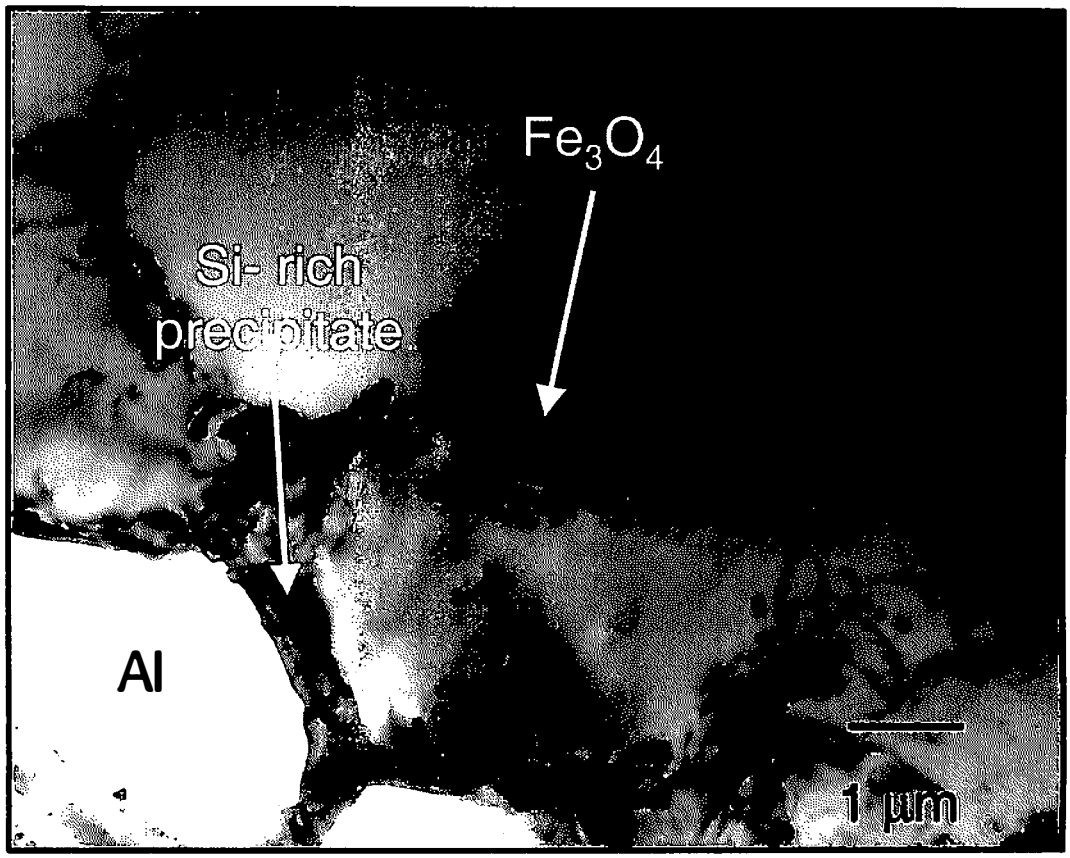


Figure 4.22: TEM indicating iron oxide particles within Al cell.

orientation effect. The solidification of the eutectic phase mixture results from remnant of liquid within α-Al dendrites and so Si do not have any particular preferred orientation within the inter-dendritic region.

A bright field TEM image indicates reaction between iron oxide and aluminum matrix along the interface (Figure 4.23). The diffraction pattern and energy dispersive spectroscopy confirms that the long precipitate along the interface is iron-aluminide close to the composition and crystal structure of FeAl. As seen by Auger microanalysis data, presented in this section, it can be concluded that the Fe-Al phase aluminide has precipitated along the interface as a result of the reaction between Fe-oxide and aluminum.

The exothermic reactions corresponding to above mentioned various products also have supplementary effect on grain refinement of the coating. Grain multiplication, primarily caused by dendrite remelting, is another factor responsible for grain refinement. If an arm from a dendrite is separated and carried away into slightly super-cooled liquid, a new crystal is formed without an added nucleation event. Convection provides a mechanism, not just carrying away the dendrite arms and other oxide particle, but also for dissipating superheat in the liquid so that the transported arm can grow [76]. Also turbulent convection has the added effect of bringing heat pulses to the interface. Laser melting by its very characteristics produces forced convection in liquid [58]. The probability of dendrite remelting increases with increase in convection and with the latent heat of fusion as the higher heat associated with solidification would reduce under-cooling of the liquid. Since, in laser treatment Fe_0O_4 particle or Fe react with Al in a region of limited volume within the liquid pool, locally the under-cooling can be reduced

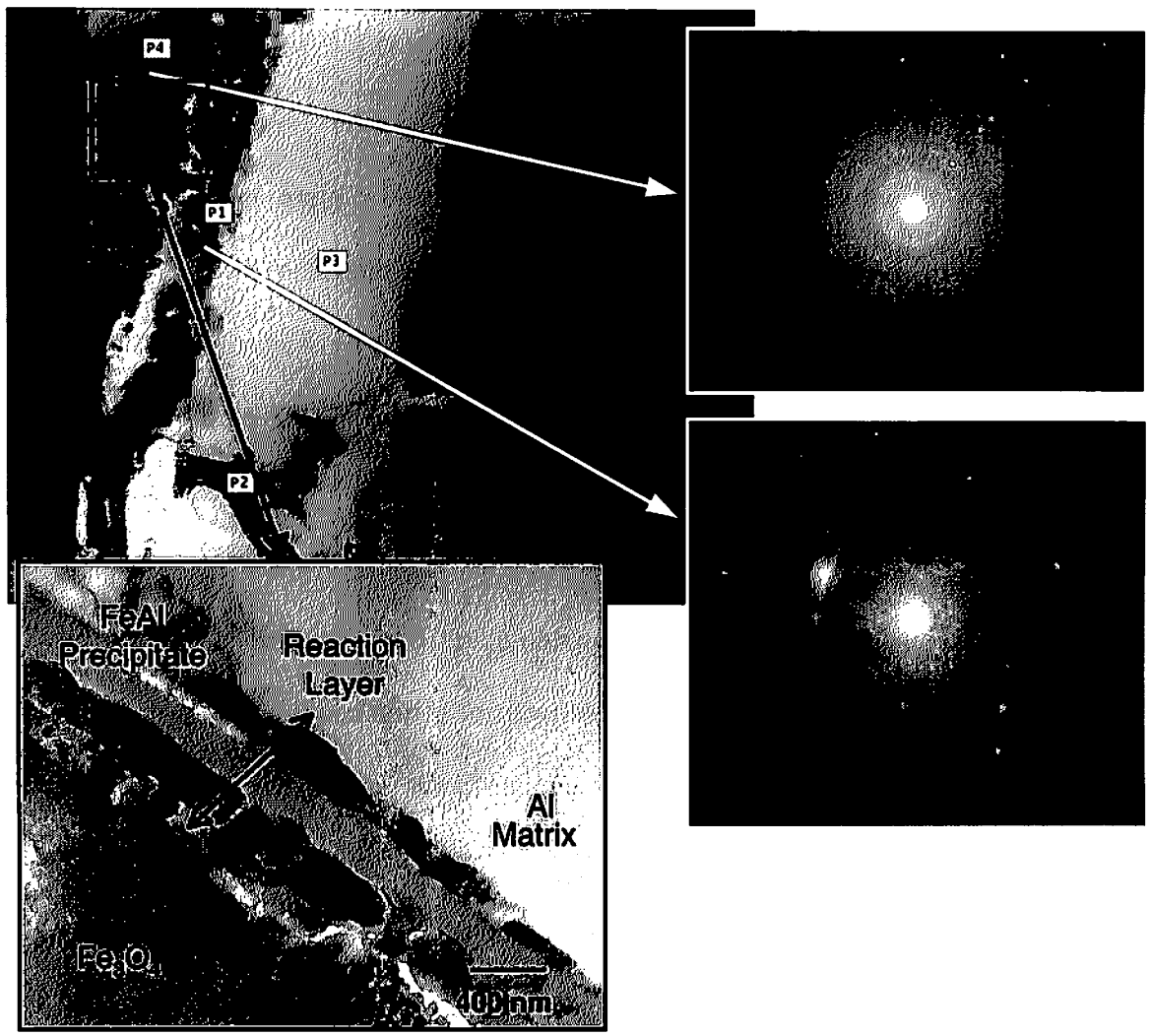


Figure 4.23: TEM indicating interfacial reaction between Fe_3O_4 particle and Al matrix. Selected area diffraction (SAD) pattern and energy dispersive spectroscopy was used for analyzing phases present.

and dendrite melting can take place. Additionally, violent reaction between Fe-oxide and liquid aluminum is expected to add to the turbulence promoting convection driven dendrites remelting. This would further grain multiplication.

Figure 4.24 is a high magnification scanning electron micrograph in which very fine grains (<200nm), perhaps underdeveloped cells or dislodged dendrite arms are seen. Extremely high solidification rate provides very little time for cells to develop into complete dendrites. Moreover, such high cooling rates trigger formation of various metastable phases and extremely fine grain structures. When the melt is substantially under-cooled growth of crystalline nuclei occurs under non-equilibrium conditions with the solid/liquid interface temperature much different from the equilibrium freezing temperature. Under these conditions new and complex microstructure develops as in the case of laser surface melting. As discussed above, by controlling nucleation and growth in quenched out combustion synthesis reaction initiated by laser surface engineering there exist a potential for synthesis of Fe-oxide nanocoating on A319 cast alloy.

Secondary electron micrograph (taken in Scanning Auger Microprobe) in Figure 4.25 shows the oxide particles fragmented during the laser treatment (confirmed by microanalysis). Attaining temperature above 3000°C is common in conventional thermite welding operations [38]. Intense power input and conduction-mode heat transfer to substrate that acts as an infinite heat sink in laser surface engineering often causes extremely rapid heating and cooling. Combined with highly exothermic thermite reaction, the solidification structures can alter extensively. The double exothermic reactions (reduction of iron oxides and reaction between Al and Fe to form aluminides) result in a violent process disintegrating the reactants and reaction products. Because of this thermal

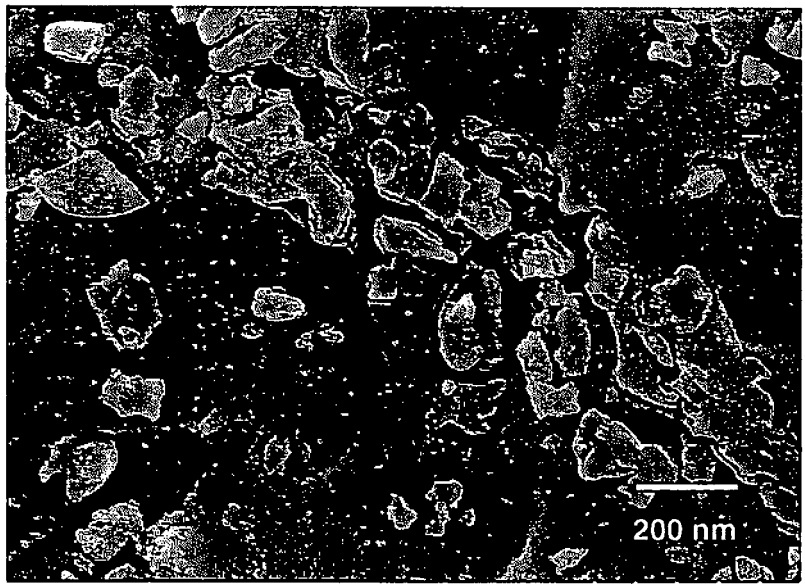


Figure 4.24: SEM of ultrafine particles formed in laser coating.

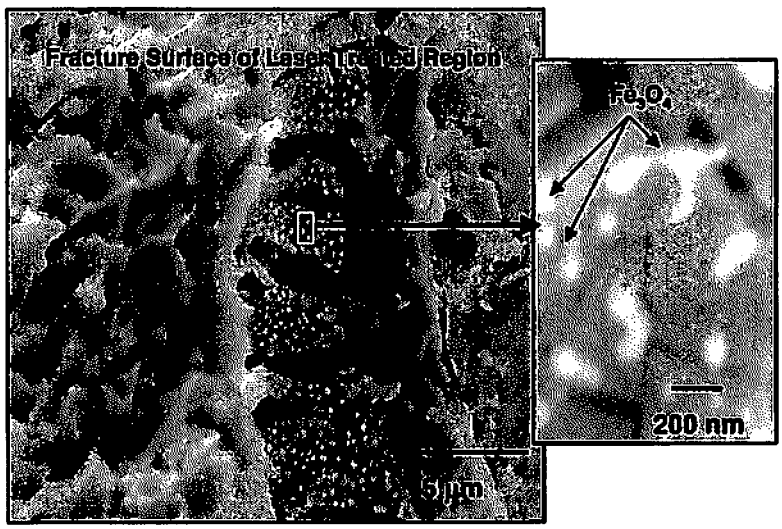


Figure 4.25: SEM of fragmented Fe_3O_4 particles.

effect the oxide particles are often fragmented to nanoscale. Formation of these ultrafine features during laser coating has significantly evaluated employing IIT technique (H, E, fracture resistance), in conjunction with scratch test (H_s and adhesion) and dry sliding wear test. The following section discusses evaluation of mechanical properties in light of the microscopy mentioned above.

4.2.3 Mechanical Properties

Figure 4.26 shows secondary electron image of a typical Berkovich indentation impression of indentation depth of 1000nm. It is clear from this micrograph that a single impression covers representative of the entire composite. There is no crack found in the SEM micrograph. Also, no deformation around the indentation was apparent in the secondary electron image. Several tracks of indentations (total number of indentations ~100) were made for different indentation depth. This allows determination of average properties of the composite material. Hardness (H) and elastic modulus (E) thus calculated are presented in Table 4.14.

The average E and H measured at maximum load of 150 mN (with average indentation depth of about 2200 nm) were ~ 76 GPa and 1.24 GPa, respectively (standard deviation less than 7%). Behavior of H and E with respect to the depth of indentation is presented in Figure 4.27. As seen in Figure 4.27 a, the hardness is higher for smaller depth of indentation, discussed previously as "indentation size effects". Furthermore, the elastic modulus as a function of depth of indentation depicts similar trend (Figure 4.27 b), however, of much smaller magnitude. The standard deviation in hardness, H

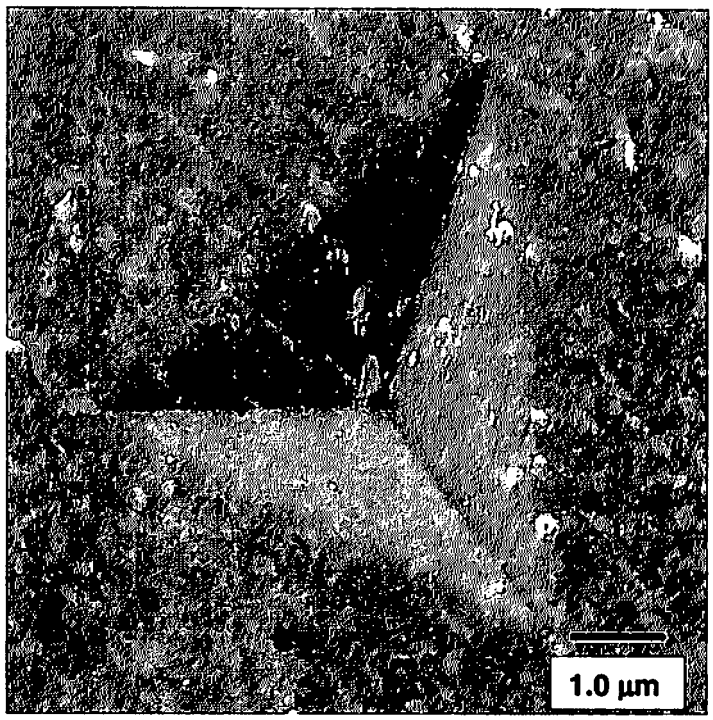
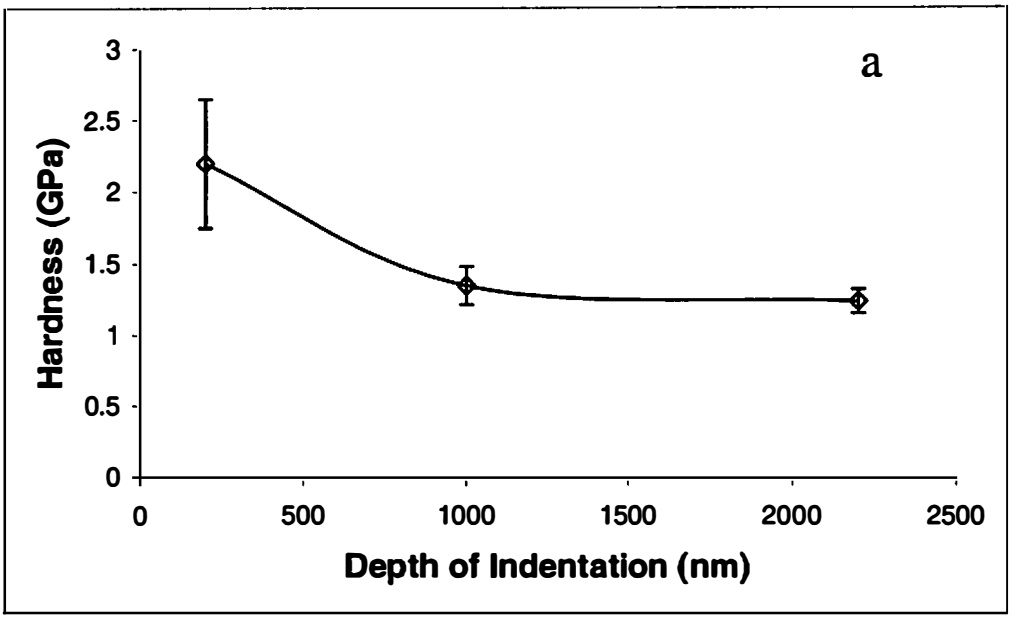


Figure 4.26: SEM of an indentation impression (Berkovich tip).

Table 4.14: Nanoindentation (Berkovich) data for Fe_3O_4 coating.

Indenter	Depth Or Load	Hardness (GPa)	Elastic Modulus (GPa)
Berkovich	200nm	2.2 ± 0.45	101 ± 8.3
	1000nm	1.35 ± 0.13	79.5 ± 2.7
	150mN (~2200 nm)	1.24 ± 0.09	76.0 ± 3.3



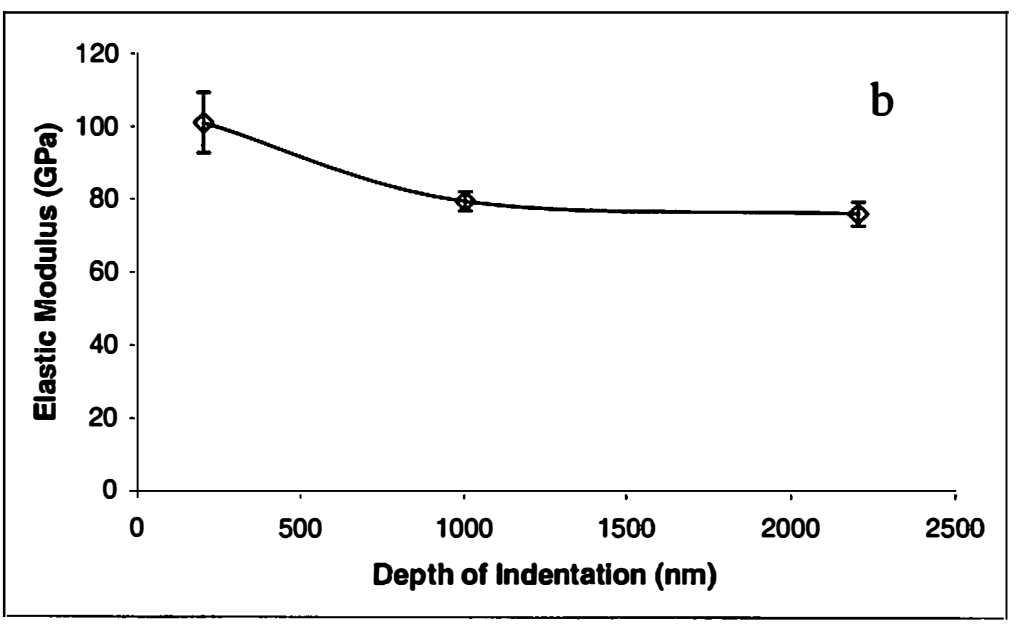


Figure 4.27: Properties of the Fe_3O_4 coating as a function of indentation depth.

corresponding to indentation depth h = 200 nm is substantially higher than that for h = 1000 nm and 2200 nm. This signifies the different response of material in terms of the mechanical behavior in lower depth of indentation compared to that in higher depth. Since, the coating is homogeneous to a scale in the order of a micron, the stochastic probability of encountering discrete harder and stiffer particles (like Si, Fe_3O_4, FeAl and other reaction products) is higher for h = 200 nm. This can increase the average values as well as standard deviation. In other words, the reaction composite coating is "effectively" homogeneous material to indentation for h > 200 nm. Indentation size effect of this type of coating has been investigated by plotting reduced elastic modulus as a function of indentation depth [$E_{reduced}$ vs. h] and observed whether the stochastic model reveals any segregation. As shown in that study [57], it was determined that the indentation size effect for this composite primarily sourced from extreme difference in properties of its constituents.

No particular trend in the hardness or elastic modulus was observed within the coating for a particular depth of indentation, when traced from the edge towards the interface in the cross-sectional samples, indicating the property is reasonably uniform throughout this coating owing to combination of refinement in microstructure and convective mixing in the liquid pool during laser treatment. Even for indentations load up to 150 mN (about 2200 nm deep) the load-displacement responses did not show any signs of cracking with the Berkovich indenter. For 200 nm depth indentation (Berkovich), since, the deformation mechanism is different (a hard thin film of work hardened material on a softer substrate) the $\frac{h_f}{h_{max}}$ and **m** is significantly different (Table 4.15). Large

number of data points (> 100) and very good correlation (R=1), however, indicate that this behavior is related to material characteristics and not experimental artifacts since the instrument was calibrated well. The fact that, even the elastic modulus (Table 4.14) is different for h = 200 nm from higher h is particularly intriguing since E is a structure insensitive property suggesting only work hardening can not explain the indenter size effect. Since, the coating was homogeneous to a scale in the order of few hundred nanometers the stochastic probability of encountering discrete harder and stiffer particles (like Si, Fe_3O_4, FeAl and other reaction products) is higher for h = 200 nm. For h = 1000 nm the coating behaves more like an effectively homogenized single-phase material to indentation due to uniformly distributed very fine (~ order of 100 nm) hard/stiff particles in the matrix and the properties like E is dominated by that of the matrix. Smaller relative degree of plastic to elastic deformation (indicated by smaller $\frac{h_f}{h_{max}}$ compared to Al 8009 and other Al alloys [8-9, 17, 19] indicated that the material possess at least moderate level of work hardenability. The indentation with a cube corner tip exhibited large pile-up due to a sharp geometry, penetration of which could not be resisted by work hardening. Also, the material was extremely tough due to homogeneous distribution of fine reinforcing particles. Hence, even the cube corner indenter was deemed unsuitable to measure resistance to fracture. IIT appears to be a useful tool not only to quantify the properties such as hardness, H, elastic modulus, E, but also to provide qualitative comparison of materials behavior such as deformation, toughness, work hardening capacity and plastic-elastic responses. Besides, the elastic modulus, hardness, and on-set of crack (fracture resistance) a wealth of information is present in an un-loading curve.

Various approaches have been adapted to derive other mechanical properties of a sample by analyzing the un-loading data [49, 50, 77, 78]. Two such analyses are presented here.

Power-law Behavior During Unloading:

The unloading data obtained during IIT was curve fitted as the power law.

$$P = \alpha (h - h_f)^m \qquad (4.6)$$

(where h_f is the final displacement after complete unloading and and m are material constant). Since, the h is combination of elastic and permanent (plastic) deformation and h_f is the final plastic deformation, $h - h_f$ gives the elastic portion of deformation, since unloading is essentially elastic in nature [78, 77]. The data is presented in Table 4.15 along with examples and explanation from various literatures [45, 78, 77, 79, 80]. In the present investigations, for most cases, the correlation factor, R, was found to be greater than 0.999. Such good correlation indicates that the load and displacement is indeed described by a power law [77, 78]. The value of the power-law exponent (m) in the unloading for the Berkovich indenter was about 1.6 for 200 nm indentation depth and ~ 1.2 for 1000 nm and 2200 nm indentation depths. The exponent m for unloading in the cases of cube corner indentation was in the range of 1.5 - 1.6. Even though the self-similar geometry of a pyramidal indenter most closely approximates a cone, these values of m are consistent with neither the conical geometry (m = 2), nor at punch geometry (m = 1) [79]. Observed m is of intermediate value (1.2 - 1.6), which is, in fact, closer to solid of revolution (m = 1.5) [81, 79]. It has been recently reported that the power fit (m = 1.2-1.6) that provides a good description of the unloading data in most

Table 4.15: Analysis of unloading data in IIT.

Material	Indenter		Ref.	Comment	m	n	$\frac{h_f}{h_{max}}$	R
Elastic	Shape of a smooth Function		[20]	$z = u(r^n)$	1 + 1/n	n	0	X
Elastic	Flat punch		[20]	z = constant	1	∞	0	X
Elastic	Solid of revolution		[21]	$z = u(r^2)$	1.5	2	0	X
Elastic	Cone		[20]	z = u(r) (z = B.r)	2	1	0	X
Elastic	Pyramid		[18]	FEM	~2	~1	0	X
Rigid-plastic	Shape of a smooth Function		[18]	Analytical	1 + 1/n	n	1	X
Most materials	Berkovich		[8,9,17]	Experimental and FEM	1.2 - 1.6	1.5 – 5	0.5-1	X
Al 8009 Elastic-almost-perfectly plastic	Berkovich		[17]	Expermental, Analytical and FEM	1.32-1.38	2.63	0.95	0.99994
Fe_3O_4/Al composite coating	Berkovich	h = 200 nm	Present Work	Experimental Data	1.6	1.67	0.84 ± 0.004	0.998
		h = 1000 nm			1.2	5	0.91 ± 0.006	1
		h = 2200 nm			1.2	5	0.92 ± 0.006	0.9994
	Cube Corner	P = 400 mN			1.53	1.9	0.97 ± 0.002	0.9994
		P = 200 mN			1.55	1.82	0.97 ± 0.002	0.9995
		P = 100 mN			1.54	1.85	0.96 ± 0.005	0.9996
		P = 50 mN			1.60	1.7	0.97 ± 0.002	0.9996
		P = 20 mN			1.59	1.7	0.96 ± 0.006	0.9996

materials [77] is fundamental in nature and is a consequence of complex elastic-plastic deformation processes occurring during unloading [77]. It has been found out that even for a sharp, geometrically self-similar indenter, like a cone or pyramids, the elastic and plastic strain around the tip is shaped more like a parabola of revolution than a cone. In other words, the effective shape of the indenter during unloading is more like a paraboloid of revolution but with a smooth function of power slightly different than 2, i.e., the shape of an indenter is given by z = u(r), where z is the vertical position, r is the radial distance from first contact point and u(r) is a smooth function involving $\mathbf{r^n}$. The exponent **m**, describing the shape of the unloading curve, is directly related to n describing the effective indenter shape by following equation.

$$m = 1 + \frac{1}{n} \qquad (4.7)$$

(where n is the power of relative radius of curvature of the effective shape of the indenter). It is equivalent to a situation in which a solid of revolution of the function **z = u(r)** were indenting an elastic half-space. The m corresponding to cube-corner indentations (1.5 - 1.6) are significantly higher than that corresponding to Berkovich indentation (1.2 - 1.6). A smaller m would mean a more uniform pressure distribution within the indenter-sample contact region. For cube corner indenter, the effective shape is described by solid with radius of curvature raised to power n > 1.7 (close to a paraboloid). This is reasonable since the cube corner is sharper than a Berkovich indenter is. Hence, the pressure decreases from its peak value as a function of radial distance more drastically compared to a Berkovich indenter. The power-law behavior of the unloading curve with very good correlation suggests the material is homogeneous and plastic to

indentation process. This is further confirmed with the comparison with literature data for most single-phase materials (Table 4.15). Power-law behavior even for a much sharper geometry (cube corner) indicates that the material is ductile. Higher **m** for cube corner tip, however, suggests that the work hardening is not too high, and the situation is closer to a cone indenting an elastic half- space as the deformation is predominantly elastic. This is reasonable for a particle reinforced composite material formed under non-equilibrium cooling containing high density of defects with lessened avenue for further work hardening.

Relative Elastic Recovery:

The relative degree of elastic and plastic deformation during indentation and un-loading is characterized by the ratio of elastic modulus to yield stress, $\frac{E}{\sigma_y}$. In this case, however, σ_y is not known. The ratio of final displacement to maximum displacement ($\frac{h_f}{h_{max}}$) is an experimentally measurable parameter that provides similar information as $\frac{E}{\sigma_y}$. Since h_f is entirely permanent deformation and h_{max} is combination of elastic and plastic deformation, the final displacement h_f, is smaller than maximum displacement h_{max}. A perfectly elastic material would completely recover. On the contrary, if the entire displacement is plastic, as in an elastic-perfectly-plastic material, (a material, which has very little work hardening capacity such as Al 8009 in Table 4.15) both the final and the maximum displacement would be the same and the unloading portion of the load-

displacement curve would be vertical ($\frac{h_f}{h_{max}} = 1$). Hence, the ratio ($\frac{h_f}{h_{max}}$) has 0 and 1 as the natural limits. Whether the material piles up or sinks-in depends on both $\frac{h_f}{h_{max}}$ and the work-hardening characteristics of the material. Since, the material cannot strain harden under load it would flow upward to resist penetration of the indenter, and, therefore, pileup is most significant in those that do not work harden and for which ($\frac{h_f}{h_{max}}$) is close to 1. On the other hand, sink-in occurs, irrespective of work-hardening characteristics, when ($\frac{h_f}{h_{max}}$) < 0.7 [17]. However, for $\frac{h_f}{h_{max}}$ > 0:7, the pile-up shall depend upon work hardening characteristics. For large values of $\frac{h_f}{h_{max}}$, true contact area A_{true} depends strongly on work-hardening characteristics of the material. With no work hardening, there is a large amount of pileup. In case of present composite coating (Fe_3O_4/Al) this ratio ↑ 0.92 (excluding indentation up to 200 nm as explained later) for Berkovich (Table 4.15). The microscopic examination of no or little pile-up and $\frac{h_f}{h_{max}}$ ratio (as compared to Al 8009 alloy 0.95) suggests that there is at least a moderate level of work hardening capacity. However, the high value of $\frac{h_f}{h_{max}}$ for cube corner tip (↑ 0.98), indicate that the material does not work harden too much. Therefore, extensive pile-up was seen in the case of cube corner tip. This is understandable because of the particle reinforcement of the matrix.

Toughness and Plasticity

Even for indentations load up to 150 mN (about 2200 nm deep) the load-displacement responses did not show any signs of cracking with the Berkovich indenter. This may be due to high toughness associated with the composite nature (Al matrix with uniform distribution of fine iron oxide and other reaction product particles) of the coating. Scanning electron microscopy of Berkovich indentation impression (Figure 4.26) confirmed that there is no crack. Furthermore, no cracking was observed in microstructure analysis, even at high magnification. This may be due to high toughness associated with the composite nature (Al matrix with uniform distribution of fine iron oxide and other reaction product particles, Figure 4.16(c)) of the rapidly solidified region.

Cube Corner Indenter: A cube corner indenter is considered to be suitable for fracture mechanics study since the threshold load for cracking is much less. In view of this, a cube corner indenter is considered to be suitable for fracture mechanics study since the threshold load for cracking is much less [51, 82]. Figures 4.28(a) and 4.29 shows a set of 5 indentations of different loads (400 mN, 200 mN, 100 mN, 50 mN and 20 mN). Secondary electron image of the impression corresponding to the even highest load indicates no sign of radial cracking [Figure 4.28(b)]. Instead, extensive plastic deformation is seen [Figure 4.28(a) and (b)] near the edges of the triangular impressions (no pile-up was visible for Berkovich indenter). Figure 4.29 shows typical load-displacement curves for different loads with no discontinuity in either loading or

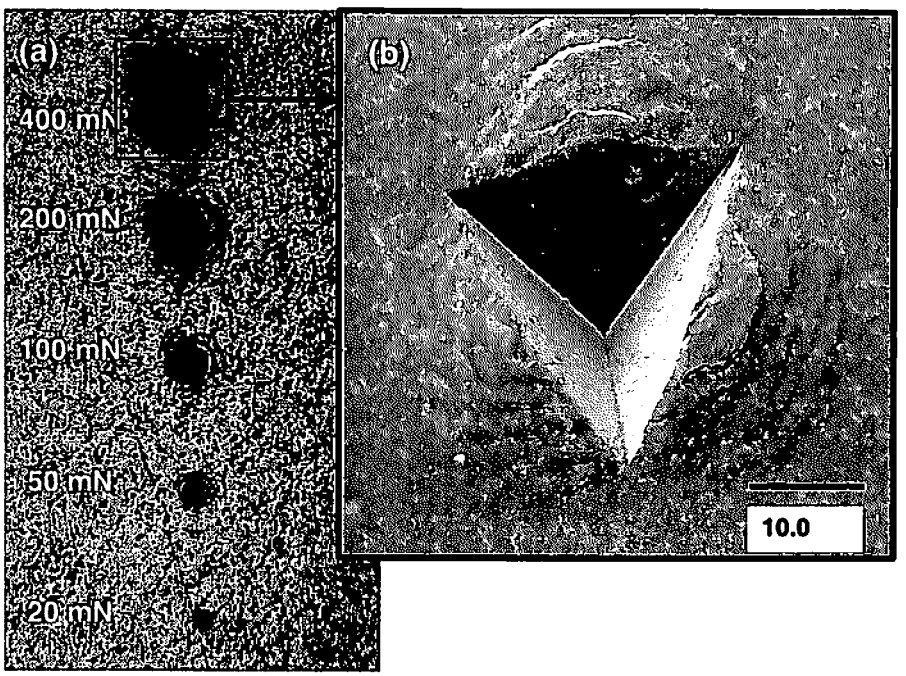


Figure 4.28: Cube-corner indenter impressions. (a) 5 indentations under different loads (b) SEM of a cube-corner indentation.

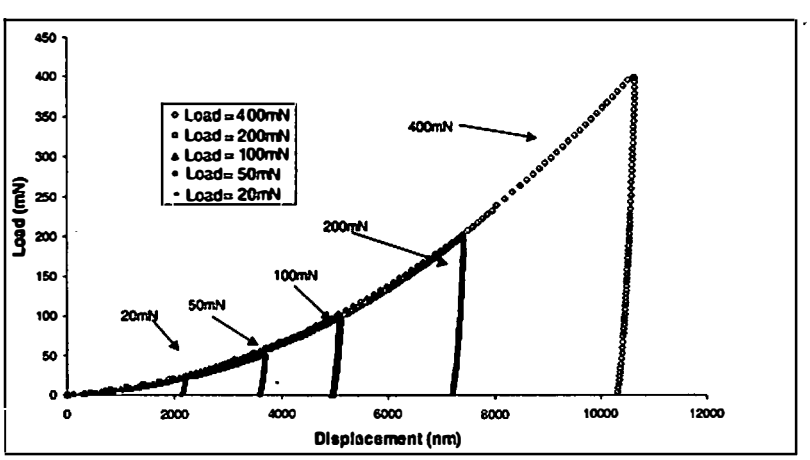


Figure 4.29: Load-displacement curves for cube corner indentation.

unloading curve, indicating absence of cracking. Also, all the unloading curves of Figure 4.29 are almost vertical, i.e., high $\frac{h_f}{h_{max}}$ (~ 0:96), Table 4.15) ratio and extensive pile-up.

Abrasion and wear are complex phenomena that are affected by several surface-layer mechanical properties including hardness, elastic modulus, ductility, and toughness and flow stress. As described above, the hardness and toughness have shown improvement. Such a tough and ductile coating is expected to improve abrasion and wear resistance of a component, hence, needs to be evaluated.

Abrasion and Wear Resistance:

Table 4.16 summarizes scratch hardness of pure Al, A319 alloy, remelted sample, FeO-coating and Fe_3O_4 coating. The A319 and all laser-treated samples have much higher hardness than pure Al samples due to presence of reinforcing phases such as Si-rich phases (and iron oxide and/or reaction products). However, for strong variation observed in A319 is because of the change in deformation mechanism. At much higher load, the scratch hardness drops drastically. This is possibly because of stress and deformation under the scratch surface, strong interaction with hard and discrete Si- and Cu-rich phases, and chip o of materials. It was further confirmed from frictional drag force and cross-sectional microscopic examinations. Fe_3O_4 and FeO-coatings have more or less constant scratch hardness, where as remelted samples, show higher scratch hardness for higher load (>3000g). Such variation in remelted A319 can be attributed to detachment of coating, interaction with discrete hard Si particles and/or deformation under the stressed region. Iron oxide coatings are adherent, effectively homogeneous and are load-

Table 4.16: Scratch hardness (GPa)

Load (g)	Pure Al	As received A319	Laser Remelted	FeO Coating	Fe_3O_4 Coating
1000	0.32	1.02	1.19	0.9	1.22
1500	0.34	1.14	1.23	0.87	1.21
2000	0.33	1.32	1.23	0.88	1.08
2500	0.37	1.25	1.24	Not done	Not done
3000	0.34	1.13	1.44	0.89	1.10
4000	0.29	0.79	1.43	0.82	1.19
5000	Not done	0.64	1.69	0.76	1.14

independent. Again, as mentioned in the section on IRT, Fe_3O_4 reacts more readily (compared to FeO) with Al. Fe_3O_4 coating has highest scratch hardness because of good reaction-induced bonding between iron-oxide particles and Al-matrix. Also, the products of such reaction contribute to toughening of the coating.

Figure 4.30 indicates the cumulative weight loss over 30 mins (equivalent to 8000m sliding distance) for the remelted sample as well as for the base. It is clear that under identical conditions, the weight loss of the laser-refined sample is substantially less than that of the as-received sample. More significantly, the surface of the laser-melted sample was much rougher compared to the as-received ground sample used in wear test. The laser melting of sample creates wavy pattern. The numerous asperities prevent greater contacts, resulting uneven stress during wear test and greater weight loss. The significant slope change at about 14 minutes of wear is due to settling of these asperities with wear surface profile. All the laser surface engineered samples show better wear resistance than the as-received A319. Also, the increase in weight loss is more gradual

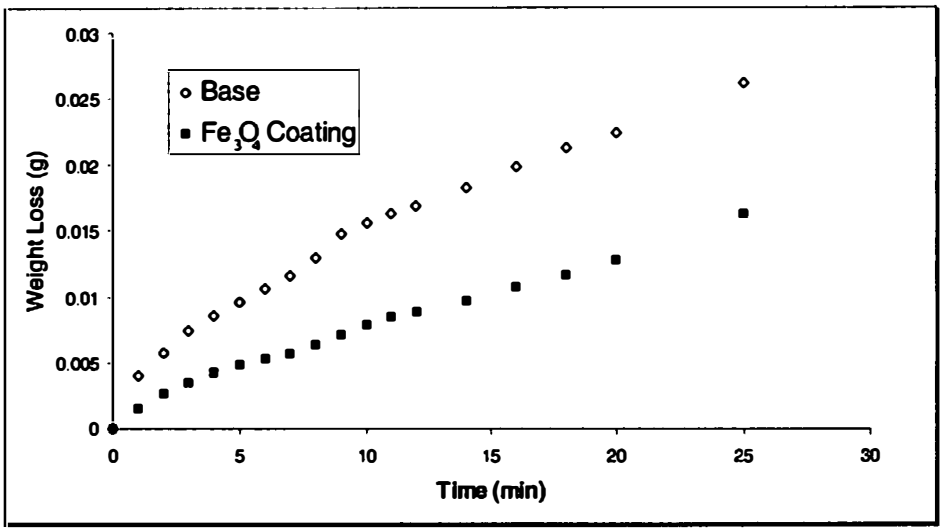


Figure 4.30: Weight loss under dry sliding test, 10N load

with increase in the load up to 13 N for FeO-coated and up to 18 N for remelted A319 and remains constant after that. Unlike the as-received A319, the laser surface engineered samples did not exhibit subsequent drop in scratch hardness and wear rates until much higher load. The drop in wear-rate in the as-received A319 is because the wear mechanism changes due to physical changes (disappearance or welding of voids, increase in number density of fractured Si particles, etc.). On the contrary, the refined microstructure in laser surface engineered samples can completely eliminate or at least substantially delay such change in wear mechanism. In view of this, it can be stated that when the structure is refined, the response to stress from point to point will be more consistent and uniform. Thus, if the response of individual phases is similar, the wear rate is less sensitive to normal load.

Chapter 5

Conclusion

- Though the laser induced rapid solidification caused extensive refinement in structure of A319, it did not change the overall microstructural morphology. The microstructure in the laser-melted surface, consists of fine dendrites of primary Al, Si in an eutectic mixture and $CuAl_2$ phase.
- Thermal conditions during LSE were evaluated by a high-speed IR thermographic imaging technique. Empirical calculations based on non-steady and steady state thermal conditions during laser processing also estimated a range of cell size within the modified surface region that is in close agreement with the experimentally measured average cell size.
- Evaluation of mechanical properties using IIT indicated that refined microstructure in the coating has, in general, reduced the scattering in hardness values with indentation depths $\perp$ 500nm leading to an assumption that the laser melted layer is homogenous.
- At even lower depth of indentation (<50 nm), the scatter in reduced elastic modulus is substantially higher but spread continuously from low to high value of 70-140 GPa.
- Although, the refinement in the microstructure of laser melted A319 has higher hardness compared to as-received A319, the elastic modulus was less affected due to its insensitivity to structural changes.

- In the iron oxide coated sample, the rapid solidification has caused refinement of the microstructure with formation of several reaction products.
- Both stoichiometric (e.g., Al3O3, FeAl, FeAl3 and Fe3Al) and non-stoichiometric phases (e.g., Fe-Al-O) were formed as a result of thermite reaction.
- These reaction products were found in discrete particle-like features as well as in interfacial regions.
- Using nanoindentation, it was possible to estimate hardness and elastic modulus of the coating. Refinement of the microstructure has enhanced the hardness of iron oxide coated sample and reduced the scattering in hardness values.
- Because of microstructure refinement and presence of interfacial reaction products as well as reinforcement of the Al matrix by particle-like features, the mechanical properties measured by IIT were improved.
- The Berkovich and cube corner indenter even with highest load did not induce crack near the corners of indentation impressions, suggesting that the reaction coating is tough.

Bibliography

[1] A.L. Kearney. Properties and Selection: Nonferrous Alloys and Special-Purpose Materials, volume 2, chapter Properties of Cast Aluminum Alloys, pages 152{177. ASM International, Materials Park, Ohio, 10th edition, 2000.

[2] Frederick S. Pettit. Surface Engineering of Aluminum and Alloys, volume 5, chapter Surface Engineering of Nonferrous Metals, pages 784{804. ASM International, Materials Park, Ohio, 10th edition, 1996. 2nd print.

[3] Annejan B. Kloosterman. Surface Modification of Titanium with Lasers. PhD thesis, Groningen University, May 1998.

[4] M.G. Hocking, V. Vasantasree, and P.S. Sidky, editors. Metallic and Ceramic Coatings- Production, High Temperature Properties and Applications. Longman Scientific and Technical, Harlow, Essex, England, 1st edition, 1989.

[5] http://www.aluminum.org/.

[6] Elwin L. Rooy. ASM Handbook, Properties and Selection: Non-ferrous Alloys and Special-Purpose Materials, volume 2. ASM International, 10th edition, 1995.

[7] Jr William D. Callister. Materials Science and Engineering: An Introduction. John Wiley Sons, Inc., fifth edition, 2000.

[8] Haizhi Ye. An overview of the Development of Al-Si Alloy Based Material for Engine Application. Journal of Materials Engineering and Performance, 12(3):288{297, June 2003.

[9] S.H. Avner. Introduction to Physical Metallurgy. McGraw Hill Book Co., Singapore, 4th edition, 1974.

[10] T.B. Massalski, H. Okamoto, P.R. Subramanian, and L. Kacprzak. Binary Alloy Phase Diagram. ASM International, Materials Park, OH, 1990.

[11] M. Pierantoni, M. Gremaud, P. Magnin, D. Stoll, and W. Kurz. The coupled zone of rapidly solidified Al-Si alloys in laser treatment. Acta Metallurgica and Materilia, 40(7):1637{1644, 1992.

[12] Hume-Rothery and G. Y. Raynor. The Structure of Metals and Alloys. Institute of Metals, 1962.

[13] M.D. Dighe and A.M. Gokhale. Relationship between microstructural extremum and fracture path in a cast al-si-mg alloy. Scripta Materilia, 37(9):1435{40, 1997.

[14] D. R. Askeland. The Science and Engineering of Materials. Chapman and Hall, New York, 3rd SI edition, 1996.

[15] R. E. Spear and G. R. Gardner. Dendrite cell size. Trans. Amer. Foundrymen's Society, 71:209{215, 1963.

[16] A.M. Papon and S. Paidassi. x. In P.L. Wee and R. S. Carbonara, editors, Proceedings of International Conference on Rapidly Solidified Materials, page 317, San Diego, 1986.

[17] M. L. V. Gayler. Journal of Institute of Metals, 38:157, 1927.

[18] S. Das, A.H. Yegneswaran, and P.K. Rohatgi. J. Mater. Sci, 22:3173, 1987.

[19] Tim Basner. Rheocasting of Semi-Solid A357 Aluminum. Technical Report 2000-01-0059, SAE Tech. Paper, 2000.

[20] J. Clarke and A.D. Sarkar: Wear characterization of as-cast binary Al-Si alloys. Wear, 54:7{16, 1979.

[21] S. Tomida, K. Nakata, S. Shibata, I. Zenkouji, and S. Saji: Improvement in wear resistance of hyper-eutectic Al-Si cast alloy by laser surface remelting. Surface and Coatings Technology, 169-170:468{471, 2003.

[22] A.K. Prasada Rao, Karabi Das, B.S. Murty, and M. Chakraborty: Effect of grain refinement on wear properties of Al and Al-7Si alloy. Wear In press, 2004.

[23] Frederick S. Pettit: Surface Engineering of Non-ferrous Metals, volume 5. ASM International, 10th edition, 1996.

[24] Marcel Schneider: Laser cladding with powder. PhD thesis, University of Twente, Enschede, March 1998.

[25] J. Th. M. De Hosson: Intermetallic and Ceramic Coatings, chapter Laser Synthesis and Properties of Ceramic Coatings, pages 307{439. Marcel Dekker, Inc., New York, 1st edition, 1999.

[26] M. Pilloz, J.M. Pelletier, A.B. Vannes, and A. Bignonnet:. Journal de Physique., Colloque C7(suppl. 1):117, 1991.

[27] H. Ushio K. Shibata: Tribology International, 27:pp39-42, 1994.

[28] Cole G.S. and Bin F.P: Al:Si. In Proceedings of the ASM 1993 Materials Congress, pages 17{21. ASM International, October 1993.

[29] T. Imura, T. Suenaga, T. Hayashi, and H. Ushio: Engine cylinder coating. Technical Report 890557, SAE Tech. Paper, 1989.

[30] V D N Rao, D. M. Kabat, H. A. Cikanek, C. A. Fucinari, and G. Wuest: Engine cylinder coating. Technical Report 970023, SAE Tech. Paper, 1997.

[31] G. Wuest, G. Barbezat, and S. Kellar: Engine cylinder. Technical Report 970016, SAE Tech. Paper, 1997.

[32] Y. Suzuki: Anodizing of aluminum. J. Mater. Eng., 10(1):61{67, 1998.

[33] M.G. Nicholas N. Eustathopoulos and B. Drevet: Wettability at High Temperature. Pergamon, New York, 1999. p93-97.

[34] F.D.Richardson and J.H.E.Jeffes: The standard free energy of formation of metal sulfides as a function of temperature. J. of Iron and Steel Ind., 171:167, 1952.,p151

[35] David R. Gaskell: Introduction to the Thermodynamics of Materials. Taylor and Francis, London, 1995.

[36] H.J.T. Ellingham: Thermodynamics of oxidation of elements. J. Soc. Chem. Ind., 63, 1944.

[37] J.J. Moore and H.J. Feng: Combustion Synthesis of Advanced Materials: Part I, Reaction Parameters. Progress in Materials Science, 39:243, 1995.

[38] B. Schwartz: Welding, Brazing, and Soldering, volume 6, chapter Thermite Welding, pages 291{293. ASM International, Materials Park, Ohio, 10th edition, 2000. 5th Print.

[39] M.C. Flemings: Behavior of metal alloys in the semisolid state. Metallurgical Transaction, 22A:957{981, 1991.

[40] Richard P. Feynman: The Feynman Lectures on Physics. Addison-Wesley Publication Company, Menlo Park, CA, 1986.

[41] Frederick Elicit Cunningham: The use of lasers for the production of surface alloys. Mechanical engineering, Massachusetts Institute of Technology, Cambridge, MA, June 1964. First result on LSA.

[42] J. DuttaMajumdar, R. Galun, B.L. Mordike, and I. Manna: Effect of laser surface melting on corrosion and wear resistance of a commercial magnesium alloy. Materials Science and Engineering, A361:119{129, 2003.

[43] I. M. Hutchings: Tribology, Friction and Wear of Engineering Materials; Arnold, London, 1992. 152

[44] J.F. Archard: Contact and rubbing of at surfaces. J. Appl. Phys., 24:981{988, 1953.

[45] D. Tabor: Hardness of Metals. Oxford University Press, New York, 1950. Classics Series in Physical Sciences.

[46] S.V. Prasad and P.K. Rohatgi: J. Metals, 39:22{26, 1987.

[47] S.Skolianos and T.Z. Kattamins:. Mater. Sci. Eng. A, 163:107, 1993.

[48] K.J. Bhansali and R. Mehrabian: Abrasive wear of aluminum-matrix composites. J. Metals, 34:30, 1982.

[49] W.C. Oliver and G.M. Pharr: An improved method of instrumented indentation. J. Mater. Res., 7(6):1564, 1992.

[50] J.L. Hay and G.M. Pharr:. Instrumented Indentation Testing, volume 8, page 232. ASM International, Materials Park, Ohio, 10th edition, 2000.1st print.

[51] D.S. Harding, W.C. Oliver, and G.M Pharr: Fracture resistance determination via nanoindentation. In Materials Research Society Symposium Proceedings, volume 356, page 663, San Diego, 1995.

[52] P. Hedenqvist S. Jacobsson, M. Olsson and O. Vingsbo: Friction, Lubrication, and Wear Technology, volume 18, chapter Scratch Testing, pages 430{437. ASM International, Materials Park, Ohio, 10th edition, 2000.

[53] D. Rosenthal: Mathematical theory of heat distribution during welding and cutting. Welding Journal, Suppl.20;:220-234, 1941.

[54] D. Rosenthal: The theory of moving sources of heat and its application to metal treatments. Trans Amer Soc Mech Engg, 68:849, 1946.

[55] H.S. Carslaw and J.C. Jaeger: Conduction of heat in solids. Oxford: Clarendon Press, Oxford, 1962.

[56] S. Kou and R. Mehrabian: editors. Modeling of Casting and Welding Processes III. The Metals, Minerals and Materials Society, TMS,Warrendale,PA, 1986.

[57] S. Nayak, L. Reister, and N. B. Dahotre: Instrumented Indentation Characterization of Laser-Remelted A319Al Alloy. Journal of Materials Research, 19(1):202-207, January 2004.

[58] C. Chan, J. Mazumdar, and M.M. Chen: An axis-symmetry model for convection in a laser melted pool. In K. Mukherjee and J. Mazumder; editors, Proceedings of a symposium of Metallurgical Soc. of AIME, page 3, Los Angeles, California, Feb-Mar 1984. AIME, AIME.

[59] M.F. Doerner and W.D. Nix. Nanoindentation: J. Mater. Res., 1(4):1086, April 1983.

[60] K.W. McElhaney, J.J. Vlassak, and W.D. Nix: Indentation size effect. Journal of Materials Research, 13, 1998.

[61] L.E. Samuels. Metallographic Polishing by Mechanical Methods. Pitman, London, 1967.

[62] J.B. Pethica, R. Hutchings, and W.C. Oliver. Nanoindentations. Philos.Mag. A, 48(4):593, 1983.

[63] J.G. Swadener, E.P. George, and G.M. Pharr. Nanoindentation. J. Mech. and Phys. of Sol., 50(4):681, 2002.

[64] Y-L Shen and Y.L. Guo. Nanoindentation. Model. Simul. Mater. Sc. Eng., 9:391, 2001.

[65] George M. Pharr. Communication with professor. The University of Tennessee, Knoxville, TN.

[66] J. J. Noordhuis and Th.M. De Hosson. Surface modification by means of laser melting combined with shot peening: A novel approach. Acta Metallurgica et Materialia, 40(12):3317, 1992.

[67] J. J. Noordhuis and Th.M. De Hosson. Microstructure and mechanical properties of a laser treated al alloy. Acta Metallurgica et Materialia, 41(7):1989-1998, July 1993.

[68] X.B. Zhou and J. Th. M. De Hosson. Reactive wetting of liquid metals on ceramic substrates. Acta Metallurgica et Materialia, 44(2):421, 1996.

[69] F.D.Richardson and J.H.E.Jeffes. J. of Iron and Steel Ind., 160:261, 1948.

[70] Narendra B. Dahotre, C. Xiao, W. Boss, M.H. McCay, and T.D. McCay:.Journal of Materials, 44(10):47{50, October 2001.

[71] Ralph Hultgren, Pramod D. Desai, Donald T. Hawkins, Molly Gleiser, and Kenneth K. Kelly. Selected Values of the Thermodynamic Properties of Binary Alloys. ASM, Metals Park, Ohio, 1973. page 156.

[72] F.A. Elrefaie and W.W. Smeltzer. Metall. Trans., 14(B):85{93, 1983.

[73] S. Nayak, L. Reister, H. M. Meyer III, and N. B. Dahotre. Micro-mechanical Properties of Laser Induced Iron Oxide-Aluminum Matrix Composite Coating. Journal of Materials Research, 18(4):833{839, April 2003.

[74] T.B. Massalski. Binary Alloy Phase Diagram. ASM International, Materials Park, Ohio, 1990.

[75] M.E. Drits, E.S. Kadaner, and V. I. Kuzmina. Russ Metall, 1:170-175, 1968.

[76] W. Kurz and D. J. Fisher. Fundamentals of Solidification. Trans Tech Publications Ltd., Switzerland, 1992.

[77] G. M. Pharr and A. Bolshakov. Understanding nanoindentation unloading curves. J. Mater. Res., 17:2660, 2002.

[78] G. M. Pharr, W.C. Oliver, and F.R. Brotzen. On the generality of the relationship between contact stiffness, contact area, and elastic modulus during indentation. J. Mater. Res., 7:613, 1992.

[79] I.N. Sneddon. The relation between load and penetration in the axisymmetric boussinesq problem for a punch of arbitrary profile. Int. J. Engng. Sci., 3:47-57, 1965.

[80] A. Bolshakov and G. M. Pharr. Influences of pile-up on the measurement of mechanical properties by load and depth sensing indentation techniques. J. Mater. Res., 13:1049{1058, 1998.

[81] H. Hertz. Uber die beruhrung fester elastische korper. Journal fuer die Reine und angewandte Mathematik, 92:156, 1882.

[82] B. R. Lawn, A. G. Evans, and D. B. Marshall. Cracking during instrumented indentation. J. Am. Ceram. Soc., 64:574, 1980.

Appendix

LIST OF PUBLICATIONS:

Journal:

(1) "Nanocoating for Engine Application," S. Nayak and N.B. Dahotre, **Surface and Coatings Technology** (Accepted).

(2) "Auger Microscopy of laser Induced Fe-oxide/Al Reaction Composite Coating," S. Nayak, H.M. Meyer, III, and N. B. Dahotre, **Surface Engineering**, Vol. 20, No. 1.

(3) "Surface Engineering of Aluminum Alloys for Automotive Engine Applications," S. Nayak and N.B. Dahotre, **Journal of Minerals, Metals and Materials Society (JOM)**, Vol. 56, No. 1, Jan. 2004.

(4) "Instrumented indentation probing of laser surface-refined cast Al alloy," S. Nayak, L. Reister and N. B. Dahotre, **Journal of Materials Research,** Vol 19, No 1, pp202-209, Jan. 2004.

(5) "Micro-mechanical Properties of Laser Induced Iron Oxide-Aluminum Matrix Composite Coating," S. Nayak, L. Reister, H. M. Meyer, III, and N. B. Dahotre, **Journal of Materials Research**, Vol 18, No 4, pp 833-839, Apr 2003.

(6) "Instrumented Indentation Characterization of Laser Induced Fe_3O_4 /Al Composite Coating," S. Nayak and N. B. Dahotre, **Advanced Engineering Materials**, Vol. 5, No. 4, Apr 2003.

(7) "The Laser Induced Combustion Synthesis of Iron Oxide Nanocomposite Coating on Aluminum," S. Nayak and N. B. Dahotre, **Journal of Minerals, Metals and Materials Society (JOM)**, Vol. 54, No. 9, pp. 39-41, Sept. 2002.

(8) "Evaluation of Laser Surface Engineered Iron Oxide Coatings on Cast Aluminum Alloy for Wear Application", A. Dasari, S. Nayak, R.D.K. Misra, O.O. Popoola and N. B. Dahotre, **Materials Science and Technology**, Vol. 18, pp. 11-18, Jun. 2002.

(9) "Laser Assisted Iron Oxide Coating on Cast Al Alloy for Automotive Engine Application", N. B. Dahotre, S. Nayak, and O. O. Popoola, **Journal of Minerals, Metals and Materials Society (JOM)**, Vol. 53, No. 9, pp. 44-46, Sept. 2001.

(10) "Thermal Diagnosis During Laser Surface Melting of Cast Aluminum Alloys", S. Nayak, Hsin Wang and N.B. Dahotre, **Journal of Applied Physics A** (In review)

(11) "Observation of Exothermic Reaction During Laser Induced Iron Oxide Coating on Aluminum Alloy", S. Nayak, Hsin Wang, Ian Anderson, E.A. Kenik and Narendra B. Dahotre, (In preparation).

Conference Proceedings/Presentations:

(1) "Microstructural Characterization of Laser Induced Iron Oxide - Aluminum Reaction Coating", S. Nayak, N. B. Dahotre, H. M. Meyer III and O.O. Popoola, ASM's Surface Engineering Congress, October 2002, Columbus, OH.

(2) "Nanoindentation Characterization of Laser Engineered Iron Oxide Coating on A319Al", N. B. Dahotre, S. Nayak, L. Reister and O. O. Popoola, ASM's Surface Engineering Congress, October 2002, OH.

(3) "Laser Surface Engineering of A319Al alloy", S. Nayak and N. B. Dahotre, Surface Engineering Symposium, THERMEC03, Madrid, Spain, 8th July 2003.

(4) "Nanocoating for Engine Application" N.B. Dahotre and S. Nayak, Invited talk on Nanocoating at International Conference on Metallurgical Coating and Thin Film, San Diego, 29th April 2003.

(5) "Auger Microscopic Study of Laser Induced Iron Oxide - Aluminum Composite Coating", S. Nayak, H.M. Meyer, III, and N. B. Dahotre, Microscopy and Microanalysis, August 2003, San Antonio. TX.

(6) "Auger Spectra Line Shape Study in Iron-Aluminum-Oxygen Reaction System", S. Nayak, H.M. Meyer, III, and N. B. Dahotre, American Vacuum Society 50th International Symposium, Nov. 2003, Baltimore, MD.

Contests

(1) "Rapidly Solidified Iron Oxide Particle - Aluminum Alloy Matrix Composite Coating," S. Nayak & Narendra B. Dahotre, **Minerals, Metals & Materials Society (TMS) Outstanding Student Paper Contest** - Graduate Division, 2002, Won Second Prize.

Book Chapter:

(1) Chapter on "Laser Surface Treatment", by S. Nayak and Narendra B. Dahotre for book entitled "Manufacturing Science". To be published by Academic Press. (In preparation).

Vita

Subhadarshi Nayak was born in Cuttack, India on 2nd April 1972, He did his schooling in Cuttack. In July 1991, he joined Indian Institute of Technology, Kharagpur to pursue Bachelor of Technology in Metallurgical Engineering. After receiving Bachelor degree he worked with Tractor Engineers Limited (an associate of Caterpillar Tractor Inc. and Larsen and Toubro Limited), Bombay, India as a Graduate Engineer Trainee and then as a Quality Engineer-Metallurgist. He worked on heat treatment, surface treatment, failure analysis, product and process development, on-field performance evaluation, and materials and product testing. After a brief tenure as a Software System Analyst with Infosys Technologies Limited, Bangalore, India, he joined the University of Tennessee in Aug 2000 to pursue his PhD in Materials Science and Engineering. He has extensive scientific publications in refereed international journals and conference proceedings. He has won several awards and recognition such as 2nd position in Materials Quiz organized by IIT, Kanpur, India, Second position in The Metals, Materials, and Mineral Society Outstanding Student Paper - Graduate Division 2002, University of Tennessee Citation for Extra-ordinary Professional Promise and Tennessee Advanced Materials Laboratory Graduate Fellowship.

5956 2951 15
06/23/04